**Dissertation**
**submitted to the**
**Combined Faculties for the Natural Sciences and for Mathematics**
**of the Rupertus-Carola University of Heidelberg, Germany**
**for the degree of**
**Doctor of Natural Sciences**

presented by

Dipl.-Ing. Giancarlo Maero
born in Savigliano, Italy

Oral examination: 12.11.2008

# Cooling of highly charged ions in a Penning trap for HITRAP

Referees: Prof. Dr. H.-Jürgen Kluge
Prof. Dr. Andreas Wolf

**Kühlung hochgeladener Ionen in einer Penningfalle für HITRAP**

Die HITRAP (Highly charged Ions Trap - Falle für hochgeladene Ionen)-Anlage wird an der GSI, Darmstadt, aufgebaut. HITRAP ermöglicht sehr präzise atomphysikalische Untersuchungen an hochgeladenen Ionen bei extrem niedrigen Energien. Sowohl die stabilen Ionen bis hin zu $U^{92+}$ als auch radioaktive Nuklide werden im GSI Beschleunigerkomplex produziert. Die Erzeugung hochgeladenes Ionen erfolgt bei relativistischen Geschwindigkeiten mit Hilfe der Strippertechnik. Danach werden die Ionen im Experimentspeicherring (ESR) eingefangen und unter Elektronenkühlung auf 4 MeV/u abgebremst. Bündel von $10^5$ Ionen werden in den HITRAP Entschleuniger ausgeschossen, dort auf 6 keV/u abgebremst und dann in einer Penningfalle, der so genannten Kühlerfalle, gefangen. Hier werden sie mittels Elektronen- und Widerstandskühlen bis auf 4 K abgekühlt bevor sie zu den Experimenten geschickt werden. Die Kühlerfalle wurde zu diesem Zweck entwickelt und ihr physikalisches und technisches Eigenschaften darauf hin optimiert. Erstmalig wurden die Kühlprozesse - insbesondere das Widerstandskühlen - für eine große Zahl hochgeladener Ionen mit Hilfe umfangreicher Simulationen untersucht. Die Simulationen lieferten sowohl ein generelles Verständnis der Prozesse in der Falle als auch wichtige Informationen für das Fallendesign.

**Cooling of highly charged ions in a Penning trap for HITRAP**

The HITRAP (Highly charged Ions Trap) facility is being set up at GSI, Darmstadt. It will enable high-precision atomic physics investigations on heavy, highly charged ions at extremely low energies. Species up to $U^{92+}$ as well as radioactive nuclides will be produced at the GSI accelerator complex by stripping of all or nearly all electrons from relativistic ions. Injected into the Experimental Storage Ring (ESR), they will be electron-cooled and decelerated to 4 MeV/u. Bunches of $10^5$ ions will be further decelerated in the HITRAP linear decelerator down to 6 keV/u and injected in a Penning trap. In this so-called Cooler Trap they will be cooled to 4 K via electron and resistive cooling before being sent to the experimental set-ups. The physical and technical design of the Cooler Trap has been conceived and optimized for this purpose. Moreover, the cooling processes for a high number of highly charged ions, and in particular the resistive cooling technique, have been systematically investigated in extensive simulations for the first time in order to gain sufficient information both for a general understanding and the design of the Cooler Trap.

a Simona

*There is always an easy solution to every human problem – neat, plausible, and wrong.*

H. L. Mencken

# Contents

# List of Tables

# List of Figures

# Chapter 1

# Introduction

The theory of quantum electrodynamics (QED) has shown so far an impressively precise predictive power. Observables have been calculated with extremely low relative uncertainties: striking examples include the *g-factor* of the free electron, whose accuracy has reached a relative value in the order $10^{-12}$ [Hug99] and recently $10^{-13}$ [Kin06], and the atomic levels of simple systems (i.e. where many-body effects can be neglected), like the hydrogen atom or few-electron atoms [Pac96, Pac98]. These achievements are made possible by the applicability of perturbative QED, where interactions between particles are expanded as a function of the perturbation term $\alpha \approx 1/137$, the fine-structure constant. The only limiting factor in terms of precision is the finite size of the nucleus.

On the experimental side, the same degree of uncertainty has been obtained: the *g-2* measurement with a relative accuracy of $4.3 \cdot 10^{-12}$ by Van Dyck and Dehmelt [Dyc87] earned the latter the Nobel prize in 1989. This impressive result could not be improved until 2006, when Gabrielse and collaborators reached 0.76 ppt in a $g/2$ measurement [Odo06], resulting also in the determination of $\alpha$ down to 0.7 ppb [Gab06]. The same group managed very recently to improve their own result, measuring $g/2$ to 0.28 ppt, i.e. with an uncertainty 2.7 and 15 times smaller than in 2006 and 1987 respectively. The resulting value of $\alpha$ achieves an accuracy of 0.37 ppb [Han08]. Combining QED with the experimental value of $g$ of the bound electron in $^{12}C^{5+}$ and $^{16}C^{7+}$, the mass of the electron has been pinned down to 0.4 ppb, i.e. to a relative accuracy of $7.3 \cdot 10^{-10}$ [Bei02, Bei03].

When moving to heavy and highly charged ions, perturbative QED breaks down [Moh98, Moh08] since the term $Z\alpha$ (where $Z$ is the nuclear charge of the ion) becomes comparable to 1 and cannot be used as perturbation term. This is the so-called *strong field* regime. Indeed, stripping heavy ions of their electrons results in extremely high electromagnetic fields. As shown in Fig. 1.1, the electron in the $1s_{1/2}$ state of uranium sees an electrical field in the order of $10^{16}$ V/cm, i.e. close to the threshold for spontaneous production of an electron-positron pair (Schwinger limit). Upon these considerations, non-perturbative

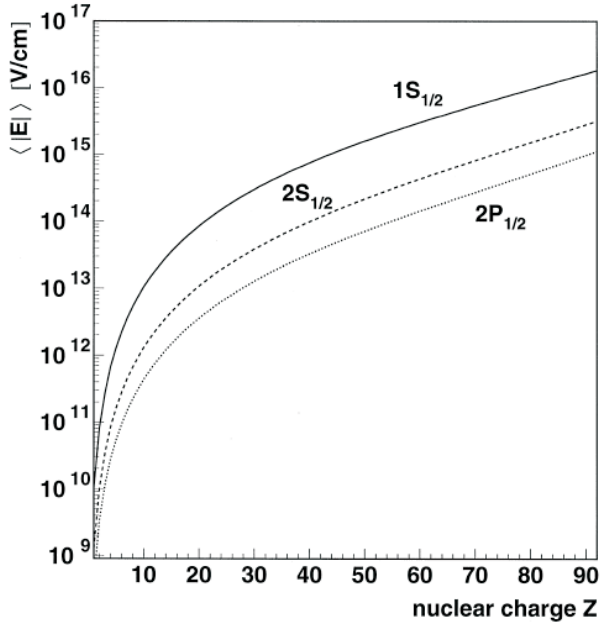


Figure 1.1: Electrical field strength in low-lying states of hydrogen-like ions. Picture reproduced courtesy of T. Beier [Bei00].

theoretical techniques have been developed [Moh98, Bei00]; on the other hand, experiments with heavy and highly charged ions are the perfect workbench to validate the theory.

The GSI accelerator complex represents a world-unique facility for the production of intense relativistic beams of heavy and highly-charged ions, thanks to the combination of synchrotron acceleration and in-flight electron stripping on a solid target at high ion beam energy [Fra87]. In order to reach ultimate accuracy the highly charged ions must be decelerated so that the uncertainty coming from the relativistic Doppler shift is eliminated. In 1990 the late Helmut Poth organized a workshop at GSI dedicated to deceleration and low-energy storage of highly charged ions. After his sudden and premature decease the activity continued with the development of a trap setup in Mainz where the *g-factor* of the bound electron in $^{12}C^{5+}$ was measured with an relative accuracy in the order of $10^{-10}$ [Häf00]. The first proposal for the HITRAP (Highly charged Ion TRAP) facility was submitted in 1998 and approved in principle in 1999 by the GSI directorate. However, due to financial restrictions, it became a mid-term project only in 2006 and was coordinated by the Atomic Physics Group, in the person of the group leader H.-Jürgen Kluge. The HITRAP project foresees a decelerator receiving the ion beam after acceleration in the heavy-ion synchrotron (SIS, SchwerIonenSynchrotron), stripping at high energy in a target, and a first deceleration, combined with stochastic and electron cooling in the Experimental Storage Ring (ESR). GSI

is responsible for the construction of the decelerator, which will provide large samples of low-energy ion species to the various experiments built by several institutes grouped under the HITRAP Network [TDR03]. These experiments include *g-factor*, mass and energy level measurements as well as observation of processes (low-energy atomic collisions, ion-surface interactions) where highly charged ions can reveal new information [Her06, Klu07]. At a later stage, HITRAP will be part of FLAIR (Facility for Low-energy Antiproton and Ion Research), the low-energy branch of FAIR (Facility for Antiproton and Ion Research, the future GSI upgrade).

A crucial part of the HITRAP facility is the Cooler Trap, the end-point of the decelerator, where the ion bunch will be trapped and cooled down to 10 eV or even further to the sub-meV range (i.e. some Kelvin, the temperature of the cryogenic setup), depending on the needs of the experiments. In this large Penning trap, electron and resistive cooling will be exploited to the purpose. But a careful study of the phenomena is necessary, both for the design phase and the understanding itself of these intricate and highly non-linear processes. Indeed, the resistive cooling of as many as $10^5$ highly charged ions simultaneously stored in a 6-T Penning trap has never been investigated yet, neither experimentally nor theoretically. The objective and focus of this work is therefore twofold. The first issue is the conception and development of the Cooler Trap, a large storage device with complex physical and technical features (size, cryogenic temperature, ultrahigh vacuum). The second issue is the analysis, via theoretical and simulation means, of the resistive cooling mechanism. A benchmark case for studying resistive cooling of many particles is the Mainz $C^{5+}$ experiment [Häf00], where cooling of 30 ions was achieved. The investigation presented in this thesis starts from the reproduction and interpretation of this experimental case and proceeds to characterize the behaviour of the cooling process and possible limitations for the case of higher numbers of particles and the Cooler Trap parameters.

Chapter 2 will give an overview of the HITRAP facility as a whole and a physical/technical description of each section. Experiments will be briefly presented, too. After a general introduction to Penning traps, Chapter 3 will deal with the physics considerations leading to the present design of the trap and will introduce the simulation tools used for the theoretical investigations. Chapter 4 will describe the theory of the cooling processes and discuss the simulations' results. The Cooler Trap technical details will be extensively covered in Chapter 5. Finally, Chapter 6 will summarize the main conclusions and outline the upcoming investigations and operations.

# Chapter 2

# The HITRAP facility

This Chapter intends to give a comprehensive description of the complete HITRAP facility in the framework of the GSI accelerator complex that feeds it. After a general overview, a more extensive explanation of each component is given, preceded by a brief description of HCI production and delivery to the facility. All sections are presented and discussed specifying their present

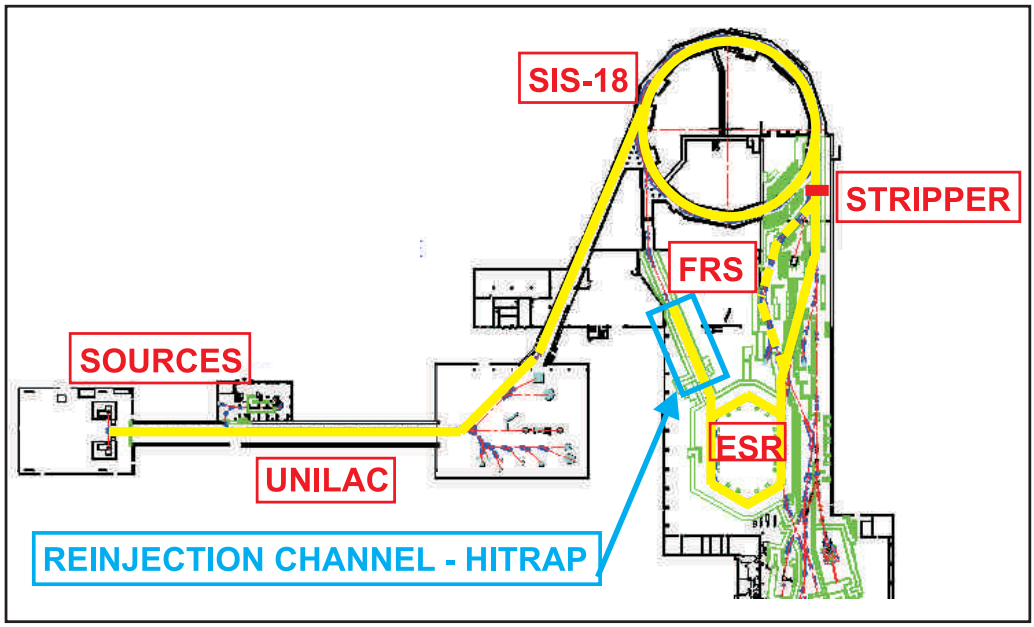


Figure 2.1: Overview of the GSI accelerator complex. The beam (yellow line) is accelerated and partially stripped in the UNILAC linear accelerator. It is further accelerated in the SIS-18 synchrotron, after which it is stripped in the stripper target to bare, hydrogen-like, helium-like or lithium-like ions. Radioactive species can be produced by nuclear reactions and selected in the FRagment Separator (FRS). Deceleration and cooling take place in the storage ring ESR. The beam is then sent to HITRAP, located in the ReInjection Channel.

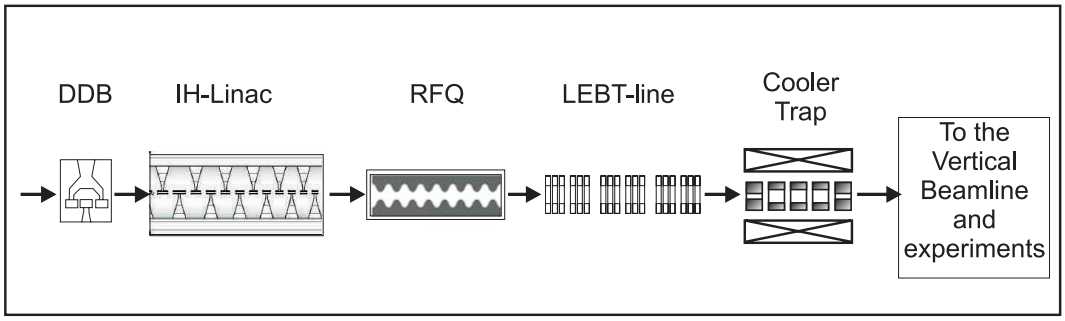


Figure 2.2: Schematics of the main HITRAP components. The Double-Drift Buncher (DDB) matches the beam extracted from the ESR into the Interdigital H-type (IH) linac. Here and in the following Radio Frequency Quadrupole structure (RFQ) the ions are decelerated and finally focused by the Low-Energy Beam Transport (LEBT) line into the Cooler Trap. In the trap ions are cooled before being sent to the experiments on the upper floor through the Vertical Beamline.

status. Finally, the planned experiments are introduced.

## 2.1 HITRAP Overview

The GSI accelerator chain, sketched in Fig. 2.1, consists of a series of subsequent facilities. A variety of ion sources is used to produce stable species ranging from hydrogen to uranium. The UNiversal LINear ACcelerator (UNILAC) accomplishes the first acceleration. Ions can then be already used in experiments in the UNILAC experimental hall or be injected into the Heavy Ion Synchrotron (SIS-18), a circular accelerator where they reach energies op to 1 GeV/u. Radioactive nuclides can be produced by fragmentation or Coulomb dissociation of the extracted primary beam, and the desired species is selected in the FRagment Separator (FRS). Stripping of electrons in a target yields highly charged ions (HCI). The ion bunch is then injected into the Experimental Storage Ring (ESR), where stochastic and electron cooling extend the beam lifetime and allow high-precision experiments at the desired energy.

The beam extracted from the ESR is guided towards the ReInjection Channel, a shielded tunnel formerly housing a beamline for reinjection of ESR beams into the SIS. The HITRAP facility (Fig. 2.2 and 2.3) is placed in this area and comprises itself several decelerating and cooling devices in series. The first part (medium-energy section) consists of a Double-Drift Buncher (DDB), an Interdigital H-type (IH) linear decelerator [Dah04] and a Radio Frequency Quadrupole (RFQ) [Hof06]. The DDB shapes the bunch to match the acceptance of the IH-linac. The linac and RFQ are designed to efficiently decelerate beams with a mass-to-charge ratio $m/q \leq 3$, but they perform no cooling. The latter is done in the low-energy section, after deceleration has made trapping possible. The beam is transported to the Cooler Trap through an electro-

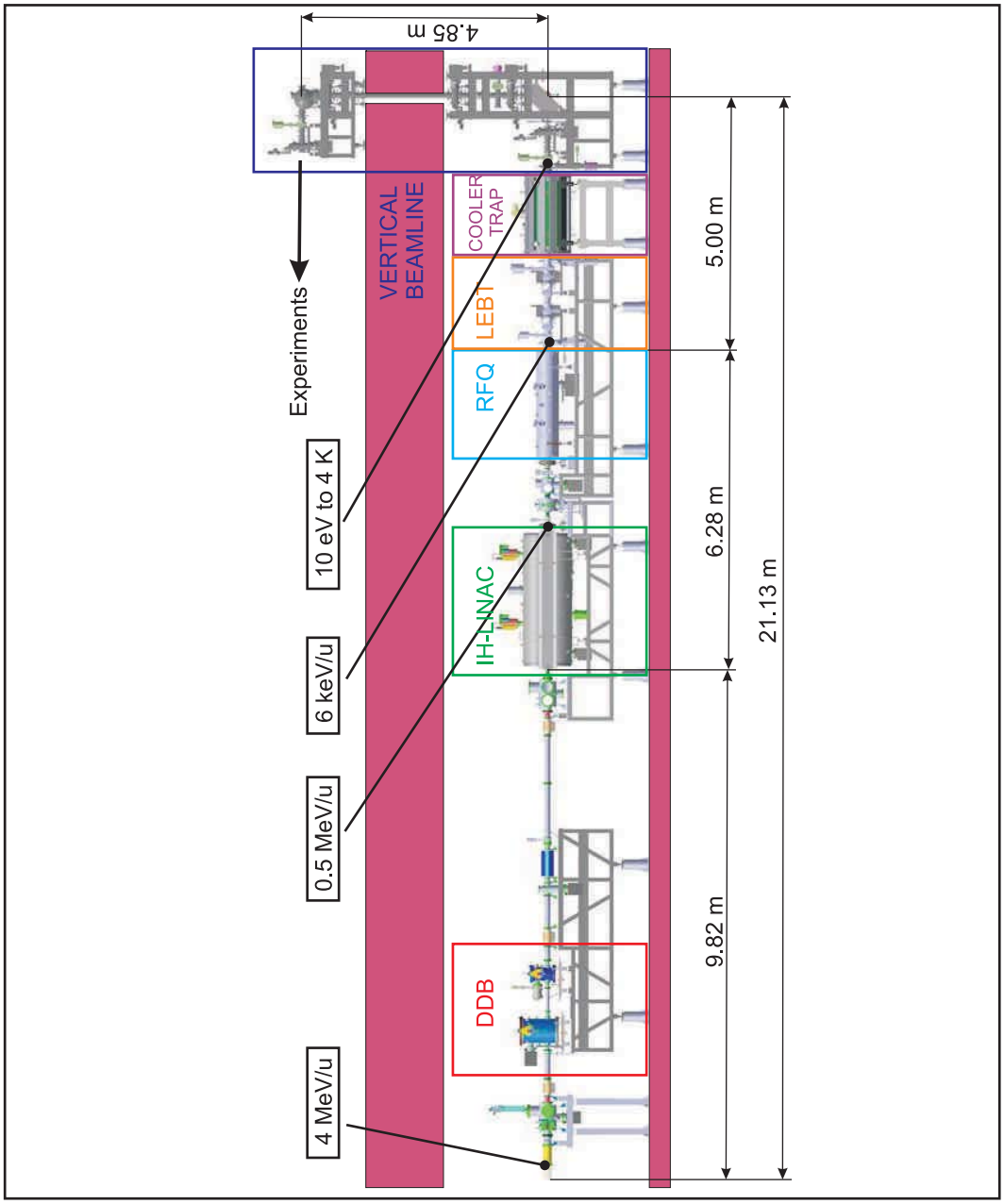


Figure 2.3: Overview of HITRAP facility. The beam comes from the storage ring ESR at 4 MeV/u. The Double-Drift Buncher (DDB) bunches the macrobunch extracted from the ESR into the Interdigital H-type (IH) linac, which decelerates the beam to 0.5 MeV/u. The Radio Frequency Quadrupole further decelerates the bunch down to 6 keV/u. The Low-Energy Beam Transport (LEBT) line focuses the beam into the Cooler Trap, where electron cooling down to 10 eV and resistive cooling down to 4 K take place. The cooled beam is sent to the experimental set-ups (not shown) located on the roof of the ReInjection Channel via the Vertical Beamline.

static beamline (LEBT, Low-Energy Beam Transport) and captured in-flight in the trap, where electron and resistive cooling bring the bunch energy down to energies of some eV or even to meV (in equilibrium with the cryogenic environment), representing an overall decrease of the kinetic energy of the ions by 13 orders of magnitude. The extracted sample is sent to the experiments placed on top of the ReInjection Channel via the Vertical Beamline.

## 2.2 Highly charged ion production

The production of HCI is achieved essentially with two methods. The first one is via multiple ionization by collisions with energetic electrons; machines that exploit this principle are electron cyclotron resonance sources (ECR) or electron beam ion sources and traps (EBIS/EBIT) [McD02]. The energy required to remove bound electrons is contained in the high-energy electrons; therefore the extracted ion beams have low energies. The drawback is the limitation to moderately charged ions in the case of ECR sources and charge states $q \leq Z-2$ for EBIS/EBIT devices, since electron energies of several hundred keV would be necessary to reach species like bare uranium. Such energies are extremely difficult to achieve in these machines and only at SuperEBIT [Mar94] few $U^{92+}$ have been observed together with a large amount of highly charged uranium ions with two or more electrons.

The second method is the in-flight stripping, where a high-energy ion beam impinges on a solid target and electrons are removed by collisions with the target atoms [Bla94]. The yield of HCI attainable with stripping depends on the beam energy and species as well as on target material and thickness but, in contrast with the first method, it can be high also for heavy species [Shi82]. A typical value is 30% stripper efficiency for $U^{92+}$ with a 400-MeV/u $U^{73+}$ primary beam impinging on a copper foil of 40 $\mu g/cm^2$ [Dah04]. The GSI accelerator chain makes the application of this method possible: all nuclides up to uranium are accelerated to 11.4 MeV/u and pre-stripped (the maximum charge state is $U^{73+}$) after acceleration in the UNILAC, injected in the SIS-18 and further accelerated. After extraction out of the SIS-18 and stripping in the stripper foil, the ion sample is injected in the Experimental Storage Ring (ESR) at a typical energy of 400 MeV/u. In the ESR (see Fig. 2.4), the deceleration down to the MeV range takes place, via synchronous ramping-down of the magnetic field of the ESR dipole magnets and of the frequency of the RF system. In order to keep transverse emittance and longitudinal momentum spread small, electron cooling stages are inserted between slowdown phases [Ste04].

The feasibility of the cooling and deceleration scheme for a $U^{92+}$ beam was tested. The scheme is sketched in Fig. 2.5. As many as $5 \cdot 10^8$ particles are delivered from the SIS. A first electron cooling cycle of 10 s takes place right after injection, as the beam quality has been degraded in the interaction with

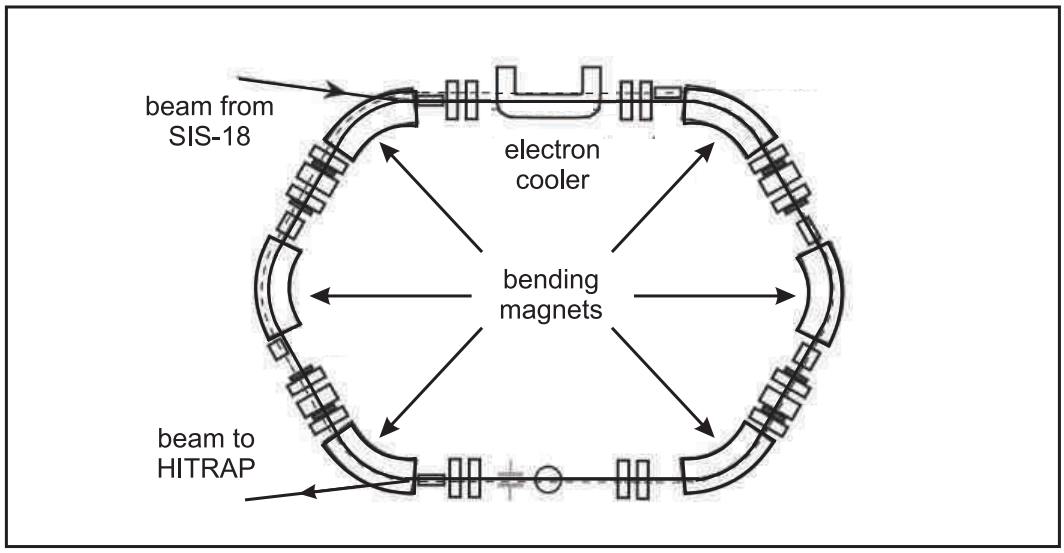


Figure 2.4: Sketch of the Experimental Storage Ring ESR. Six dipole magnets bend the beam onto a closed orbit of 108 m. One of the straight sections houses the electron cooler. Here the beam undergoes Coulomb collisions with a cold, collinear electron beam bent by a dipole magnet onto the ion trajectory and successively deviated again by a second dipole.

the stripping foil. After deceleration down to 30 MeV/u (7 s), the maximum number of particles is $5 \cdot 10^7$. Electron cooling is repeated. Only 5 s are needed since the process is more efficient at low energy. Electron cooling is applied again right before extraction, after the second deceleration stage. It has been demonstrated that with the last deceleration cycle the beam can be brought down to a minimum energy of 3 MeV/u in 5 s. The energy limit is due to the frequency range of the RF system. Since the final energy influences the losses during electron cooling, the extracted sample at 3 MeV/u is about $10^5$ ions, while stopping at 5 MeV/u $10^6$ particles can be extracted. The complete cycle is performed in $30 \div 40$ s.

The HITRAP requirement is the delivery of a bunch every 10 s. As the operation of magnets and rf systems at the lower energy limit is complicated, a final energy of 4 MeV/u has been chosen [Kes06], for which the yield is $\sim 6 \cdot 10^5$ ions. Further optimization in order to reduce the cooling cycle to 10 s is possible, for instance using stochastic cooling at 400 MeV/u instead of electron cooling. This mechanism has already been successfully demonstrated and is being integrated in the deceleration procedure.

## 2.3 The HITRAP decelerator

The beam extracted from the ESR is sent to the HITRAP facility in the ReInjection Channel (see Fig. 2.3). The limit for in-flight capture in the Cooler

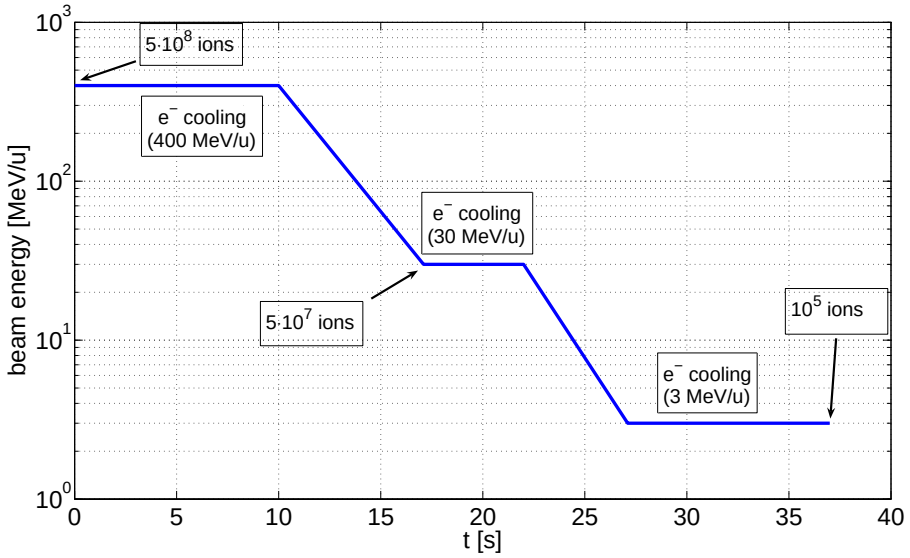


Figure 2.5: Test of deceleration and cooling cycle in the storage ring ESR. In this test, the 400-Mev/u beam delivered from the synchrotron is decelerated down to 3 MeV/u in th ESR. Electron cooling stages inserted at the beginning, at an intermediate energy of 30 MeV/u and before extraction reduce emittance and momentum spread. The complete cycle is performed in $30 \div 40$ s. Losses reduce the maximum extracted beam to $10^5$ ions for this extraction energy.

Trap (see Chapter 3 for details) is about 6 keV. One compact structure cannot efficiently decelerate the ion beam starting from an energy of 4 MeV/u down to 6 keV, therefore the task is realized in two steps. The first is accomplished in an Interdigital H-type (IH) linear decelerator, taking the energy down to 0.5 MeV/u, while a Radio Frequency Quadrupole (RFQ) will perform the second part. In order to use existing UNILAC power supplies, all HITRAP RF devices have a working frequency of 108.408 MHz (or higher harmonics of that frequency), i.e. the frequency of the UNILAC Alvarez structure.

### 2.3.1 The Double-Drift Buncher and IH-Linac

With an acceptance between 10° and 15° out of the 360° of the 9.2 ns period, the IH-Linac cannot receive efficiently the 1-$\mu$s macropulse coming out of the ESR. The ESR pulse has therefore to be bunched accordingly. It has been calculated that the task can be accomplished by a Double-Drift Buncher (DDB), consisting of two RF cavities fed by 2-kW RF generators (see Fig. 2.6). The DDB solution has been chosen as such a device is easier to operate than a multi-harmonic buncher while keeping the same bunching efficiency [Pan01]. The first cavity, a 4-gap buncher, operates at 108.408 MHz. The second cavity is a 2-gap buncher working at the second harmonic (216.816 MHz).

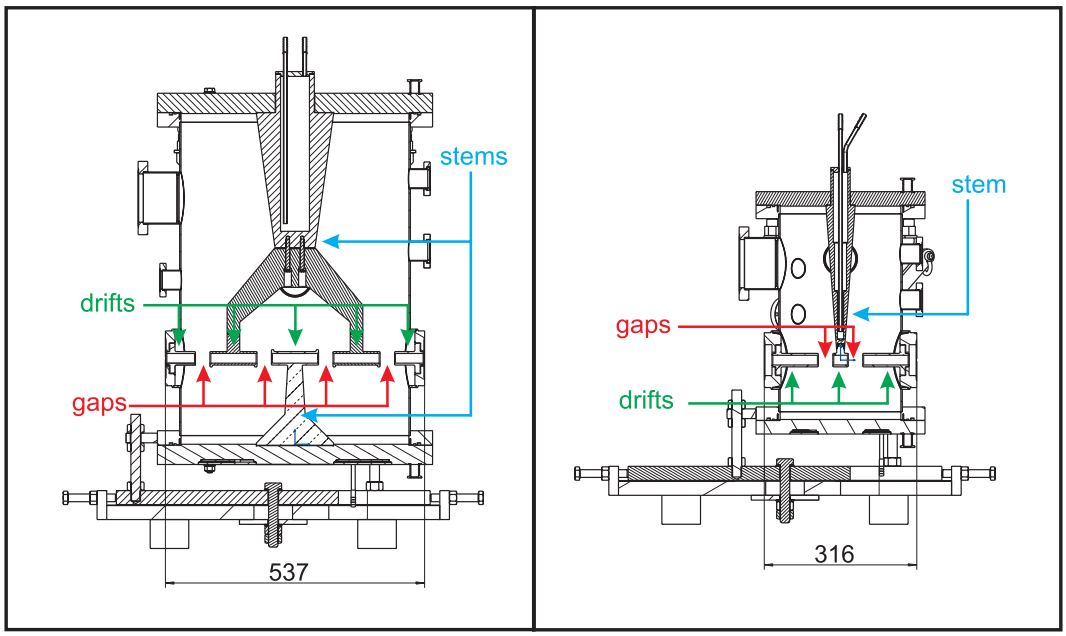


Figure 2.6: Technical drawing of the Double-Drift Buncher cavities (longitudinal section). The 4-gap 108 MHz cavity is shown on the left and the second cavity, a 2-gap buncher working at the second harmonic (216 MHz), on the right. The drift tubes are indicated with their holders (stems). All dimensions in mm. See [Dah06] for further details.

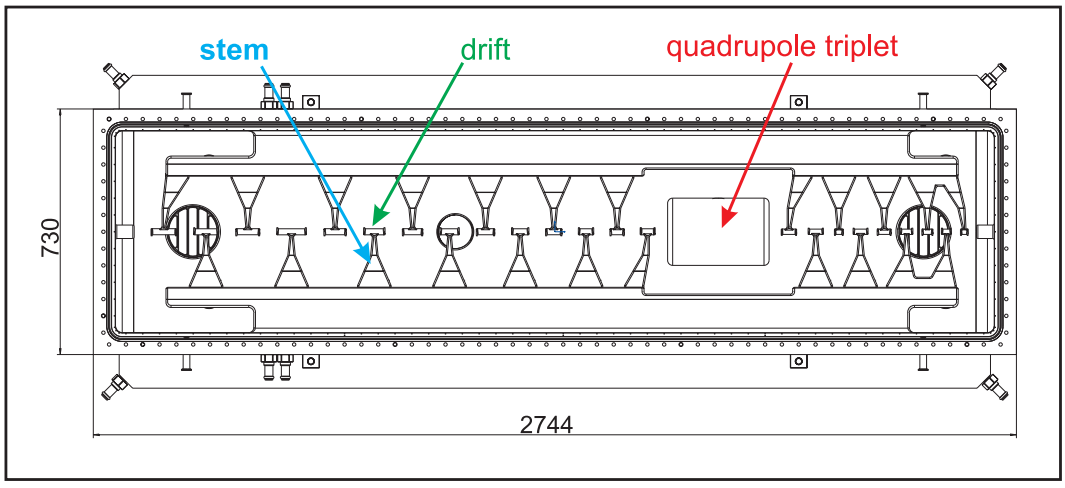


Figure 2.7: Technical drawing of the IH-linac (longitudinal section). The 25 drift tubes and their stems are visible. Notice the inner tank housing the quadrupole triplet for transverse focusing. All dimensions in mm. See [Dah06] for further details.

Table 2.1: Calculated performance of the decelerator elements [Kes06a]. The beam quality as well as the transmission for each device is reported. The overall transmission is about 55%. Notice the increase in transverse emittance, due to nonlinear beam optics effects.

| | DDB | IH | Rebuncher | RFQ & Debuncher |
|---|---|---|---|---|
| Entrance energy [MeV/u] | 4 | 4 | 0.5 | 0.5 |
| Exit energy [MeV/u] | 4 | 0.5 | 0.5 | 0.006 |
| $\beta$ exit | 0.093 | 0.033 | 0.033 | 0.0036 |
| Normalized $\varepsilon_{xx'(yy')}$ entrance [mm mrad] | 0.2 | 0.21 | 0.3 | 0.34 |
| Phase spread (entrance) [°] | 240 | 15 | 75 | 45 |
| Energy spread (entrance) [%] | 0.01 | 3.5 | 5 | 5 |
| Normalized $\varepsilon_{xx'(yy')}$ exit [mm mrad] | 0.21 | 0.3 | 0.34 | 0.36 |
| Phase spread (exit) [°] | 150 | 20 | 70 | 300 |
| Energy spread (exit) [%] | 3.5 | 6 | 5 | 8 |
| Transmission [%] | 98 | 70 | 95 | 85 |

The DDB was installed in the ReInjection Channel in 2007 (see Fig. 2.8) and was commissioned in the same year during two beamtimes where $^{64}Ni^{28+}$ and $^{20}Ne^{10+}$ beams were used. The emittance was measured with a pepper pot emittance meter at the location where the entrance of the linac will be placed. The measured rms normalized emittances were $\varepsilon^{rms}_{xx',n} = 0.207$ mm mrad and $\varepsilon^{rms}_{yy',n} = 0.249$ mm mrad. These values can be compared with the nominal specifications, reported in Table 2.1, which summarizes the expected performance of the decelerator. Since effective emittance is four times the rms value, the measured values are larger by a factor four when compared to the nominal $\varepsilon_{xx',n} = \varepsilon_{yy',n} = 0.21$ mm mrad. This enhanced value, which is within the acceptance of the DDB but not that of the IH, was due to problems in the cooling cycle of the ESR, which yielded an uncooled beam. Nevertheless, a well focused beam at the IH position was observed and a transmission of 80% was obtained, which is already close to the nominal 98% (also in Table 2.1). Bunches from both cavities operated solely or together were resolved with a set of phase probes and diamond detectors, but results are not conclusive yet and investigations will continue during the next beamtime to optimize the power and phase settings.

The IH structure is a particular type of linear accelerator. Like all linear RF machines, it is based on the application of oscillating electromagnetic fields to a series of drift tubes in a resonant cavity. The beam is subject to an accelerating force when it is outside of the drifts, while the RF phase is reversed when

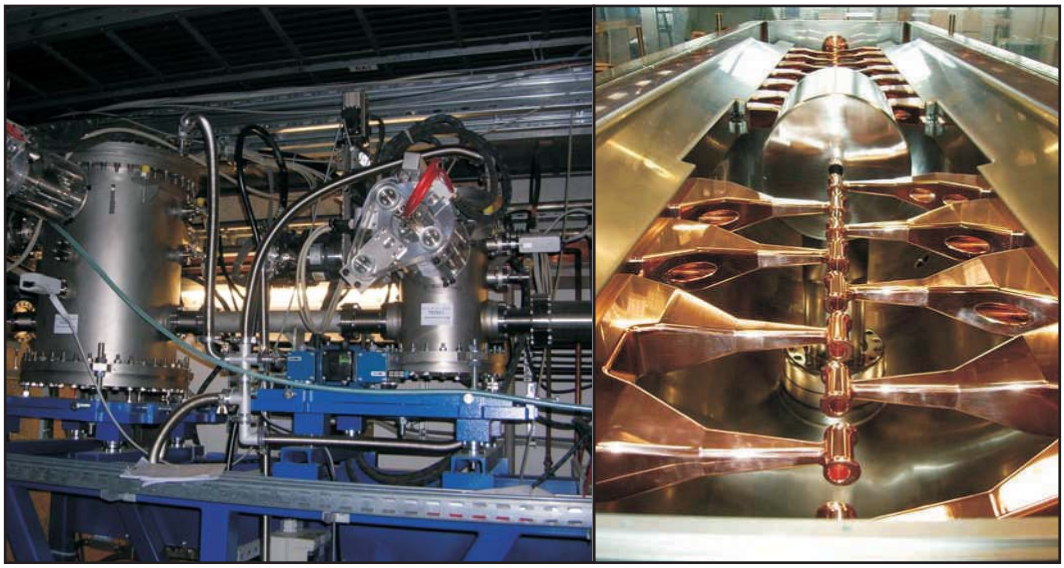

Figure 2.8: Photographs of the DDB and linac. On the left, the two cavities of the DDB as installed in the ReInjection Channel, where they were commissioned in 2007. On the right, a view of the opened linac tank, where drift tubes and housing of the quadrupole triplet are visible. The linac is now also installed in the Channel and its commissioning is about to start.

the beam is passing through the drifts and is therefore shielded. The length of the drift tubes is progressively shortened from the injection to the extraction end so that beam and RF are always in phase. In this way a net acceleration is achieved [Rat98, Wan98]. In a very simplified picture, deceleration is obtained with the same scheme but inverting both the RF phase and the placement of the drift tubes. The HITRAP IH-Linac [Dah04] consists of a 2.7-m long stainless steel tank with 25 gaps and an internal quadrupole triplet lens for transverse focusing (see Fig. 2.7 and 2.8). Each element is copper plated. As previously said, existing power supplies had to be used. The linac works therefore at a frequency of 108.408 MHz, with a peak power below 200 kW, which is within the specifications. In order to decelerate species with mass-to-charge ratio m/q$\leq$ 3 down to 0.5 MeV/u, an overall effective voltage of 10.5 MV is required. The calculated transmission is 70%. Tuning and power conditioning are under way and the machine will be commissioned in a dedicated beamtime during August 2008.

### 2.3.2 The Radio Frequency Quadrupole Decelerator

An RFQ decelerator is a 4-vane or 4-rod structure where RF electric fields applied to four rods with a proper longitudinal modulation provide both an effective transverse confining potential and a longitudinal acceleration or deceleration [Wan98]. The design and construction of the HITRAP RFQ is the

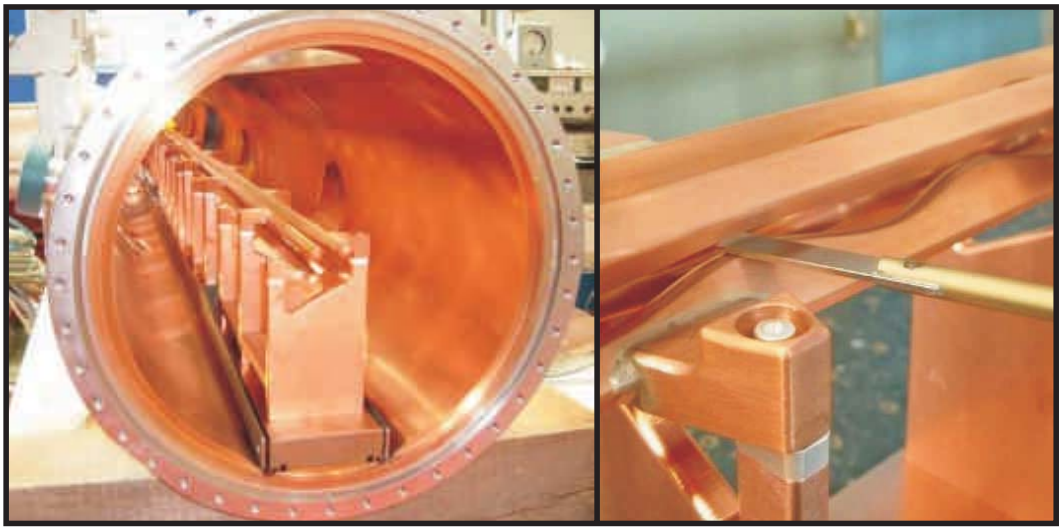

Figure 2.9: Photograph of the internal structure of the RFQ. On the left, the open RFQ tank shows the four-rod structure. On the right, the detail shows the sinusoidal modulation of the rods.

subject of B. Hofmann's PhD thesis [Hof08]. This RFQ is a 4-rod structure (see Fig. 2.9), which follows closely the design of the High Charge Injector at GSI [Fri91]. The fact of being designed for species with $m/q \leq 3$ allows a relatively short length of 1.99 m. The maximum rod voltage is 77.5 kV.

The phase width of the beam arriving from the IH-Linac (45°) must be matched to the RFQ acceptance (20°). An existing 2-gap spiral rebuncher was adapted to our set-up and installed in front of the RFQ itself. Its nominal 95% efficiency. Since efficient trapping in the Cooler Trap requires a low energy spread, a single harmonic debuncher is installed behind the RFQ. According to calculations, the debuncher reduces the beam spread from ±7% to ±4%. Due to nonlinearities, the transverse emittance is estimated to be as high as 100 mm mrad in both directions. The calculated combined efficiency of the RFQ and debuncher is 85%. The complete structure has been assembled. Power conditioning is ongoing and the commissioning will take place in a dedicated beamtime during October 2008.

Summarizing, we can have an overall view of the expected performance of the decelerator section looking again at Table 2.1. The HITRAP decelerator accomplishes the task of beam deceleration from 4 MeV/u to 6 keV/u. The evident increase in transverse emittance can be explained, as already said, as an effect of nonlinearities in the beam optics. Injecting some $10^5$ ions from the ESR at 4 MeV/u, the overall transmission efficiency about 55% guarantees that at least $10^5$ HCI can be delivered to the low-energy part of HITRAP.

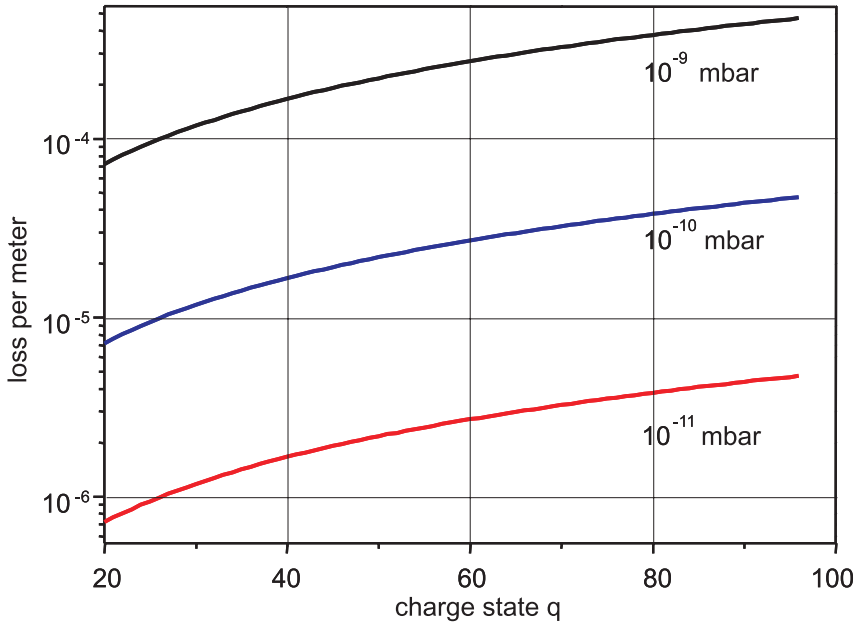


Figure 2.10: Charge exchange loss as a function of charge state $q$ for ion energies below 25 keV/u, according to the Schlachter model [Sch84]. In this model, no dependence on the velocity is taken into account.

## 2.4 The low-energy section

The low-energy section performs the last part of the bunch manipulation, i.e. cooling it to the low energies requested by the experiments. The Low-Energy Beam Transport (LEBT) line connects the RFQ to the Cooler Trap, where cooling of the bunch takes place. The beam is then guided to the experiments on the upper-floor platform via the Vertical Beamline.

### 2.4.1 The Low-Energy Beam Transport line

The vacuum specifications of the decelerator require a standard ultrahigh vacuum (UHV) value of $10^{-8}$ mbar. On the contrary, the Cooler Trap stores the ion bunch for a time not shorter than 10 s in order to perform the cooling to 4 K. Therefore charge-exchange reactions [Sch84, Man86] cannot be ignored and set more stringent vacuum conditions. No experimental data exist for HCI at energy in the keV regime. For energies between 10 eV and 25 keV/u, the cross section for one-electron capture is described by the velocity-independent semi-empirical formula [Sch84]

$$\sigma_{q,q-1} = 1.43 \cdot 10^{-12} q^{1.17} I^{-2.76} \; [cm^2], \tag{2.1}$$

where $q$ is the ion initial charge state and $I$ the ionization potential of the residual gas. The result for $U^{92+}$ is a cross section of $5 \cdot 10^{-13}$ cm$^2$. The losses

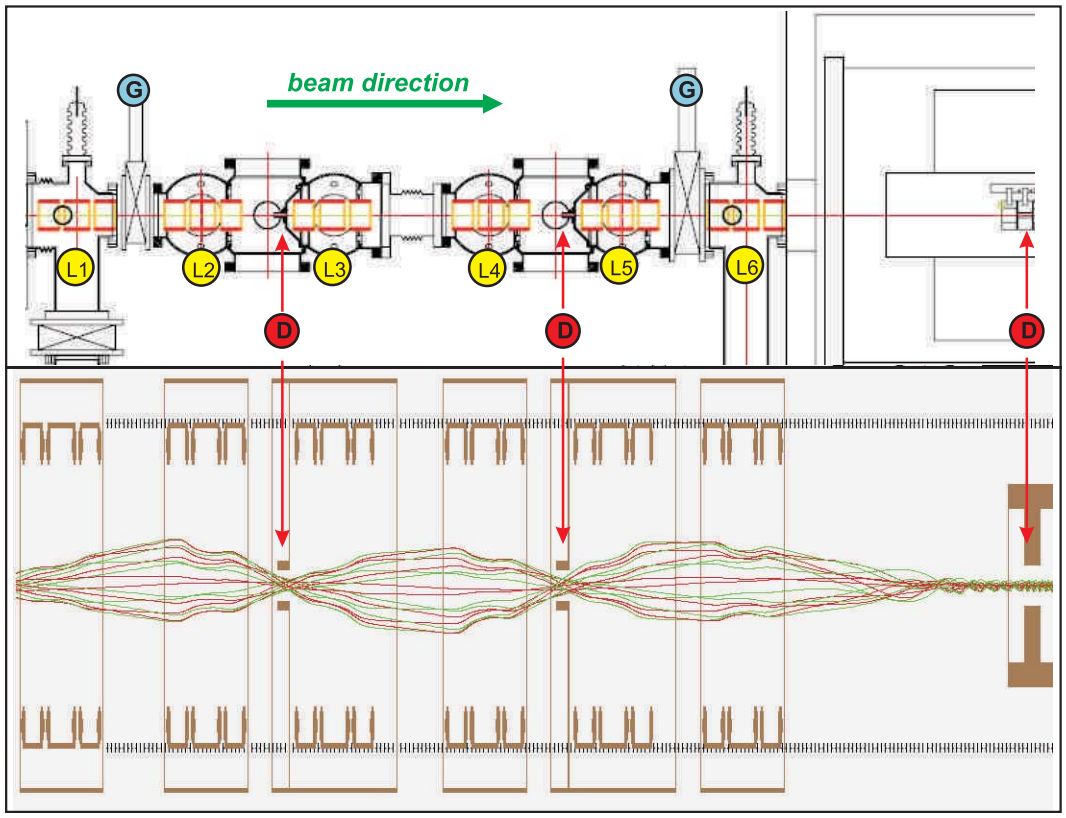


Figure 2.11: The LEBT line. The upper part shows a technical drawing of the beamline. L1÷L6 indicate the Einzel lenses, D the position of the diaphragms and G the gate valves. The lower part shows a simulation of the ion bunch transmission through the beamline. The beam, going from left to right, is focused through the diaphragms and injected in the trap, whose first electrodes are visible on the right. The third diaphragm is represented by the endcap electrode (see next Sec. 2.4.2 and 5.2.2 for details on the electrode stack).

per meter as a function of $q$ are plotted in Fig. 2.10. A pressure of $10^{-9}$ mbar gives losses of about 0.1%/m. It can be estimated that in order to store for at least 10 s a bunch of $U^{92+}$ ions with losses below $10^{-3}$, the pressure in the trap should be as low as $10^{-13}$ mbar [Her05].

The purpose of the LEBT is therefore twofold: focusing of the beam for injection in the Cooler Trap and vacuum separation between the RFQ and the trap itself. Figure 2.11 shows a scheme of the LEBT and the corresponding beam optics. Two diaphragms are located along the LEBT line, acting as differential pumping barriers, and a third diaphragm is represented by the endcap of the Cooler Trap. Focusing the beam in the two 8-mm diameter diaphragms is obtained by the use of three doublets of electrostatic cylindrical lenses. Einzel lenses have been preferred to quadrupoles because of the large beam emittance. Ion-optical simulations yielded an injection into the trap with

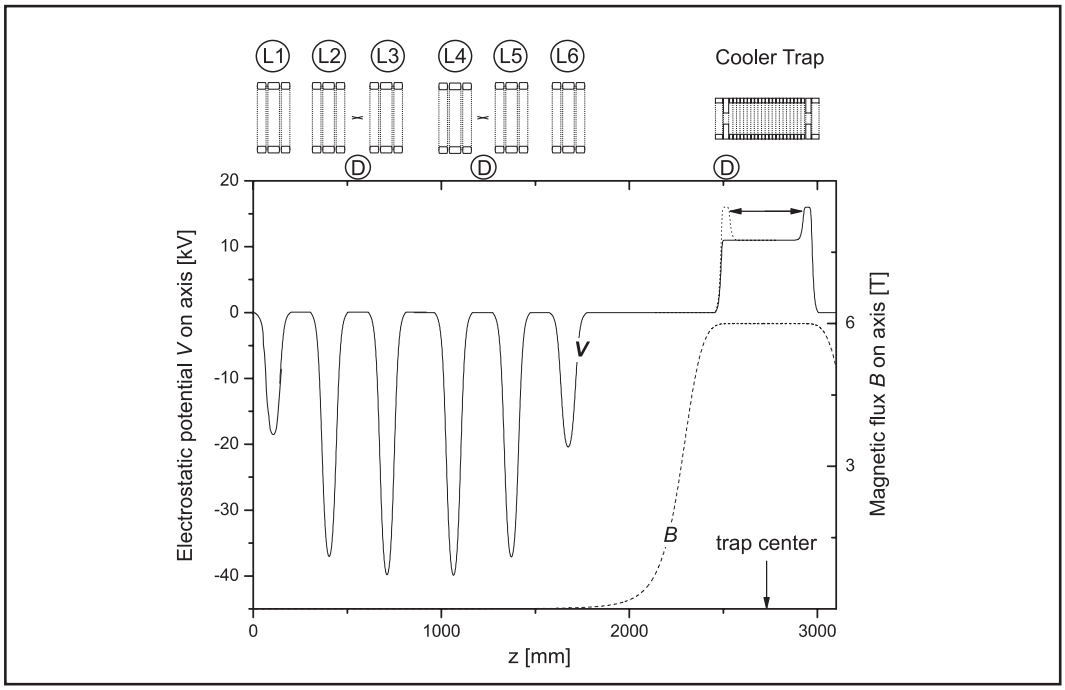


Figure 2.12: Electrostatic potential and magnetic field on the axis of the Low-Energy Beam Transport line and Cooler Trap. In the upper part, the beamline lenses (L1÷L6), the Cooler Trap and the diaphragms (D) are sketched to indicate their position (sketch not to scale). The last diaphragm is the trap endcap. In the diagram, the solid line represents the electrostatic potential and the dashed line the magnetic field of the solenoid within which the trap is inserted.

a rms radius (then freezed due to the magnetic field) of about 0.7 mm and an optical transmission above 90% with the potential distribution depicted in Fig. 2.12 [Her05]. We expect to reach a better transmission, as the calculations so far took into account a non-optimized output beam from the RFQ.

Further details on the vacuum specifications for the LEBT and the Cooler Trap come in Sec. 5.1, where the slope of the pressure along the beamline is calculated. In brief, the pressure in the LEBT must decrease from $10^{-9}$ mbar on the RFQ side to $10^{-11}$ mbar on the trap side. Two turbopumps with a pumping speed of 300 l/s and two ion-getter pumps will be used for the purpose. The turbopumps will be located on the flanges housing lenses 1 and 6, the ion-getter devices will be connected to the vessels at the position of lenses 2 and 4. The central electrode of each Einzel lens is made out of a grid to facilitate efficient pumping of the inner chamber. Two diagnostics stations including a Faraday cup, a micro-channel plate and a digital camera each are housed respectively between lens 2 and 3 and between lens 4 and 5, at the positions of the diaphragms. The exit electrode of lenses 2 to 5 are radially 4-fold split for beam deflection.

The whole LEBT line is bakeable at 200°. Baking tests on all elements

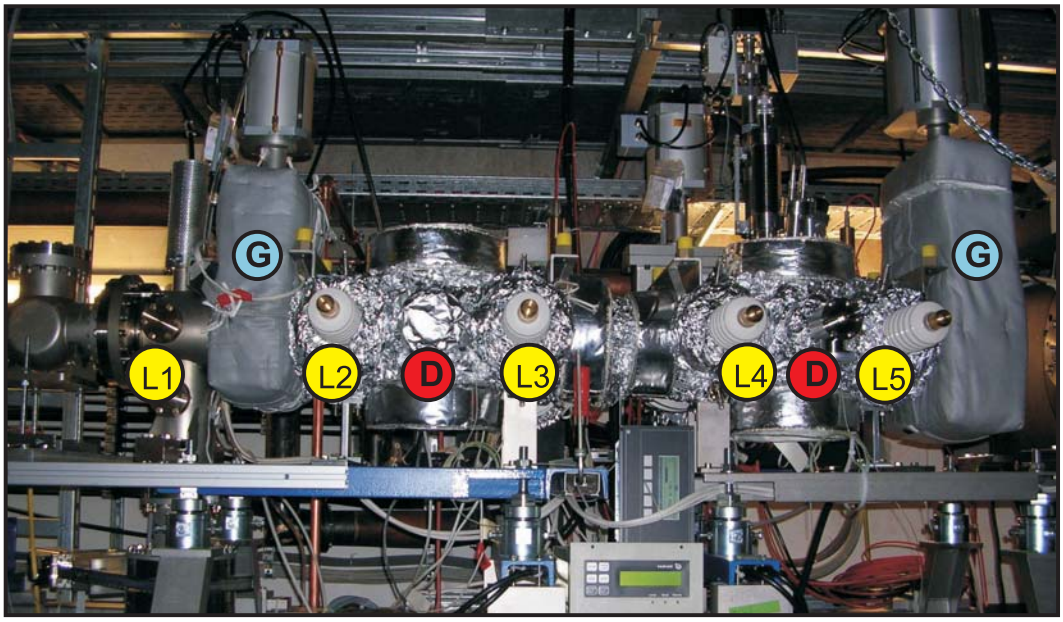


Figure 2.13: Photograph of the LEBT line as installed in the ReInjection Channel. The position of the lenses (L1÷L5. L6 is not visible), diaphragms (D) and gate valves (G) is indicated.

have been performed successfully and the beamline has been mounted in the ReInjection Channel (see Fig. 2.13), where transmission tests with a $H_2$/He ion source (see Sec. 5.4) are about to start.

### 2.4.2 The Cooler Trap

In the following, a concise description of trapping principles and main features of the Cooler Trap is given. The physical design will be the subject of Chapter 3, while Chapter 5 will be devoted to the discussion of the technical design.

A Penning trap is a device where charged particles are confined thanks to the combination of electric and magnetic fields. The axial confinement is provided by a quadrupole electrostatic potential of the form $V \propto V_o\,(z^2 - r^2/2)$, generated by applying a voltage between two endcap electrodes and a central ring. In the easiest technical solution, the electrodes are simple cylinders (cylindrical Penning trap). Since a three-dimensional confinement cannot be achieved with electrostatic fields only, a solenoid is placed around the trap. The longitudinally directed magnetic field $\vec{B} = B\hat{z}$ exerts a Lorentz force in the radial plane, thus providing stable trapping.

It can be shown that the ion motion in a Penning trap is the superposition of three eigenmotions: an axial bounce with frequency $\omega_z = \sqrt{qV_o/md^2}$ (where $d$ is a geometrical trap parameter), and a linear composition of two radial motions called reduced cyclotron (frequency $\omega_+$) and magnetron ($\omega_-$).

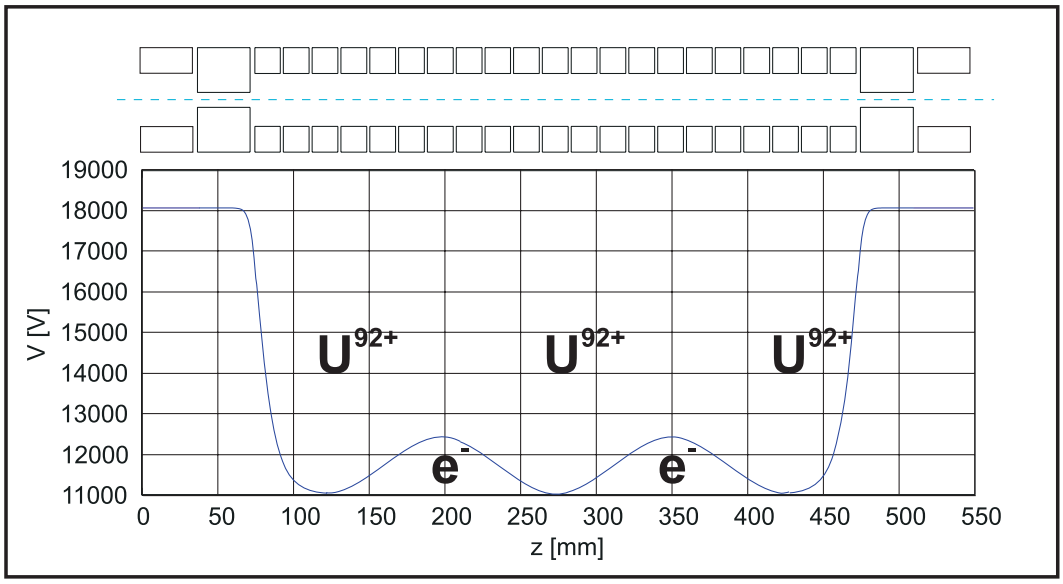


Figure 2.14: Nested trap configuration of the Cooler Trap. In the upper part, a section of the electrode stack of the Cooler Trap. The diagram below shows the electric potential (only indicative) on the longitudinal axis. Simultaneous trapping of positive and negative charges can be achieved in the nested hills and wells.

The requirements for the Cooler Trap are challenging and determine its special design. The trap must catch and store $10^5$ highly charged ions every 10 s. $10^9 \div 10^{10}$ electrons have to be confined at the same time in the trap in order to perform electron cooling of the hot ion cloud.

A small ideal trap with hyperboloidal geometry (see Sec. 3.1) is not suited for in-flight capture of incoming bunches of particles with an energy in the keV range. A cylindrical, axially-elongated structure allows the ion pulse to reach the farther endcap electrode and be completely trapped by rising the potential on the first endcap before it is reflected and escapes again. On the one hand, the performance of the decelerator sets the lowest energy achievable at the injection. On the other hand, the length of the trap is limited by the financial cost of the superconducting magnet which, with a field strength of 6 T, provides the radial confinement (see Sec. 5.2.1). We will see in Sec. 3.3 that efficient trapping is achieved with an effective trapping length of 400 mm when the bunch energy is about 6 keV.

Simultaneous storage of particles of opposite sign is possible in a so-called *Mutli-Ring Trap* (MRT), i.e. a cylindrical trap with several inner electrodes. Applying proper voltages to the electrodes, inner hills and wells of the electric potential *nested traps* can be created. Therefore both positive ions and electrons are stored in the adjacent nested traps. This technique has been already exploited in other trap facilities, like the set-ups for confinement of antiprotons and positrons at CERN (ASACUSA [Ich01], ATHENA [Amo04],

ATRAP [Gab99]). Fig. 2.14 shows a sketch of the Cooler Trap electrodes and the nested-trap potential configuration.

At low relative energy, the recombination rate between electrons and ions would become the dominant process and the charge state of the ions would be altered. Therefore electron cooling is stopped and resistive cooling is foreseen for the last part of the cooling process. The lower energy limit for the resistive cooling is set by the temperature of the cooling circuit. Therefore the complete trap set-up will be in thermal contact with the superconducting magnet at 4 K. An extensive discussion of the cooling processes is given in Chapter 4.

We have already mentioned the stringent vacuum requirements of the trap, namely a pressure better than $10^{-13}$ mbar. In addition to endcaps with a reduced inner diameter which act as differential pumping barriers, the cryogenic temperature will have beneficial effects since it will freeze most of the possible contaminants. For further details on the trap vacuum, see Sec. 5.1.

### 2.4.3 The Vertical Beamline and EBIT

The HITRAP experiments presented in Sec. 2.5 require beams with different characteristics: while trap set-ups need short bunches in order to catch the ion sample in-flight, collision expreriments will request continuous beams. Therefore different extraction modes are envisaged for the cooled sample: *pulsed*, i.e. fast extraction in a bunch by rapid switching of the trapping voltages, or *quasi-continuous*, i.e. with a leakage of ions from the trap obtained by slow lowering of the electrode voltages.

The Vertical Beamline transfers the beam extracted from the Cooler Trap 4.85 m up to the experimental platform, crossing the concrete shielding. In order to steer the desired ion species upwards and simultaneously clean the ion fraction recombined in the Cooler Trap, an existing 90° double focusing dipole magnet is employed. On the upper floor a spherical electrostatic bender redirects the beam to the experimental setups. The choice of a spherical bender guarantees a transverse focusing in both the horizontal and vertical direction and therefore a symmetric beam. All other optical elements are electrostatic (see Fig. 2.15). The same type of diagnostics is used as in the LEBT line (see Sec. 2.4.1). Also similar are the vacuum considerations, based on the charge exchange model by Schlachter. As Fig. 2.10 shows, reduction of charge exchange along such a long beamline demands a vacuum of $10^{-10}$ mbar to keep losses in the order of $10^{-4}$ over the length of 10 m. Ion getter pumps will be employed. Since active pumping is not possible in the 1.6-m long pipe crossing the concrete shielding, this free-drift section will be coated with non-evaporable getter (NEG) in order to reduce the outgassing surface [Her05].

Due to the limited availability of beam from the ESR, it is desirable to have an offline source. For this reason it is foreseen to use an Electron Beam Ion Trap (EBIT) as highly-charged ion source to perform both tests and measurements on medium-weight HCI. This EBIT is a room-temperature commercial device

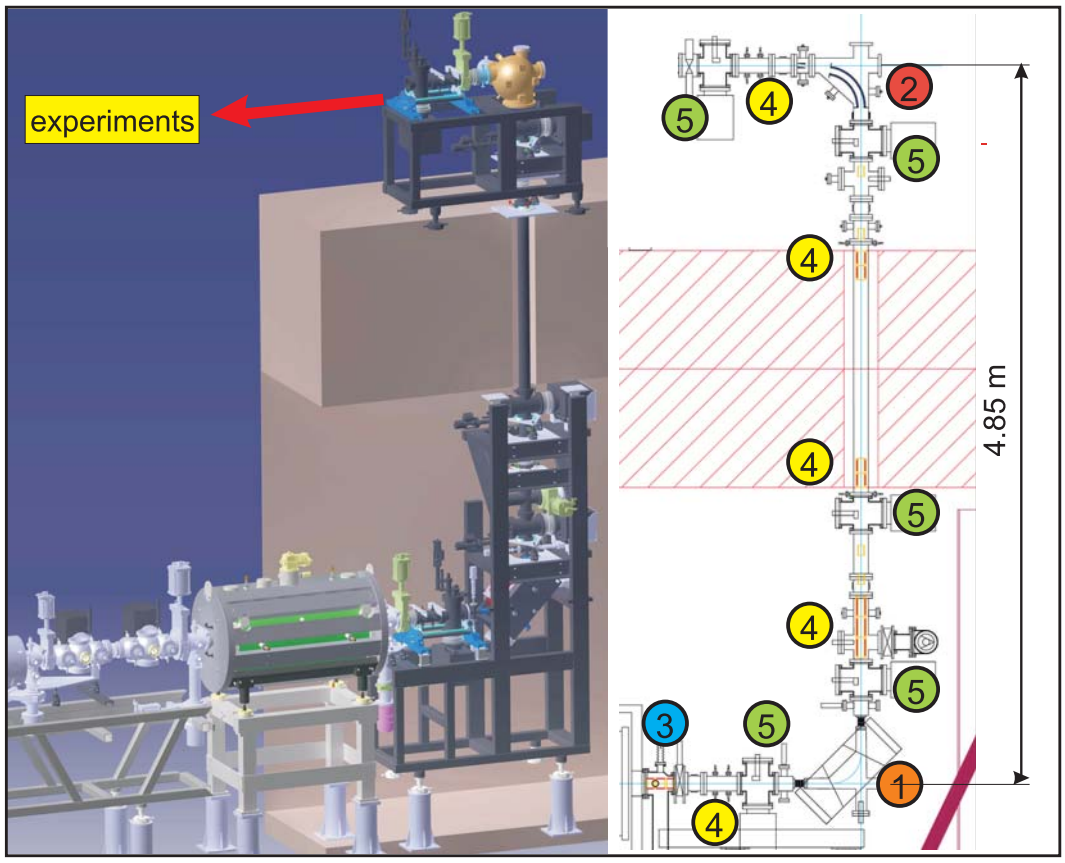


Figure 2.15: Vertical Beamline. The beam extracted from the Cooler Trap is bent upwards by a 90° magnet (1). It crosses the shielding and is then bent horizontally towards the experimental platform by an electrostatic kicker-bender (2). All other focusing elements (Einzel lenses (3), quadrupoles (4)) are electrostatic. Diagnostic and pumping stations are indicated (5).

which can provide highly charged ions up to $Ar^{18+}$ or $Xe^{46+}$ either in pulsed or DC mode [DRE08]. The EBIT will be placed on the roof of the ReInjection Channel, aside of the spherical bender and perpendicular to the beamline guiding the cooled beam to the experiments. An electrostatic kicker, combined with the bender, will inject the beam extracted from the EBIT in the Vertical Beamline, whose design allows also transport back to the Cooler Trap for preparation of the ion sample before redirection to the experiments.

## 2.5 HITRAP experiments

HITRAP gives access to a large variety of experiments which were, to a large extent, developed in the EU RTD network HITRAP during 2001-2006. These are briefly treated in the following.

### 2.5.1 Mass measurements

As one of the most unique and fundamental properties of a nuclide, masses constitute a source of primary interest, both for stable and unstable species. Indeed, the knowledge of masses provides insight into the nuclear structure: binding energies, $Q$-values can be extracted from the comparison between different nuclides. High-accuracy data have therefore an impact on a wide range of fields. For instance, masses are one of the key parameters for a correct description of the stellar nucleosynthesis processes [Arn99, Sch06]. They offer input for the verification of the Conserved-Vector-Current (CVC) hypothesis and the unitarity of the Cabibbo-Kobayashi-Maskawa (CKM) matrix, crucial points within the Standard Model [Har01]. QED tests are possible by measurement of masses with highest accuracy.

The extended storage time makes Penning traps an excellent tool for mass spectrometry. A mass value is determined exploiting the ion eigenmotions in a trap, as it can be derived from the definition of cyclotron frequency $\omega_c = qB/m$ and the relation $\omega_c = \omega_+ + \omega_-$ for an ideal trap or $\omega_c^2 = \omega_z^2 + \omega_+^2 + \omega_-^2$ (invariance theorem) for a real trap. The magnetic field strength $B$ is accurately determined by measuring the frequency of a well-known reference mass $m_{ref}$, yielding the proportionality

$$\frac{m_i}{m_{ref}} = \frac{\omega_{ref}}{\omega_i}. \tag{2.2}$$

The cyclotron frequency is obtained either by destructive methods (TOF, Time-Of-Flight) or by single-ion non-destructive techniques via detection of the induced image charges [Bla06]. With the latter, relative accuracies in the order of $10^{-11}$ have been achieved on singly charged ions [Bra99]. Since the mass resolving power reads

$$R = \frac{m}{\Delta m} = \frac{\omega_c}{\Delta \omega_c}, \tag{2.3}$$

it is clear that the use of highly charged ions can significantly improve the accuracy of mass measurements, although at HITRAP the range of investigations is going to be limited by the deceleration and cooling cycle to stable nuclei and unstable isotopes with half-life $\geq 10$ s. A Penning trap devoted to this purpose is under development in Mainz with the close collaboration of GSI [Her06]. The aim is an uncertainty $\delta m/m < 10^{-11}$.

### 2.5.2 *g-factor* measurements

Another innovative trap setup for *g-factor* measurements has been developed by the Mainz-GSI collaboration and will be part of the HITRAP physics program [Alo07]. The determination of the electron *g-factor* bound in a hydrogen-like ion represents a sensitive test of QED [Bei00]. $g_{bound}$ can be written

$$g_{bound} = 2\frac{q}{e}\frac{m_e}{M_i}\frac{\omega_L}{\omega_c}, \tag{2.4}$$

where $m_e$, $M_i$ are the masses of the electron and the ion, respectively, and $e$, $q$ their charges. $\omega_L$ is the Larmor (i.e. spin precession) frequency and $\omega_c$ the cyclotron frequency. The set-up consists of two traps: the so-called 'precision trap' in a very homogeneous magnetic field and the 'analysis trap' where a ring made of nickel creates a magnetic bottle, i.e. a quadratic inhomogeneity of the type $B_2 z^2$ [Häf03]. While $\omega_c$ can be measured by means of the induced image currents in the precision trap, $\omega_L$ is determined as follows. A particle placed in the analysis trap experiences a magnetic potential with different sign for the two spin directions. This results in a different force proportional to $\mu \partial B/\partial z$ (with $\mu$ magnetic moment of the particle) and hence in a different axial frequency (*continuous Stern-Gerlach effect*). Spin flips on a single ion are induced via resonant excitation in the precision trap and the ion is transported to the analysis trap, where spin flips can therefore be detected. $\omega_L$ is determined as the excitation frequency that yields more spin-flip events. *g-factors* obtained in experiments on $^{16}C^{5+}$ [Häf03] and $^{16}O^{7+}$ [Ver04] showed a perfect agreement with the theoretical value, yielding a relative accuracy in the order of $10^{-9}$. Using then the theoretical value of $g$ and inverting Eq. (2.4), the mass of the electron can be determined more accurately [Bei03a]. The CODATA group gives now the uncertaninty of the electron mass with $\delta m/m \sim 6 \cdot 10^{-10}$, about five times better than the previously accepted value [Moh08]. The same accuracy is expected for the upcoming experiments on uranium at HITRAP. This might yield a new value for the fine structure constant $\alpha$ [Sha06] with a higher accuracy than the value obtained from the 3.7 ppm measurement of *g-2* of the free electron by the Seattle group [Dyc87]. However, it should be noted that the Harvard group very recently improved the uncertainty in $\alpha$ to 0.37 ppb [Han08]. Althought a determination of the fine structure constant from the *g-factor* of the bound electron cannot reach presently the accuracy of that from the *g-factor* of the free electron, such a measurement would yield a completely independently obtained value for this important fundamental constant.

### 2.5.3 Laser spectroscopy

The energy of ground-state hyperfine splitting (HFS) scales with the atomic number $Z$ as $Z^3$. This means that in heavy and highly charged ions ($Z > 60$) the wavelength enters the optical region and laser spectroscopy is possible. Moreover, the lifetime of the optically-pumped excited state scales as $Z^{-9}$, therefore the fluorescence rate from magnetic dipole (M1) transitions is strongly increased for heavy HCI. Accurate measurements of this transition in hydrogen-like and helium-like ions of the same species rule out to first order the nuclear effects and allow the verification of bound-state QED effects on the atomic structure. So far, experiments have been performed at storage rings [Kla94, See98], where the Doppler effect drastically reduced the level of accuracy, or in an EBIT [Cre96, Cre98, Bei01], where the limitation was the

poor signal-to-noise ratio.

The RETRAP [Gru05] setup has been moved from Berkeley to GSI and will house a new Penning trap with a mesh electrode as central ring to allow detection of the transition fluorescence. In this new setup, baptized SPECTRAP (SPECtroscopy TRAP) and collecting the effort of GSI, Imperial College (London), TU Darmstadt, University of Münster, Lawrence Berkeley and Lawrence Livermore National Laboratories and Texas A&M University, the measurement will profit from the high density of particles (attainable in a trap via *rotating wall* compression [Gre00]) and their low energy, which reduces the Doppler shift and broadening. The resulting accuracy is expected to be three orders of magnitude better than previously ever achieved [Vog05].

### 2.5.4 Reactions

Collision experiments reveal fundamental details of interactions as well as of the atomic structure. In an experimental set-up being prepared by KVI Groningen and the universities of Krakow, Vienna and St. Petersburg, the energy deposition on a surface will be addressed [Lem05]. Electron emission as a function of charge state and energy of the ions and the properties of the surface [Khe98] will be investigated, as well as the predicted, but up to now experimentally not observed, *trampoline effect*, i.e. the repulsion between the ionized surface and the partially recombined, but still positively charged, impinging ion [Bri96]. The formation and decay of *hollow atoms*, i.e. multiply excited states, will be studied by means of X-ray spectroscopy to acquire new information about level schemes in HCI.

Another precision spectroscopy tool that will be used at HITRAP is the *reaction microscope* built up at MPI-K Heidelberg. In this setup, collisions between highly charged ions and a gas jet will be studied with the COLTRIMS (COLd Target Recoil Ion Momentum Spectroscopy) technique [Ull03]. The set of detectors will track projectile, recoil ion and electrons, offering a complete reconstruction of the kinematics of the charge exchange processes, which dominate at low energy [Dör00]. X-ray spectroscopy of highly charged ions will be used in combination with this setup, too, thanks to a series of solid-state detectors.

# Chapter 3

# Physics and design of the Cooler Trap

Capture, storage and cooling of some $10^5$ highly charged ions with an initial energy in the keV/u range, as well as simultaneous loading of $10^9 \div 10^{10}$ electrons, set specific requirements for the trap size, its internal structure and the electromagnetic confining fields. This chapter deals with the theoretical and computational analysis that brought to the actual configuration. First, the physics of Penning traps in general is presented. Confinement and motion of a charged particle are discussed as well as the the collective behaviour of a large ensemble of ions. Then we elaborate the specific constraints for the Cooler Trap and the consequent choices. Finally, we present the simulation tools that have been chosen and developed to study the processes taking place in the Cooler Trap itself.

## 3.1 Penning trap basics

The Laplace equation $\nabla^2 V = -\nabla \vec{E} = 0$ forbids the confinement of a charged particle with an electrostatic field, since not all of the field components can have the same sign, i.e. confinement in one direction implies deconfinement in another one at least (this is also known as *Earnshaw's theorem* [Ear42]). There are two ways to obtain storage in three dimensions. The first is the use of time-varying electric fields (Paul trap [Pau53]), that create an effective confining potential. The alternative solution is the use of a combination of static fields, both electric and magnetic. The most straightforward *Penning-Malmberg trap* is a long cylindrical conductor (grounded) with two plates or rings (*endcaps*) at the extremities [Mal75]. A voltage applied to the endcaps provides trapping along the symmetry axis $z$. The complete setup is immersed in the axial magnetic field generated by an outer solenoid, that provides radial confinement via the Lorentz force

$$\vec{F}_L = q\vec{v} \times \vec{B}. \tag{3.1}$$

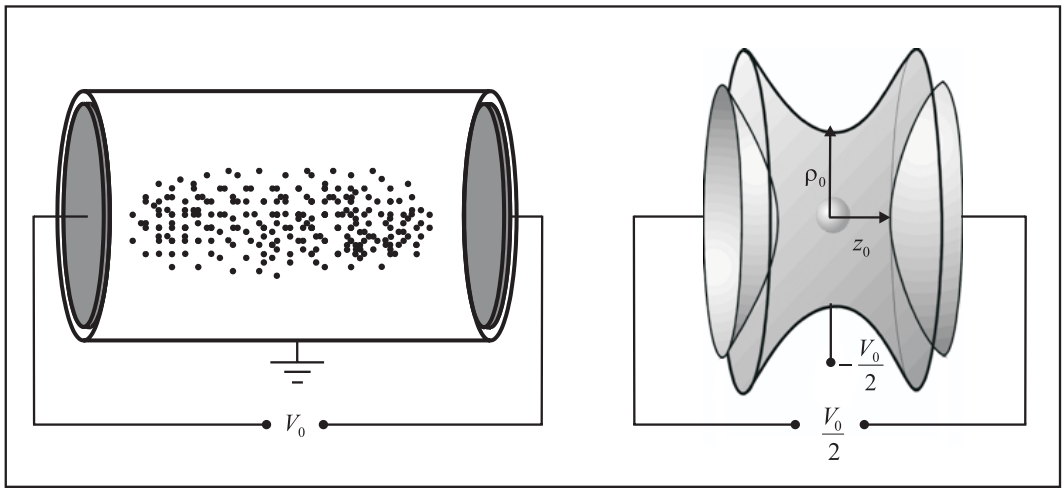


Figure 3.1: Penning trap schematics. On the left, the cylindrical Penning-Malmberg trap used by plasma physicists to confine large samples of particles (plasma columns). On the right, the hyperboloidal Penning trap, customary in atomic physics for high-accuracy investigations on a single or few particles.

Since $F_L$ acts in the transverse plane, a charged particle cannot drift radially, but performs gyrations along the B-field lines. This device, sketched on the left of Fig. 3.1, has been used extensively in plasma physics to confine large amounts of electrons and later ions.

Atomic physicists have been using a somewhat different and more sophisticated type of device, i.e. a high-precision trap whose central ring and endcaps have hyperbolical shape (Fig. 3.1, on the right). A first complete description of the confinement of charged particles in a combination of a quadrupole electrostatic field and a magnetic field was devised by J.R. Pierce [Pie49]. The Nobel laureate H.G. Dehmelt successively developed the hyperboloidal trap and for the first time realized experiments on charged particles confined with it [Deh58, Deh67, Deh68, Deh69]. In a hyperboloidal trap, the electrostatic potential has exactly a quadrupole shape and an analytical treatment can show that the dynamics of a charged particle in this volume is decomposed into three periodic eigenmotions with well-defined frequencies [Bro86]. The electrostatic potential

$$V = \frac{1}{2}\frac{V_o}{d_o^2}\left(z^2 - \frac{1}{2}r^2\right) \tag{3.2}$$

makes the particle bounce with an axial sinusoidal motion of frequency

$$\omega_z = \sqrt{\frac{qV_o}{md_o^2}} \tag{3.3}$$

depending on the geometry ($d_o = \frac{1}{2}\sqrt{z_o^2 + \rho_o^2/2}$) of the trap, the applied potential $V_o$ and the mass-to-charge ratio of the particle, but not on the energy of

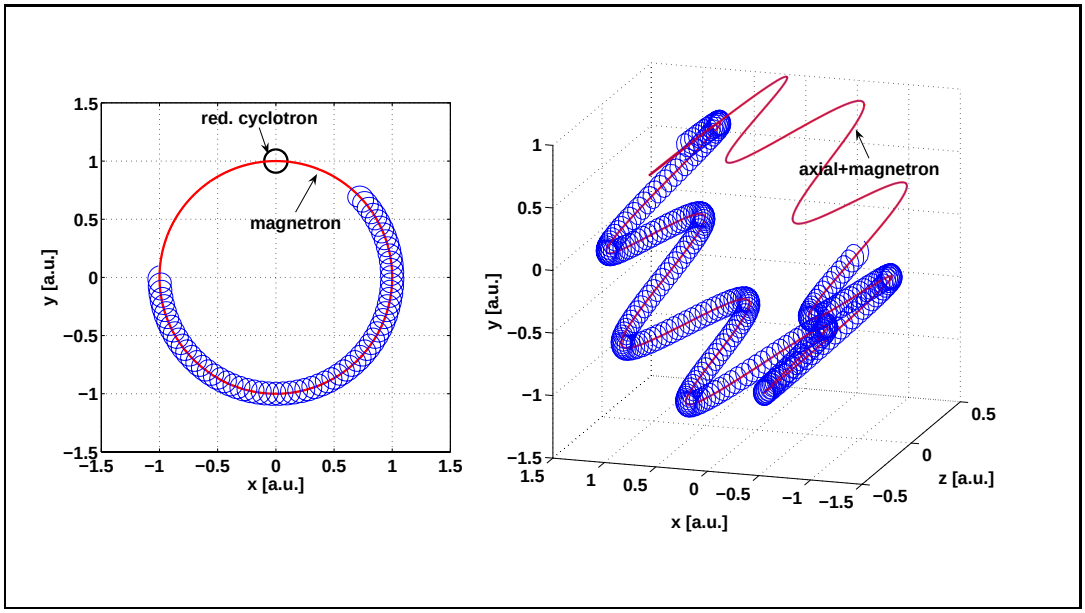


Figure 3.2: Ion motions in a Penning trap. On the left, the motions in the radial plane. On the right, the composition of the three motions in 3D.

the particle itself. This important feature can be exploited for resonant detection and manipulation. Similar considerations hold for the radial motion: in a pure magnetic field, the ion follows a closed circular orbit in the orthogonal plane (or a spiral if it has a velocity component along $\vec{B}$), called *cyclotron motion*, with frequency

$$\omega_c = \frac{qB}{m}; \tag{3.4}$$

the simultaneous presence of an electric field alters the radial motion adding an $\vec{E} \times \vec{B}$ circular drift, called *magnetron motion*. The result is the separation of the pure cyclotron rotation in two superimposed motions, the *reduced cyclotron* (slight alteration of the pure cyclotron, with frequency $\omega_+$) and the slow magnetron drift around the symmetry axis with frequency $\omega_-$. Finally we have an epicycloid in the radial plane (see Fig. 3.2). The frequency values are

$$\omega_\pm = \frac{\omega_c}{2} \pm \sqrt{\frac{\omega_c^2}{4} - \frac{\omega_z^2}{2}}, \tag{3.5}$$

and generally the fields are chosen such that $\omega_c \approx \omega_+ >> \omega_z >> \omega_-$. As previously mentioned when mass and *g-factor* measurements were discussed (see Sec. 2.5), detection and manipulation of trapped particles is possible exploiting the three eigenfrequencies and the relations connecting them: $\omega_c = \omega_+ + \omega_-$, $\omega_c^2 = \omega_z^2 + \omega_+^2 + \omega_-^2$ (*invariance theorem* [Bro86]). As an example, not only determination of the ions' properties is achieved via resonant detection, but also excitation at the sum of two eigenfrequencies results in a periodic energy

transfer between the the different eigenmotions. This principle can be used to cool the energy stored in all degrees of freedom while acting on a single mode only, like in the case of the resistive cooling of the axial motion which is envisaged at HITRAP.

## 3.2 Collective properties

If a test charge is introduced in a cloud of charges of opposite sign, its electric potential is screened beyond a certain distance. The potential decays according the law $\exp\{-r/\lambda_D\}/r$. The characteristic decay distance $\lambda_D$ is called *Debye length*, defined as

$$\lambda_D = \left(\frac{\varepsilon_o k_B T}{nq^2}\right)^{1/2}, \tag{3.6}$$

where $T$, $n$, $q$ are the temperature, density and charge of the cloud, $k_B$ the Boltzmann constant and $\varepsilon_o$ the dielectric constant. When the size of the cloud is larger than $\lambda_D$, individual particles cannot be distinguished beyond this characteristic distance and the collective properties of the cloud become relevant. The ionized gas is then called a *plasma*.

A plasma can be confined in a Penning trap and its relaxation to thermodynamical equilibrium leads to a state influenced by $q$, $n$ and $T$. It has been shown that a plasma at equilibrium in a quadrupole electrostatic potential takes the shape of an ellipsoid rigidly rotating along the longitudinal axis ( rigid rotor equilibrium) [Dub99]. Assuming a constant plasma density $n(r) = n$ we can write the radial force balance

$$-\frac{mv_\theta^2}{r} = qE_r + qv_\theta B, \tag{3.7}$$

where $v_\theta$ is the rotation tangential velocity. With the known cyclotron frequency $\omega_c$ and introducing the plasma frequency

$$\omega_p = \left(\frac{q^2 n}{2\varepsilon_o m}\right) \tag{3.8}$$

as well as the angular velocity $\omega = v_\theta/r$, Eq. (3.7) becomes

$$-\omega^2 = \frac{1}{2}\omega_p^2 + \omega\omega_c. \tag{3.9}$$

The solution reads

$$\omega = \frac{\omega_c}{2}\left[1 \pm \left(1 - \frac{2\omega_p^2}{\omega_c^2}\right)^{1/2}\right] \tag{3.10}$$

i.e. there are two real rotation frequencies only if

$$2\omega_p^2 \leq \omega_c^2 \Leftrightarrow n \leq n_B \doteq \frac{\varepsilon_o B^2}{2m}. \tag{3.11}$$

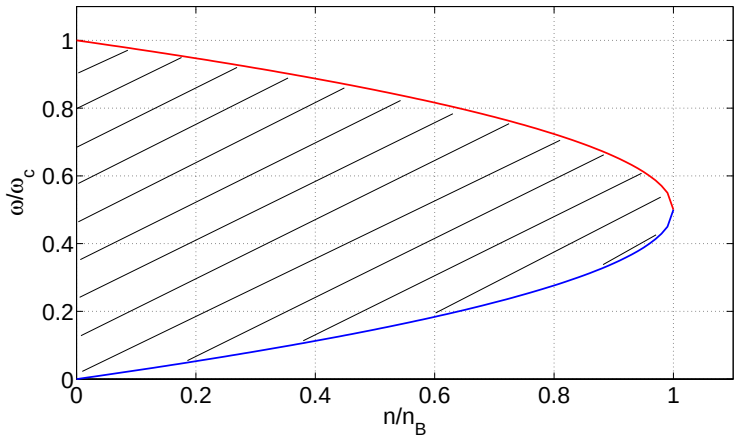


Figure 3.3: Plasma confinement below the Brillouin limit. The hatched area represents the region where radial confinement is attained.

This means that there is a constraint on the density of particles beyond which the radial confinement is lost. The cloud expands until the density is reduced enough to equilibrate electrostatic repulsion with the magnetic and centrifugal forces. This upper density value is called *Brillouin limit* $n_B$. The confinement region is depicted in Fig. 3.3.

The confinement of charged particles is also subject to another limit: the effective potential in the trapping region is given by the sum of the potentials given by the trap electrodes and the charge distribution itself (*self-field* or *space charge*). Increasing the number of ions, space charge will progressively fill the potential well along the longitudinal axis until the potential flattening will reach the endcap voltage and no other ions can be trapped anymore. This means that there is a limitation on the total number of charges that can be trapped. With the assumption of a cylindrical column of radius $\rho_c$ and uniform density, the maximum number of confined particles $N$ of charge $q$ reads [Mit95]

$$N = \frac{4\pi\varepsilon_o L V_d}{q}\left(1 + 2\ln\frac{r_w}{\rho_c}\right)^{-1} \tag{3.12}$$

where $L$ is the length of the trap (cap-to-cap distance), $r_w$ its radius and $V_d \approx 0.7 V_{endcap}$ the potential well depth. Thus $N$ depends linearly on $V_{endcap}$. Later in this chapter, in the discussion on the code benchmarking (see Sec. 3.5), we will verify the confinement conditions in the Cooler Trap.

Very important collective features of a plasma are *electrostatic plasma modes*, i.e. collective motions of the charged particle cloud. They have been investigated both theoretically [Dub91] and experimentally [Hei91] and are well understood and characterized. Their importance lies in the fact that since their frequencies depend on density and shape of the plasma, their detection can be exploited for nondestructive diagnostics [Amo03]. Furthermore, energy

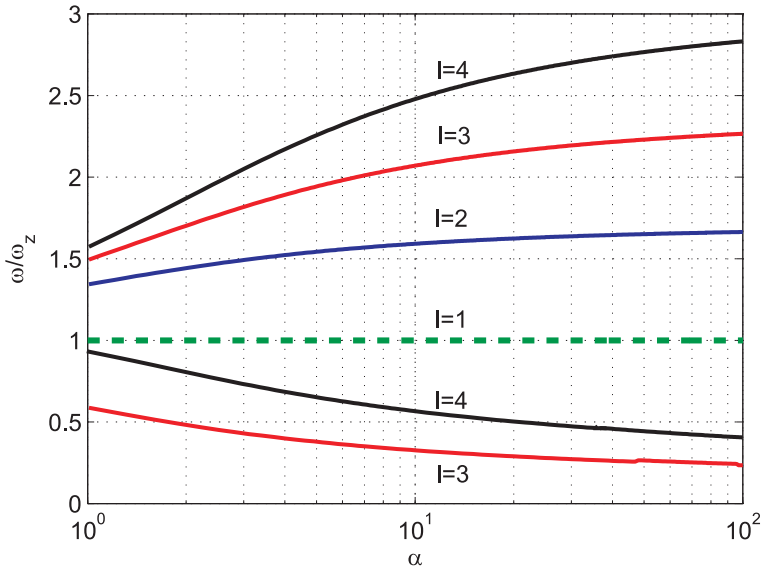


Figure 3.4: Low-order plasma modes according to the cold fluid theory. Frequencies are plotted as a function of the aspect ratio $\alpha = L/2\rho_c$ of the plasma ellipsoid (with $L$ and $\rho_c$ length and radius of the ellipsoid, respectively). The first azimuthally-symmetric modes are shown only for $\alpha \geq 1$. $l = 1$ is the center-of-mass motion, with frequency $\omega_z$. There are multiple possible branches for modes with $l > 2$.

is stored in those modes and their understanding and monitoring cannot be neglected in the resistive cooling. The plasma modes are indicated by two integer numbers $l$ and $m$, with $l > 0$ and $|m| \leq l$. $m \neq 0$ modes introduce azimuthal deformations breaking the radial symmetry. Examples of low-order modes are the center-of-mass motion, i.e. the $(1, 0)$ mode (whose frequency is equal to the single-particle axial oscillation $\omega_z$ if the space charge is negligible), or the $(2, 0)$ mode, a breathing-like deformation where the cloud periodically stretches in the axial direction and squeezes in the radial one, and vice versa. For $(1, 1)$ the cloud center does not lie on the longitudinal axis and rotates around it. The frequencies of the plasma modes can be calculated within the cold fluid theory [Dub91], which assumes a cold plasma of uniform density in a quadratic potential. Under these assumptions, the frequency $\omega$ of any low-order, $m = 0$ mode is extracted by the so-called dispersion relation

$$1 - \frac{\omega_p^2}{\omega^2} = \frac{k_2}{k_1} \frac{P_l(k_1)\, Q_l'(k_2)}{P_l'(k_1)\, Q_l(k_2)}, \tag{3.13}$$

where $k_1 = \alpha \left(\alpha^2 - 1 + \omega_p^2/\omega^2\right)^{-1/2}$, $k_2 = \alpha \left(\alpha^2 - 1\right)^{-1/2}$ and $\alpha = L/2\rho_c$ aspect ratio of the plasma ellipsoid. Figure 3.4 shows the trend of the first $m = 0$ modes ss a function of $\alpha$. Frequencies will be altered by the deviations from the cold fluid theory, namely the temperature and density of the plasma. We

will come back to plasma modes when discussing resistive cooling in Chapter 4.

## 3.3 Electromagnetic characterization

Given the general features and limitations of a Penning trap, the actual design of the Cooler Trap has been developed upon the most compelling constraints, i.e. efficient injection and storage of the ion bunch together with electrons and successive possibilities of manipulation.

A small-size hyperboloidal trap is not suitable for injection of a 1.2-$\mu$s, 6-keV/u beam, as the incoming bunch, stopped by the farther endcap by a potential about $15 \div 18$ kV (considering $U^{92+}$, with a $m/q = 2.6$, the beam energy is 15.6 keV/q), would bounce back and exit before the other endcap potential is raised. An elongated cylindrical trap is therefore necessary (as already envisaged in the Technical Design Report of the HITRAP facility [TDR03], the first official document to present the technical guidelines of the complete project). It can be shown that the accurate harmonicity of hyperboloidal traps can be achieved in the central region of a cylindrical trap with a proper electrode geometry [Bro86]. Calculations have shown that keeping the base voltage of the electrode stack at $\approx$ 11 kV, the beam is decelerated to 2 keV/u and a trapping length of 400 mm yields a time $\tau_{out} = 400$ ns to raise the first endcap voltage [Her06a]. Fast switches able to perform operation are available (see Sec. 5.3).

A cylindrical trap is also useful for its extended trapping volume. With a magnetic field of 6 T, chosen as a compromise between radial confinement capabilities and cost, the Brillouin limit for $U^{92+}$ and electrons is, respectively, $4 \cdot 10^8$ cm$^{-3}$ and $1.75 \cdot 10^{14}$ cm$^{-3}$. For simultaneous confinement of two species the lower limit must be considered. Experimentally, the Brillouin density is not always reached (without the rotating wall compression, which implies heating of the cloud). With the conservative assumption of a maximum density of $0.2 \cdot n_B$, confinement of $10^5$ bare uranium ions requires a volume of 1.25 mm$^3$, while $10^{10}$ electrons demand 125 cm$^3$. The latter value is the volume of a cylinder with a length of 400 mm and a radius of 10 mm. A larger radius is desirable to reduce losses by impact on the walls. On the other hand, the magnet surrounding the trap limits the diameter of the cold bore to 150 mm, and the cryogenic electronics must be lodged inside that environment, too. The compromise is an electrode inner radius of 17.5 mm. This guarantees a sufficient storage space, even when electrons (the actual critical species in terms of accumulation) will be swept out and the cooled ions will be collected in a smaller, central region.

The last fundamental feature of the Cooler Trap is its rather complex internal structure, including volumes conceived for separate storage of ions and electrons, i.e. nested traps. The so-called *nested-trap* configuration refers to the possibility of shaping the axial potential profile in order to have hills and

wells where, respectively, electrons and ions can be confined [Gab99]. These inner traps should be fairly harmonic, as a potential with such a shape grants several advantages; we have already mentioned in Sec. 3.1 the control possibilities on the particles' eigenmotions, whose values are in this case well defined. But this is advantageous even for the pure storage convenience: experiments as well as theory [Moh02] have demonstrated that more efficient trapping can be achieved compared to classical flat-bottomed Penning-Malmberg traps used in the plasma community, where the length of the cylindrical column of ions influences the storage lifetime ([Dri83], [Faj99]).

Nested traps are instrumental in the operation of the Cooler Trap tasks. Since the first cooling part is performed via Coulomb collisions with synchrotron-radiation-cooled electrons, these are pre-loaded and get confined under the nested potential hills. Subsequently injected hot ions cross the electron regions and lose energy, falling into the nested wells. Electrons are then swept out by fast switching of the electrode voltages (thanks to the large $m/q$ difference between electrons and HCI, the latter are not affected by the fast operation). Ions are collected in the center and resistively cooled. If we want to have a central nested well for HCI from the beginning, which is desirable in order to have full detection of the dynamics during the whole stay in the Cooler Trap, the minimum number of nested traps is five, as Fig. 3.5 depicts: three for the ions and two for the electrons. For the sake of maximum simplification and flexibility, we decided to have for all of them equal geometrical features, which are described and further motivated in the next Subsection.

Summarizing, the basic concepts of the Cooler Trap are the following:

- cylindrical geometry with a *nested-trap* configuration;
- axial trapping length of approximately 400 mm;
- inner radius of 17.5 mm;
- magnetic field of 6 T.

### 3.3.1 Orthogonal vs Multi-Ring traps

Following the concept of the high-accuracy Penning traps used in atomic physics, the initial TDR design [TDR03] included for each nested trap a special electrode configuration that provides a high degree of harmonicity at a definite position, a frequent request in precision spectroscopy: the *orthogonalized anharmonicity compensation* [Gab84, Bro86]. As the purpose of the Cooler Trap is rather different (storage of high numbers of particles, not single-ion precision measurements), we investigated the opportunity of such an arrangement.

The request for harmonicity means that the desired potential should have in the center the quadrupole form $V \propto z^2 - r^2$. Keeping in mind the azimuthal

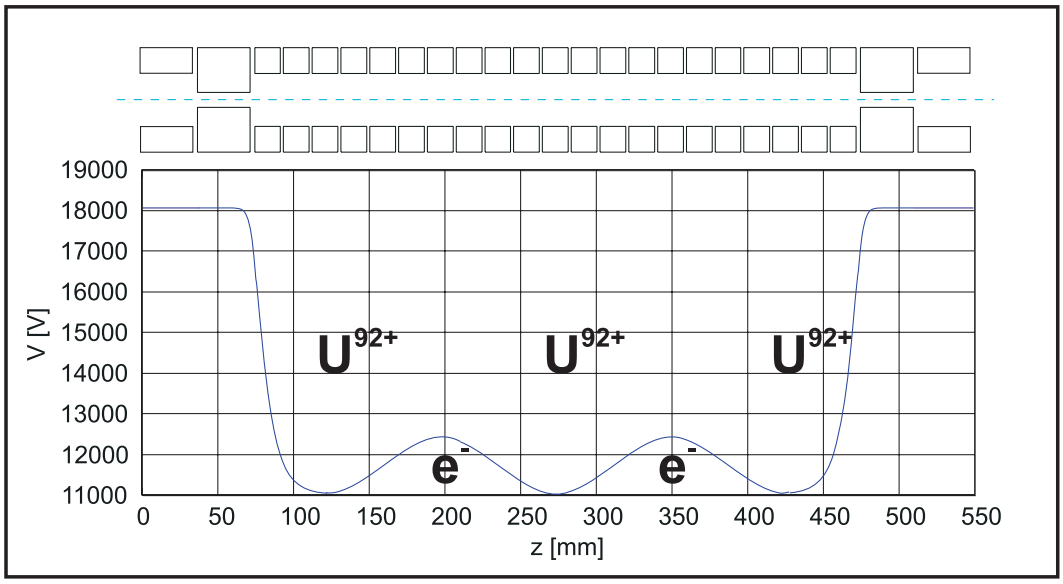


Figure 3.5: Potential of a nested-trap configuration. The voltages applied to the electrodes of the Cooler Trap (sketched in the upper part) can be shaped in such a way that simultaneous storage of positive and negative charges is possible in adjacent potential hills and well.

symmetry of Penning traps, an expansion of $V$ in Legendre polynomials yields

$$V = \frac{1}{2} V_o \sum_{k_{even}=0}^{\infty} C_k \left(\frac{r}{d_o}\right)^k P_k\left(\cos\theta\right), \tag{3.14}$$

where $V_o$ is the trapping potential and $d_o^2 = \frac{1}{2}\left(z_o^2 + \frac{1}{2} r_o^2\right)$ is a geometrical factor depending on the trap's radius $\rho_o$ and distance from center to endcap $z_o$. The request of harmonicity implies $C_k = 0\ \forall k > 2$. Obviously a reasonable compromise is asking for $C_4 = 0$, being it the first non-harmonic contribution.

In a cylindrical trap, the introduction of two correction electrodes aside of the central ring (see Fig. 3.6) helps in extending the harmonic region, but alters the $C_k$ coefficients: $V$ can be in fact written as a superposition of $\Phi_o$ (endcap voltage) and $\Phi_c$ (correction voltage)

$$V = V_o \Phi_o + V_c \Phi_c, \tag{3.15}$$

where

$$\Phi_o = \frac{1}{2} \sum_{k_{even}=0}^{\infty} C_k^{(0)} \left(\frac{r}{d_o}\right)^k P_k\left(\cos\theta\right), \tag{3.16}$$

$$\Phi_c = \frac{1}{2} \sum_{k_{even}=0}^{\infty} D_k \left(\frac{r}{d_o}\right)^k P_k\left(\cos\theta\right). \tag{3.17}$$

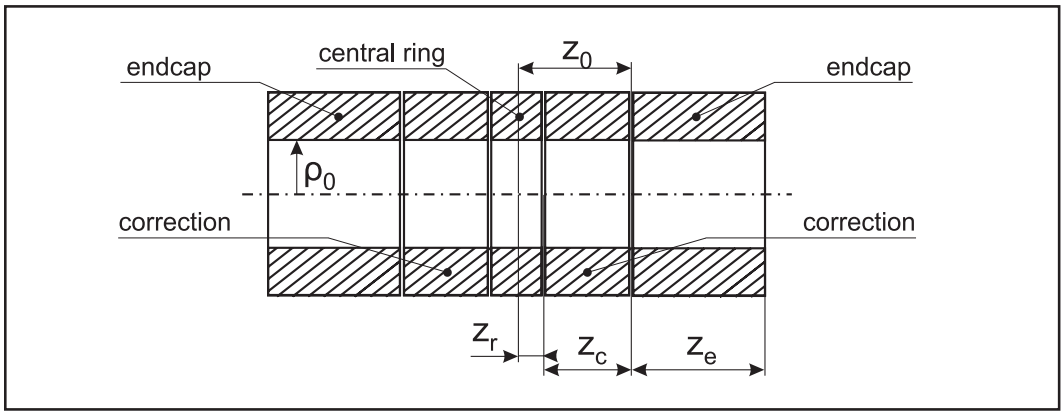


Figure 3.6: Compensated cylindrical Penning trap of radius $\rho_o$. The potential well is defined by the voltages applied on the endcaps of length $z_e$ and the central ring of length $2z_r$. The voltage of the correction electrodes (length $z_c$) is potimize to improve the harmonicity of the potentials. The trapping region is $2z_o$.

The $C_k^{(0)}$, $D_k$ coefficients can be determined by comparison with the expansion in Bessel functions:

$$V = V_o \sum_{n=0}^{\infty} A_n J_o\left(ik_n\rho\right)\cos\left(k_n z\right), \tag{3.18}$$

where

$$k_n = \frac{\left(n+1/2\right)\pi}{z_o + z_e} \tag{3.19}$$

and $z_e$ is the endcap length[1]. Evaluation of Eq. (3.14) and (3.18) on the z-axis yields

$$C_k^{(0)} = \frac{(-1)^{\frac{k}{2}}}{k!}\frac{\pi^{k-1}}{2^{k-3}}\left(\frac{d_o}{z_0+z_e}\right)^k \sum_{n=0}^{\infty}(2n+1)^{k-1}\frac{A_n^{(c)}}{J_0\left(ik_n\rho_0\right)}, \tag{3.20}$$

$$D_k = \frac{(-1)^{\frac{k}{2}}}{k!}\frac{\pi^{k-1}}{2^{k-3}}\left(\frac{d_o}{z_0+z_e}\right)^k \sum_{n=0}^{\infty}(2n+1)^{k-1}\frac{A_n^{(d)}}{J_0\left(ik_n\rho_0\right)}, \tag{3.21}$$

with

$$A_n^{(c)} = \frac{1}{2}\left\{(-1)^n - \sin\left(k_n z_0\right) - \sin\left[k_n\left(z_0 - z_c\right)\right]\right\}, \tag{3.22}$$

$$A_n^{(d)} = \sin\left(k_n z_0\right) - \sin\left[k_n\left(z_0 - z_c\right)\right]. \tag{3.23}$$

[1]The arguments of this paragraph, originally developed for closed traps or infinitely long endcaps, still substantially hold for large $z_e$ ($z_e/\rho_o > 3.$). The theory of orthogonalized traps as we summarized here is drawn from [Gab89]

Table 3.1: Geometry of a 95-mm long orthogonal trap. The real values take into accounts spacings between electrodes (2 mm).

| | Exact value [mm] | Real value [mm] |
|---|---|---|
| $z_o$ | 17.0915 | 17.09 |
| $z_c$ | 14.2731 | 12.27 |
| $z_{ring}$ | 2.8184 | 1.82 |
| $z_e$ | 30.4085 | 29.41 |

This has two effects: since now $C_k = C_k^{(0)} + D_k \frac{V_c}{V_o}$, $C_4$ can be made zero by a proper choice of the correction potential

$$\frac{V_c}{V_o} = -\frac{C_4^{(0)}}{D_4}; \tag{3.24}$$

the disadvantage is that $C_2$ is affected by the correction voltage, and so is the axial frequency

$$\omega_z = \sqrt{\frac{qV_o}{md_o^2} C_2}. \tag{3.25}$$

This undesired effect can be avoided by *orthogonalizing* the trap, i.e. making $D_2 = 0$; this is always possible with a proper selection of $\rho/z_0$ and $z_c/z_o$. Moreover, it can be shown that with $z_c/z_o = 0.835$, also $C_6$ goes to zero.

With the abovementioned assumptions, the geometry of an orthogonalized cell of length $\sim 95$ mm (i.e. $\sim 1/5$ of the total length) in the Cooler Trap is easily determined, as summarized in Table 3.1, where real spacings between electrodes and a machining accuracy of 10 $\mu$m are included.

We would like to recall the attention of the reader on some key features of the orthogonal trap. As visible from Fig. 3.6 and 3.7, the large extension of the endcaps strongly restricts the useful longitudinal trapping length: the useful region has a length $2z_o$. Second, the arrangement of electrodes of different axial dimension yields the highest harmonicity when the potential and geometrical centers coincide. These properties results in excellent control of a single trapped particle, but become a disadvantage for the storage of a large bunch of ions: the trapping volume is reduced and if the potential center is moved to another axial position, the harmonicity is severely degraded. In other words, there is a price to pay in terms of flexibility, while the effort in reaching this nominal high accuracy might also become useless since it is anyway limited by the considerable space charge of the ion cloud. In order to evaluate quantitatively the trade-off between the advantages and disadvantages, we compare the orthogonal trap with a different arrangement, the *Multi-Ring Trap (MRT)*.

The basic concept of the MRT is to use the same geometry for all electrodes. In a configuration with an arbitrary number of equal electrodes, the main and most evident advantage is the possibility of shaping the electrostatic

potential with the same accuracy at virtually any internal position, although the maximum harmonicity might be worse than that of an orthogonal trap. As a matter of fact, Fei [Fei99] has shown that MRTs can be orthogonalized too, using more sets of correction rings and choosing an optimized electrode geometry. However, since we want to minimize the number of electrodes while keeping the concept of five harmonic compensated regions rather than reaching the maximum accuracy, we draw our geometry from simpler arguments: using a single ring as endcap for two adjacent nested traps we obtain 21 electrodes with a length of 17 mm and 2-mm spacings. An MRT arrangement has already been successfully used in other storage trap facilities, like the antiproton MUSASHI-ASACUSA setup ([Ich01], [Kur05]) at CERN.

The correct potential of any real electrode stack can be evaluated either numerically with any solver, like SIMION [SIM95], or with the analytical formula[2] [Ver01]

$$\Phi(r,z) = \sum_{n=1}^{\infty}\left\{\left[\frac{\Phi_1\cos(k_n z_o)-\Phi_N\cos(k_n z_{2N-1})}{k_n} + \right.\right. \tag{3.26}$$

$$\left.+\sum_{i=1}^{N-1}\left(\frac{\Phi_{i+1}-\Phi_i}{z_{2i}-z_{2i-1}}\cdot\frac{\sin(k_n z_{2i})-\sin(k_n z_{2i-1})}{k_n^2}\right)\right]\cdot \tag{3.27}$$

$$\left.\cdot\ \frac{I_o(k_n r)}{I_o(k_n\rho_o)\frac{L}{2}}\sin(k_n z)\right\}, \tag{3.28}$$

where $k_n=\frac{n\pi}{L}$, $\rho_o$ and $L$ are radius and length, $N=5$ the number of electrodes. The fourth-order anharmonicity can be once again eliminated by a proper $V_c$ tuning, which we can calculate as follows. Observing that the coefficient of $z^4$ is proportional to the fourth partial derivative in z, and rearranging Eq. (3.26) as a function of the electrode voltages $\Phi_i$, the request for harmonicity reads

$$\left.\frac{\partial^4 V}{\partial z^4}\right|_{z=0} = \sum_{n=1}^{5}\gamma_i\Phi_i = 0; \tag{3.29}$$

by symmetry $\Phi_1=\Phi_5=\Phi_e$, $\Phi_2=\Phi_4=\Phi_c$, $\Phi_3=\Phi_r$, therefore

$$\Phi_c = -\frac{\gamma_r\Phi_r+2\gamma_e\Phi_e}{2\gamma_c}. \tag{3.30}$$

To compare the properties of the orthogonal and the MRT arrangements, one can then fit their potential (obtained via Eq. (3.26)) on the z-axis to an n-degree polynomial of the type

$$V=\sum_{i=0}^{n}B_i z^i=\sum_{i=0}^{n}\frac{C_i'}{d_o^i}z^i, \tag{3.31}$$

[2]This expression implies only the restriction to constant inner radius.

Table 3.2: Expansion coefficients of the on-axis potential in an orthogonal and Multi-Ring trap. In the first two columns, $V$ is fitted to an 8th-degree polynomial on a length of $2 \cdot z_{o,ortho} = 2 \cdot 17.09$ mm. The third column shows a fit for the MRT on a length of $2 \cdot z_{o,MRT} = 2 \cdot 29.50$ mm.

| | Orthogonal | MRT | MRT (extended) |
|---|---|---|---|
| $C_2'$ | $2.718 \cdot 10^{-1}$ | $2.599 \cdot 10^{-1}$ | $2.570 \cdot 10^{-1}$ |
| $C_4'$ | $5.506 \cdot 10^{-3}$ | $-8.267 \cdot 10^{-3}$ | $-4.313 \cdot 10^{-4}$ |
| $C_6'$ | $-1.547 \cdot 10^{-2}$ | $5.328 \cdot 10^{-2}$ | $5.465 \cdot 10^{-2}$ |
| $C_8'$ | $1.056 \cdot 10^{-3}$ | $-1.180 \cdot 10^{-2}$ | $-2.238 \cdot 10^{-2}$ |

and look at the $C_i'$ coefficients. These are presented in Table 3.2 and show that indeed the MRT higher-order coefficients (especially $C_6$ and $C_8$) are generally worse, but not too severely. As a matter of fact, the coefficients for the orthogonal trap are not as good as one would expect since the high-accuracy region is rather limited, while the larger endcap-to-endcap distance in the MRT favours a fairly good harmonic approximation over an extended length. The third column shows indeed that, extending the fitting region to include the correction electrodes, the expansion coefficients do not get worse. As a confirmation, the accuracy index

$$B_{sum} = \frac{\sum_{i=3}^{n} B_i z^i}{B_2 z^2}, \tag{3.32}$$

which intuitively estimates the relative overall contribution of the high-order terms with respect to the pure parabolic potential, is also comparable in the two configurations (see Fig. 3.7).

To summarize, we have shown that the major advantage of the orthogonal trap, i.e. the axial-frequency independence on the correction-electrode potential, can be sensibly affected by the fact that in our case we have relatively short endcaps with adjacent traps, which can reciprocally distort the respective harmonicities. Voltage tuning will therefore be necessary anyway, especially due to the massive space charge (see Sec. 3.5 and 4.3.4). On the contrary, the axially-elongated storage capacity and the flexibility in field shaping of the MRT are of great advantage to our needs. Therefore the MRT configuration proves to be the most effective choice for the Cooler Trap, and is the finally chosen design. 21 inner electrodes with radius 17.5 mm, length 17 mm and spacings of 2 mm are used to shape the nested traps. Endcaps have a length of 34.75 mm and a radius of 5 mm, with the double purpose of reinforcing the trapping potential and providing a differential pumping barrier. Two additional external electrodes are added to stabilize the field outside the trapping region (see Chapter 5).

A final remark on the effects of construction imperfections is mandatory. Every real setup is affected by machining and alignment defects, the influence of which is sometimes sensible and degrading in terms of physics, too.

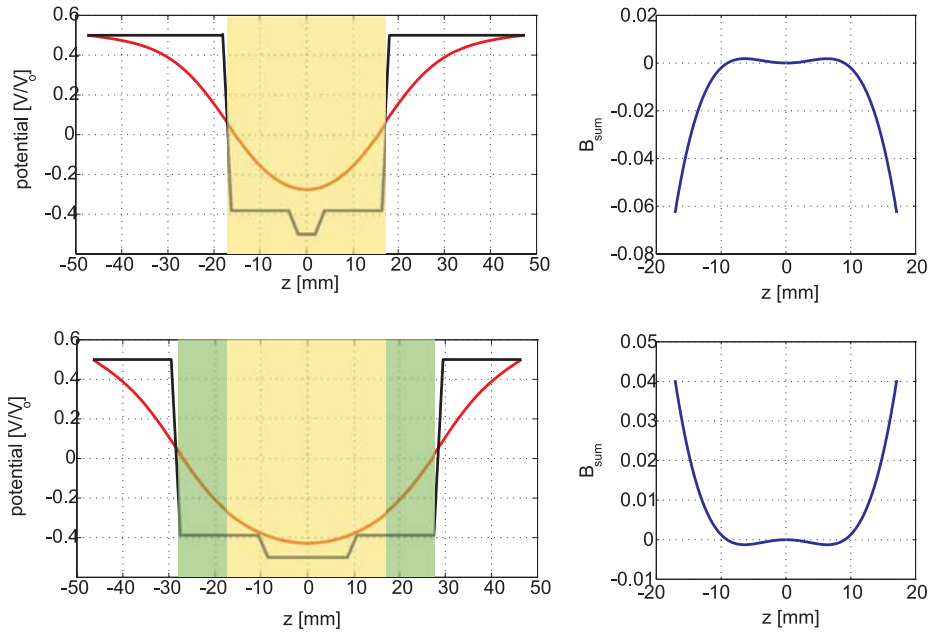


Figure 3.7: Comparison between orthogonal (top left) and Multi-Ring (bottom left) trap. In red, the potential along the z-axis, in black the electrode voltages. On the right side, the $B_{sum}$ accuracy index in the central region highlighted in yellow on the left. Notice the axially-extended trapping region of the MRT (highlighted in green).

Therefore an analysis on the electric potential distortions was performed. The central nested trap was considered, assuming a 'worst case' where the central ring was tilted and the two adjacent correction electrodes were misaligned with respect to the longitudinal axis. With an interelectrode spacing of 2 mm, the maximum rotation before contact between adjacent elements is 4.5°. The electrode shifts were forced up to 1 mm, much above the mechanical tolerances (reasons for the technical details on the electrode design are discussed in Chapter 5). The calculations show that the parameters of interest described above ($C_k$ coefficients, $B_{sum}$ index) have a deviation within 50% of the values obtained for the ideal case, up to a distance of 5 mm from the longitudinal axis. The conclusion is that the distortions are practically negligible. The reason is mainly the large inner radius of the Cooler Trap, which smoothens the effect in the center of the imperfections at the radial boundary.

## 3.4 The choice of a Particle-In-Cell (PIC) code

The study of the electrostatic field properties of a given trap geometry is a task where SIMION proves to be an excellent tool. Nevertheless SIMION is based on the solution of the Laplace equation. Hence its apparent limitation

is the space charge arising from the presence of a large number of ions, which will repel each other deforming the actual $\vec{E}$ field. The program allows one to estimate the charge repulsion [SIM95] that suit better the case of beam lines rather than a trap where particles, in their periodic motion, experience repeatedly a relatively small volume for a long time. To treat thoroughly and self-consistently the space charge problem, the Coulomb repulsion between ions can be calculated following two different approaches, that are (1) evaluating each particle-particle interaction or (2) solving the Poisson equation.

Full *Molecular Dynamics* (MD) codes follow the first idea. This means that, in an ensemble of $N$ particles, the trajectory of each ion is subject not only to the external electromagnetic forces (the trap potential configuration and magnetic field), but also to the Coulomb interaction with its $N-1$ companions:

$$\vec{F_i} = q_i E + q\vec{v_i} \times \vec{B} + \sum_{j=1, j\neq i}^{N} \frac{1}{4\pi\varepsilon_o} \frac{q_i q_j}{(r_i - r_j)^2} \frac{\vec{r_i} - \vec{r_j}}{|\vec{r_i} - \vec{r_j}|}. \tag{3.33}$$

The accuracy of this method has the drawback that the number of interparticle forces to evaluate, and subsequently the computation time, will scale with $N^2$. Optimizing with the implementation of the Barnes-Hut algorithm [Bar86], one can reach an $O(N \log N)$ dependence. The computational effort requires code parallelization and availability of machine clusters, and yet the number of particles that can be simulated cannot exceed a few thousand. To consider larger ensembles of ions, *superparticles* and *force scaling* are introduced [Bec01]. Instead of simulating all of the $N$ bodies, only $N_{sim}$ superparticles, with $N_{sim} \ll N$, are computed, giving therefore a scaling

$$n_{sc} = \frac{N}{N_{sim}}. \tag{3.34}$$

To get the result for $N$ particles, the real Coulomb interaction $F_c$ must be scaled accordingly and the force $F_{c,sim}$ used in the simulation reads then

$$F_{c,sim} = n_{sc} \cdot F_c. \tag{3.35}$$

The scaling factor must be handled with care: large values increase the difference between the Coulomb field of a superparticle and the more smeared effect of a real cloud of ions. The effect is fairly negligible as far as $n_{sc}$ is about $10 \div 100$ [Stu08].

The so-called *mean-field approach* is radically different from a full MD code, as no direct particle-particle interaction is considered, but the charge distribution of the ions is inserted in the Poisson equation

$$\nabla^2 \Phi = -\frac{\rho}{\varepsilon_o}. \tag{3.36}$$

In a separate operation, the ions are moved solving the Newton equations, where the electrostatic force is given by the solution of Eq. (3.36), that will

then include, in addition to the external electrostatic field, the space-charge effect as a mean field (hence the name). As practically one distributes the charge on a spatial grid and the Poisson equation is evaluated on its nodes, this method is also called *Particle-In-Cell (PIC)* or *Particle-Mesh (PM)*. The clear advantage is the linear dependence of the simulation time on the number of particles. Scaling with superparticles is used here, too, to further reduce the computational effort. This results in a code that can be easily handled by single PC units. The disadvantage is in the loss of the direct interaction, that forces to neglect the hard-core repulsion of real particles: the superparticles can be imagined as finite-size rigid clouds that may pass through each other (*cloud-in-cell* or *CIC*) model [Bir69]. Nevertheless the drawback is mitigated by the fact that most or virtually all collisions are at large impact parameter and really close encounters are rare.

The promising computational advantages, together with the availability to our group of an existing code which we could modify and adapt to our purposes, motivated us to embrace the PIC approach. The details of the program will be explained in the following Subsections.

### 3.4.1 Structure of the PIC code

The core of the code we have used for our investigations was already existing, as it had been conceived by Dr. Stefan Schwarz who exploited it in simulations for the LEBIT ion trap at the National Superconducting Cyclotron Laboratory (NSCL), Michigan State University [Rin06, Sch05]. We have kept its fundamental architecture, that follows the standard PIC approach as described by Birdsall [Bir69], [Bir91] and Hockney [Hoc88] and which we have just outlined above.

Figure 3.8 shows the main loop of the program:

- the zero-th step is the generation of superparticles, that can be skipped in the subsequent cycles;
- the charge carried by the superparticles is attributed to the grid points in which the simulation volume has been subdivided, with a weighting system accounting for the scaling factor $n_{sc}$ mentioned above, the mesh type (in our case, a two-dimensional, $rz$-symmetric geometry) and the choice of charge apportionment on mesh nodes;
- the Poisson equation is solved on the spatial grid via a Fast-Fourier-Transform (FFT) routine;
- the mean field is calculated at each particle position from $\Phi$ given by the Poisson equation, and together with $\vec{B}$ is fed into the particle advancement algorithm. The ion position, velocity and acceleration are updated (and can be recorded), so that the loop restarts with a new charge distribution evaluation.

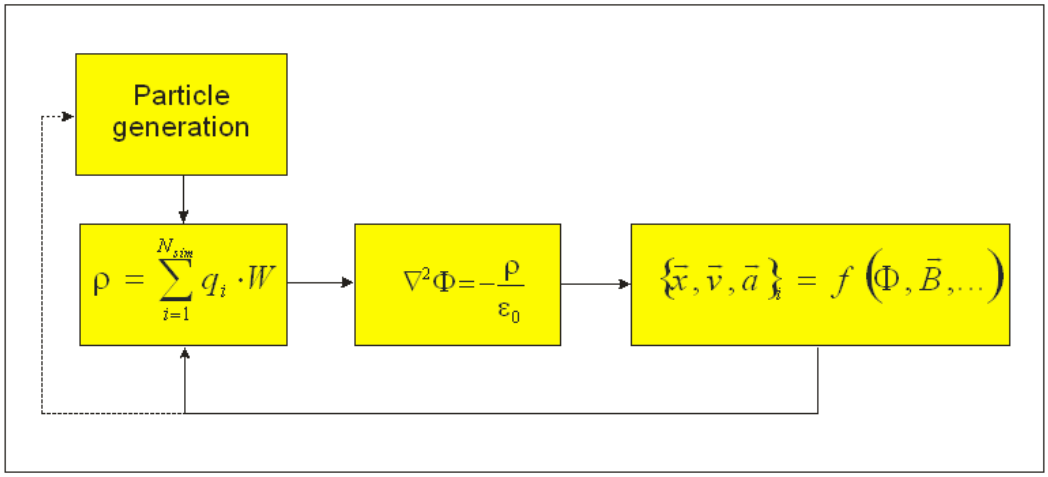


Figure 3.8: Scheme of the PIC code. The particle charge $\rho$ is weighted according to the scaling factor $W$ and included in the evaluation of the Poisson equation, which determines the total electrostatic potential $\Phi$. The new position, velocity and acceleration $\{\vec{x}, \vec{v}, \vec{a}\}$ of each particle are determined by the electromagnetic force. The charge distribution is updated, the loop restarts and incidentally new particles can be generated.

The *FFT* or *direct* method applied to the Poisson equation is a powerful tool to gain in computational speed when compared to conventional iterative methods (e.g. *Successive Over-Relaxation, SOR*, used for instance by SIMION). It consists in a Fourier analysis along one of the spatial dimensions of the potential and charge distribution. The solution of the resulting system of equations is sped up by a *recursive cyclic reduction* of the number of equations, made possible by the formal similarity of those as a consequence of symmetries [Hoc65]. The method is applicable to *xy* as well as to *rz* geometries, with proper modifications, that makes it suitable to our case.

The boundary conditions allowed by this technique are rather limited, e.g. only a rectangular-shaped grid is permitted. To include more complex structures with internal electrodes, the *capacity matrix* method is actually implemented. The potential is calculated first without taking into account the internal electrode points, then the deviation from the desired values gives the charge induced on the electrodes and the Poisson equation is calculated again. Therefore, the price to pay is solving the potential for each internal electrode point [Hoc88]. However since our simulations concern generally the inner trap electrodes, whose diameter is constant, we were not affected by this problem.

As mentioned above, the ion charges must be included in the Poisson equation via attribution to the grid points. Accurate weighting of the charge deposited by a particle on nodes has an influence on the good reproduction of the real physics. The simplest attribution to the closest node (*nearest-grid-point, NGP* or *zero-order* method) is rather rough and the resulting potential will

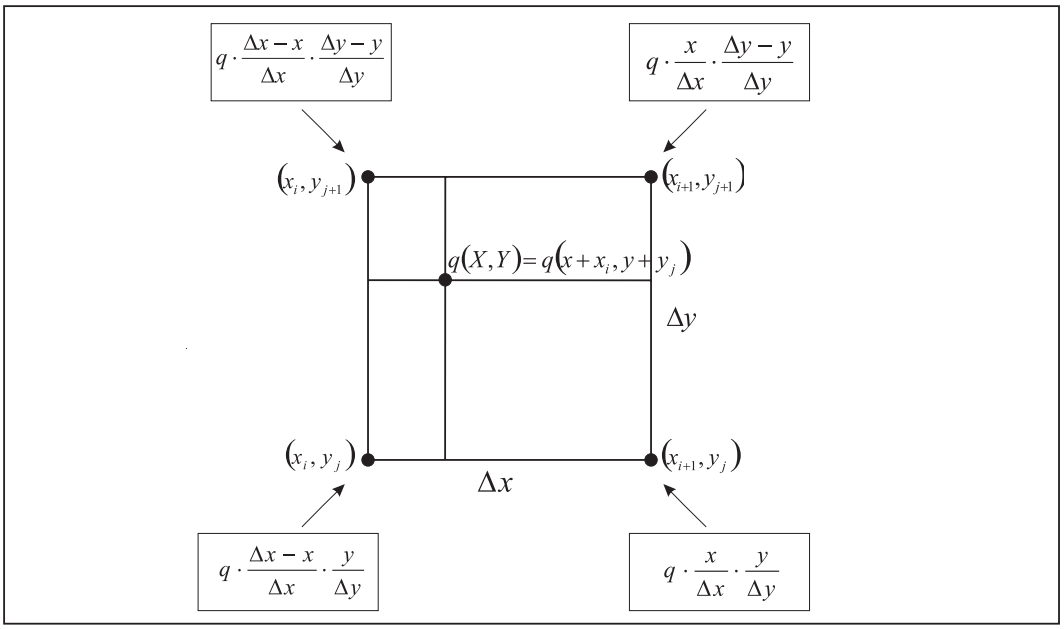


Figure 3.9: First-order weighting of a charge in an *xy* geometry. Notice that in a 3D Cartesian volume, $q$ has actually the dimensions of a linear charge density. The procedure is easily applied to an *rz* symmetry, just keeping in mind that the mesh cell volume depends on the radial coordinate.

have non-smooth fluctuations. It is a more common practice to interpolate between the two (in 1d) or four (2d) nearest grid points (see Fig. 3.9), therefore smearing the effect of the charged particle, that can now be seen as a finite-size cloud contained in the volume of a cell; this smoothens the solution (*cloud-in-cell, CIC* or *first-order* method). Higher-order weighting procedures could also be used, but at the expense of a higher computational cost. Self-consistency requires in every case that the same weighting scheme is used when the field is evaluated at the particle position during the time advancement step.

Notice that charge distribution on an *rz* grid implies smearing of a point particle on a ring of charge, so that the potential will have a cylindrical symmetry and no azimuthal irregularity can be seen. However the separation of mean-field evaluation and particle advancement allows a complete 3D treatment of the ions' trajectories, which we will deal with in the following.

### 3.4.2 Particle advancement algorithms

At a first thought, the numerical solution of Newton's equations of motion

$$\frac{\mathrm{d}\vec{r}}{\mathrm{d}t} = \vec{v} \tag{3.37}$$

$$\frac{\mathrm{d}\vec{v}}{\mathrm{d}t} = \vec{a} = \frac{\vec{F}}{m} \tag{3.38}$$

might seem a relatively straightforward task to be accomplished via the use of one of the many finite-difference routines. The specificity of the physical problem under consideration make it far less trivial that intuition may lead to think.

In the plasma physics community, the Runge-Kutta algorithms (second- and fourth-order versions mainly) [Abr70] and the so-called leapfrog algorithm [Hoc88], [Bir91] are among the most common and widely used due to their accuracy and robustness. The latter scheme is derived as follows: considering a time discretization $\Delta t$, one can write

$$\frac{\mathrm{d}\vec{r}}{\mathrm{d}t} \rightarrow \frac{\vec{r}\,(t+\Delta t)-\vec{r}\,(t)}{\Delta t}=\vec{v}\left(t+\frac{1}{2}\Delta t\right) \tag{3.39}$$

$$\frac{\mathrm{d}\vec{v}}{\mathrm{d}t} \rightarrow \frac{\vec{v}\left(t+\frac{1}{2}\Delta t\right)-\vec{v}\left(t-\frac{1}{2}\Delta t\right)}{\Delta t}=\vec{a}\,(t)\,, \tag{3.40}$$

that after rearranging yields the succession of operations

$$\vec{v}\left(t+\frac{1}{2}\Delta t\right) = \vec{v}\left(t-\frac{1}{2}\Delta t\right)+\vec{a}\,(t)\,\Delta t \tag{3.41}$$

$$\vec{r}\,(t+\Delta t) = \vec{r}\,(t)+\vec{v}\left(t+\frac{1}{2}\Delta t\right)\Delta t. \tag{3.42}$$

The difficulty in simulating the environment of a Penning trap is the presence of the magnetic field $\vec{B}$. The $\vec{v}\times\vec{B}$ term is a pure rotation of the velocity vector, whose absolute value is modified only by the electrostatic force; therefore the succession of steps to advance the velocity has to be taken into account. The original PIC code initially followed Boris' approach [Bor70] of

1. adding half of the electric impulse;
2. rotating the velocity vector;
3. adding the second half of the electric impulse.

In fact Eq. (3.38) can be discretized according to the time-centered scheme [Bun67]

$$\begin{aligned}\frac{\vec{v}\,(t+\Delta t/2)-\vec{v}\,(t-\Delta t/2)}{\Delta t} &= \frac{q}{m}\Big[\vec{E}+\\ &+ \frac{\vec{v}\,(t+\Delta t/2)+\vec{v}\,(t-\Delta t/2)}{2}\times\vec{B}\Big]\end{aligned} \tag{3.43}$$

If we define

$$\vec{v}\,(t-\Delta t/2) = \vec{v}^{-}-\frac{q\vec{E}}{m}\frac{\Delta t}{2} \tag{3.44}$$

$$\vec{v}\,(t+\Delta t/2) = \vec{v}^{+}+\frac{q\vec{E}}{m}\frac{\Delta t}{2}, \tag{3.45}$$

the rotation in the radial plane $xy$ is expressed by

$$\frac{\vec{v}^{+} - \vec{v}^{-}}{\Delta t} = \frac{q}{2m}\left(\vec{v}^{+} + \vec{v}^{-}\right) \times \vec{B} = \left(\vec{v}^{+} + \vec{v}^{-}\right) \times \frac{\vec{\omega}_c}{2}\widehat{e}_z \tag{3.46}$$

and the succession of operations becomes

$$\begin{aligned}
&1. && \vec{v}^{-} &&= \vec{v}\,(t - \Delta t/2) + \frac{q\vec{E}}{m}\frac{\Delta t}{2} && (3.47)\\
&2a. && v_x' &&= v_x^{-} + v_y^{-} t && (3.48)\\
&2b. && v_y^{+} &&= v_y^{-} + v_x' s && (3.49)\\
&2c. && v_x^{+} &&= v_x' + v_y^{+} t && (3.50)\\
&3. \quad \vec{v}\,(t + \Delta t/2) && &&= \vec{v}^{+} + \frac{q\vec{E}}{m}\frac{\Delta t}{2}. && (3.51)
\end{aligned}$$

The steps $2a. \div 2c.$ represent the radial rotation of angle $\theta$, approximated with $t = -\tan\theta/2 = \omega_c \Delta t/2$, $s = 2t/\left(1 + t^2\right)$. The approximation is good while $\theta$ is not too large.

This is the key point: since the cyclotron motion has the highest eigenfrequency, $\omega_c = qB/m$ can definitely be the limiting factor in the time discretization for high values of $B$. That is to say, a straightforward implementation would require

$$\Delta t \ll \frac{1}{\omega_c} = \frac{m}{qB}, \tag{3.52}$$

i.e. the strength of the magnetic field directly imposes a condition on the time step. Actually we may want to be free to relax this condition, since the phenomena we want to observe act on characteristic times that are much larger[3]. In other words, we are not interested in following the details of the cyclotron motion, that would have unaffordable computational cost; nor is time-adaptivity a solution, leading again simply to extremely small $\Delta t$. Notice that simulating highly charged ions, the high $q/m$ ratio increases the eigenfrequencies' values and makes the situation more critical. The leapfrog algorithm, even with the implementation of the $\vec{v} \times \vec{B}$ rotation described above, has hence an undesired limitation.

This problem has been solved with the implementation of a modified Velocity Verlet routine [Spr99] that is completely independent on the strength of the magnetic field[4]. In an ensemble of $N$ particle, the generic Velocity Verlet

[3] Our interest is focused on resistive cooling of the much slower axial motion, as described in detail in the next chapter

[4] A remark: this method has been used here within the Velocity Verlet scheme, but it can be adapted to other algorithms like the leapfrog or Runge-Kutta with similar results.

scheme [All89] for any of them reads (omitting the subscript)

$$\begin{aligned}
\vec{r}\,(t+\Delta t) &= \vec{r}\,(t)+\Delta t\vec{v}\,(t)+\frac{1}{2}\left(\Delta t^2\right)\vec{a}\,(t)+O\left((\Delta t)^3\right) && (3.53)\\
\vec{a}\,(t+\Delta t) &= \vec{a}\,(\vec{r}_{1,\ldots,N}\,(t+\Delta t)\,;\vec{v}_{1,\ldots,N}\,(t+\Delta t)\,;t+\Delta t) && (3.54)\\
\vec{v}\,(t+\Delta t) &= \vec{v}\,(t)+\frac{1}{2}\Delta t\left[\vec{a}\,(t)+\vec{a}\,(t+\Delta t)\right]+O\left((\Delta t)^3\right); && (3.55)
\end{aligned}$$

although implicit in the second equation, it becomes explicit if the acceleration does not depend on the velocity. But in our case the acceleration is a consequence of the Lorentz force in the electromagnetic field:

$$\vec{a}=\frac{q}{m}\left(\vec{E}+\vec{v}\times\vec{B}\right) \qquad (3.56)$$

i.e. it has an explicit dependence on $\vec{v}$. Yet it has been shown [Spr99] that with a Taylor expansion of the magnetic term and a homogeneous value of B, the Verlet algorithm can be rewritten in an explicit form. I will not delve into the mathematical details and straightforwardly give the final expressions. Considering as usual a purely axial magnetic field $\vec{B}=B\widehat{e}_z$, calling $\vec{a}^C$ the velocity-independent part of the acceleration, i.e. in our case the electrostatic term $q\vec{E}/m$, and with the definitions $S\left(\omega_c\Delta t\right)\equiv\sin\left(\omega_c\Delta t\right)-\omega_c\Delta t$, $C\left(\omega_c\Delta t\right)\equiv\cos\left(\omega_c\Delta t\right)-1$, the advanced position of any particle is

$$\begin{aligned}
x\left(t+\Delta t\right) &= x\left(t\right)+\frac{1}{\omega_c}\left[v_x\left(t\right)\sin\left(\omega_c t\right)-v_y\left(t\right)C\left(\omega_c t\right)\right]+\frac{1}{\omega_c^2}\cdot\\
&\quad\cdot\left[-a_x^C\left(t\right)C\left(\omega_c\Delta t\right)-a_y^C\left(t\right)S\left(\omega_c\Delta t\right)\right]+O\left((\Delta t)^3\right) && (3.57)\\
y\left(t+\Delta t\right) &= y\left(t\right)+\frac{1}{\omega_c}\left[-v_y\left(t\right)\sin\left(\omega_c t\right)-v_x\left(t\right)C\left(\omega_c t\right)\right]+\frac{1}{\omega_c^2}\cdot\\
&\quad\cdot\left[-a_y^C\left(t\right)C\left(\omega_c\Delta t\right)+a_x^C\left(t\right)S\left(\omega_c\Delta t\right)\right]+O\left((\Delta t)^3\right) && (3.58)\\
z\left(t+\Delta t\right) &= z\left(t\right)+\Delta t v_z\left(t\right)+\frac{1}{2}\left(\Delta t\right)^2 a_z^C\left(t\right)+O\left((\Delta t)^3\right). && (3.59)
\end{aligned}$$

Solving the Poisson equation the electrostatic field (i.e. $\vec{a}^C$) at the updated

positions is known and the velocities will be

$$\begin{aligned} v_x(t+\Delta t) &= v_x(t)\cos(\omega_c\Delta t) + v_y(t)\sin(\omega_c\Delta t) + \frac{1}{\omega_c}\left[-a_y^C(t)\,C(\omega_c\Delta t) + \right. \\ &\left. + a_x^C(t)\sin(\omega_c\Delta t)\right] + \frac{1}{\omega_c^2}\left[-\frac{a_x^C(t+\Delta t) - a_x^C(t)}{\Delta t}C(\omega_c\Delta t) + \right. \\ &\left. - \frac{a_y^C(t+\Delta t) - a_y^C(t)}{\Delta t}S(\omega_c\Delta t)\right] + O\left((\Delta t)^3\right) \qquad (3.60) \\ v_y(t+\Delta t) &= v_y(t)\cos(\omega_c\Delta t) - v_x(t)\sin(\omega_c\Delta t) - \frac{1}{\omega_c}\left[-a_x^C(t)\,C(\omega_c\Delta t) + \right. \\ &\left. - a_y^C(t)\sin(\omega_c\Delta t)\right] + \frac{1}{\omega_c^2}\left[-\frac{a_y^C(t+\Delta t) - a_y^C(t)}{\Delta t}C(\omega_c\Delta t) + \right. \\ &\left. + \frac{a_x^C(t+\Delta t) - a_x^C(t)}{\Delta t}S(\omega_c\Delta t)\right] + O\left((\Delta t)^3\right) \qquad (3.61) \\ v_z(t+\Delta t) &= v_z(t) + \frac{1}{2}\Delta t\left[a_z^C(t) + a_z^C(t+\Delta t)\right] + O\left((\Delta t)^3\right). \qquad (3.62) \end{aligned}$$

Validation tests, performed running the routine with a single ion in a harmonic potential and varying the time step, show that in our working conditions (B= 6 T and m/q$\sim 1 \div 3$, i.e. $\omega_c \sim 10 \div 100$ MHz) a reasonable compromise between accuracy and computational speed is $\Delta t = 5 \cdot 10^{-9}$. As a matter of fact, it is

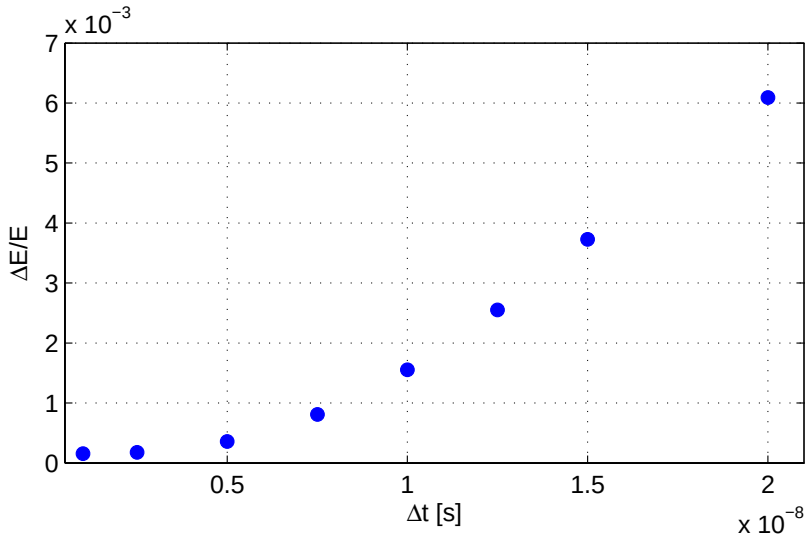


Figure 3.10: Dependence of the particle energy conservation on the time step chosen for the particle advancement with the modified Velocity Verlet. The deviation in energy is calculated over a total simulation time of 0.1 s. The chosen value is $\Delta t = 5 \cdot 10^{-9}$.

Table 3.3: Dependence of the energy conservation on the magnetic field. No increase is observed with rising $B$, as the trend is substantially constant.

| $B$ $[T]$ | 1 | 3 | 6 |
|---|---|---|---|
| $\Delta E/E$ | $2.570 \cdot 10^{-3}$ | $2.496 \cdot 10^{-3}$ | $2.365 \cdot 10^{-3}$ |

much smaller than the cyclotron period: nevertheless the limitation appears to be not the magnetic, but the electric field. The parameter of interest being the energy conservation along time (the sum of kinetic and potential energy must remain constant in absence of dissipative forces), one can verify that the dependence of relative energy deviation on the time step magnitude has a quadratic-to-cubic trend in the range $\Delta t \in [10^{-9} \div 2 \cdot 10^{-8}]$ (see Fig. 3.10). Larger time steps were not considered, as the axial motion (our main focus in the study of resistive cooling) begins to become very inaccurate. For smaller $\Delta t$, the main contribution to the energy non-conservation is in the radial plane.

Still this does not mean that the magnetic field is responsible. The proof of the algorithm independence on the B-field strength is given by tests at different B values; computations of the trajectory of a $U^{92+}$ ion in a harmonic potential well show that after a total simulation time of 1 second the relative error in the ion energy is always around $2.5 \cdot 10^{-3}$, as reported in Table 3.3.

As a comparison, a leapfrog and both 2nd-order and 4th-order Runge-Kutta routines were checked, but in all cases the particle got radially lost via energy non-conservation already after a simulation time of some milliseconds, although $\Delta t$ was further reduced to values between $10^{-10}$ and $10^{-11}$ seconds.

## 3.5 Benchmarking of the code

### 3.5.1 Singly charged ions

In order to have a comparison not only with the theoretical expectations but also with feasible results that can be obtained with a PIC code, we made a benchmarking test taking as a reference the simulations by Mitchell [Mit97] on singly-charged ions in a closed cylindrical Penning trap. The relaxation to equilibrium conditions of a constant-density cylindrical ion column is observed, and the quantities of interest are given by the accumulation limits in the trap volume that we have introduced in Sec. 3.2: the Brillouin density and the number of storable particles.

We reproduced the simulation by Mitchell creating a 1 mm-radius column of ions with mass $m = 100$ and charge $q = 1$ in a trap[5] with $L = 48$ mm,

[5]The size is very close to original values of $L = 50$ and $r_w = 25$ mm; the FFT method requires the number of grid points in the axial direction to be a power of 2. The geometry approximation alters all our parameters of interest only by a factor 0.96.

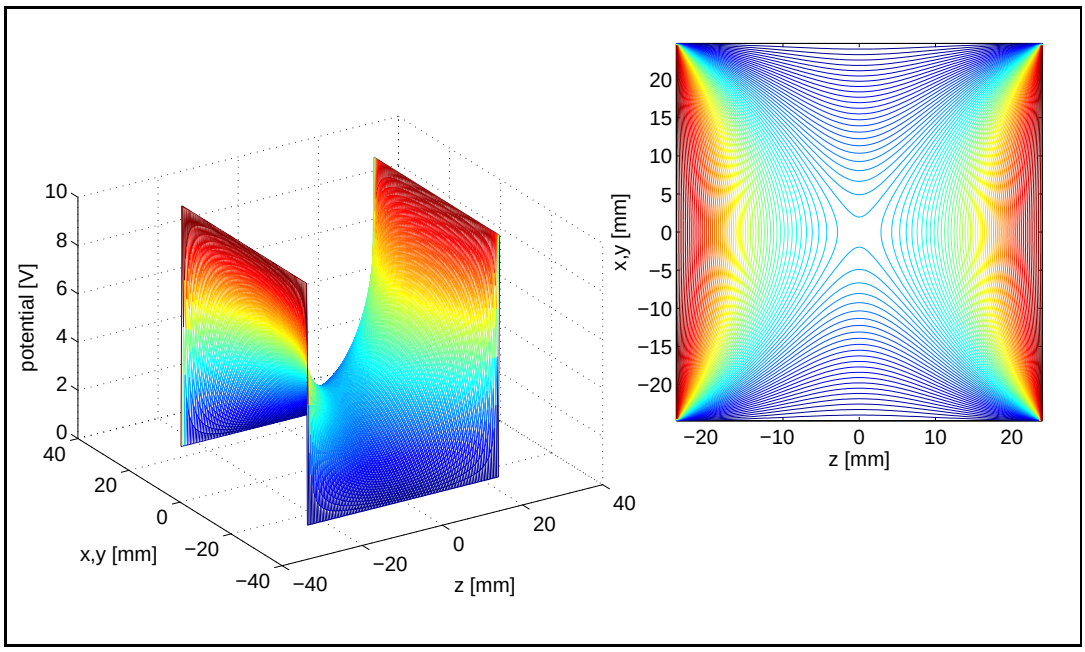


Figure 3.11: View of the electrostatic potential in a cylindrical Penning trap of length 48 mm and radius 24.75 mm. In absence of space charge, the potential in the center of the trap is approximated by a quadrupole which is confining in $z$ and deconfining in $r$.

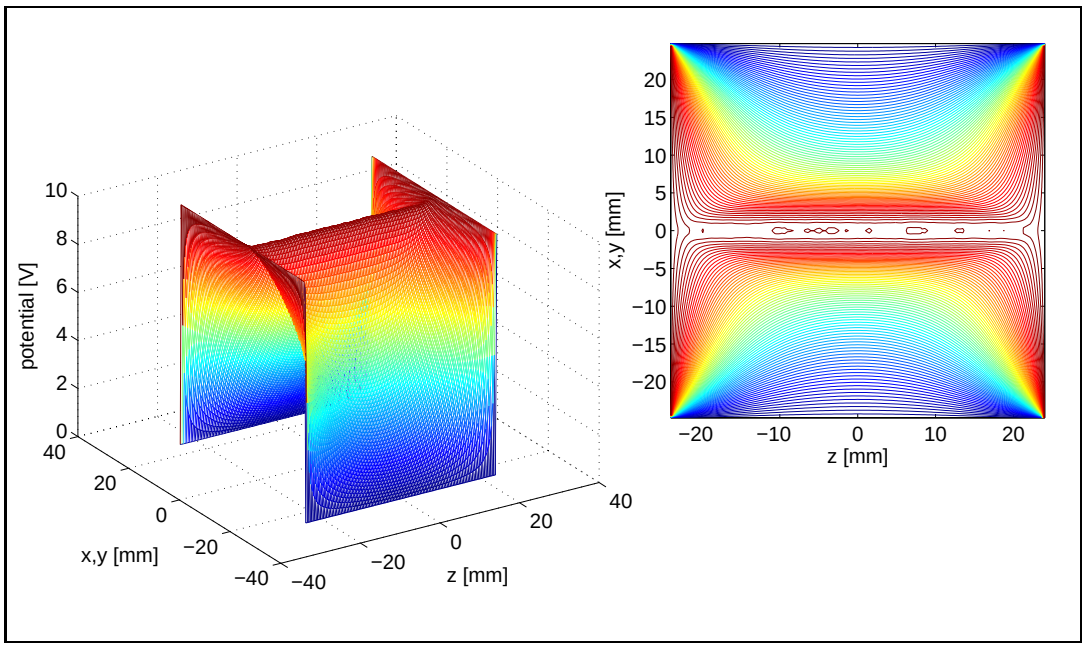


Figure 3.12: The trap of Fig. 3.11 has been filled with a column of ions along the longitudinal axis. The space charge cancels the confining potential. Other ions injected along $z$ would escape.

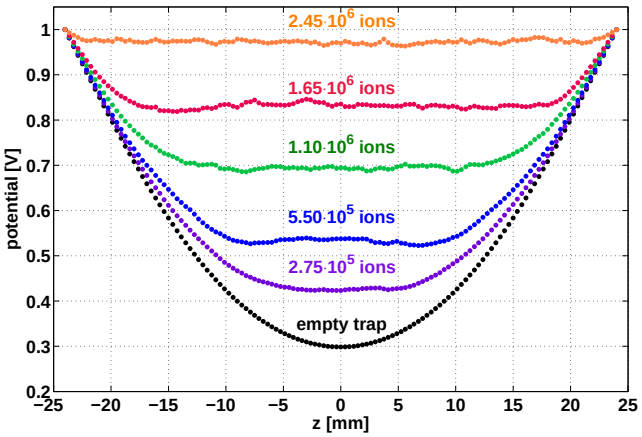


Figure 3.13: Electrostatic potential along the longitudinal axis for increasing number of stored particles. The trap of Fig. 3.11, 3.12 is progressively filled by singly charged ions of mass 100 amu. The initial parabolic well is increasingly flattened until it completely cancels the confining voltage on the endcaps. Small ripples occur as an effect of finite-size charges.

$r_w = 24.75$ mm, $B = 1$ T, and a spatial grid of $128 \times 66$ cells. The particles are injected over 0.5 ms, a time larger or at least comparable to the period of the axial oscillation ($\sim 0.044 \div 0.440$ ms), so that no unphysical cloud deformation occurs. Their relaxation to equilibrium is observed for a total simulation time of 2.5 ms.

The electrostatic potential in the empty trap is reproduced in Fig. 3.11, which shows the quadrupole shape in the center. Storage of particles is possible until the potential on the longitudinal axis is totally flattened like shown in Fig. (3.12). For this geometry Eq. (3.12) and Eq. (3.11) yield respectively $N = 3.15 \cdot 10^6 \cdot V_{endcap}$ and $n_B = 2.67 \cdot 10^7$ cm$^{-3}$. Table 3.4 summarizes the conclusions: endcap voltages of 0.1 and 1.0 V result in reaching the z-confinement limit before the Brillouin limit, since the approximate densities at maximum storage are $2.09 \cdot 10^6$ and $2.09 \cdot 10^7$ cm$^{-3}$. The column maintains a cylindrical shape, as shown in Fig. 3.14 (a) and (b). Further rise in the confining potential increases the number of trapped particles and hence the density at constant volume; the cloud undergoes a radial expansion and takes an ellipsoidal shape (see Fig. 3.14 (c)) in order to reduce the density in the center.

Notice that $N_{stored}$ does not go completely linearly with $V_d$: for low potential values the number of stored particles is lower than the theoretical prediction, while it approaches and overcomes the expected limit for increasing $V_{endcap}$. The Eq. 3.12 is anyway an approximation and our results show perfect agreement with Mitchell's values. A further remark: simulations with different numbers of superparticles show that the scaling does not influence significantly

Table 3.4: z-confinement as a function of endcap voltage and scaling factor in a cylindrical Penning trap of length 48 mm and radius 24.75 mm. The trap is progressively filled with singly charged ions of mass 100. The theoretical number of stored particles is $N_{stored} = 3.15 \cdot 10^6 \cdot V_{endcap}$. Notice the weak dependence on the scaling factor.

| $V_{endcap}$ $[V]$ | $N_{sim}$ | $n_{sc}$ | $N_{real} = n_{sc} \cdot N_{sim}$ | $N_{stored}$ |
|---|---|---|---|---|
| 0.1 | 5000 | 66 | $3.3 \cdot 10^5$ | $2.30 \cdot 10^5$ |
| 0.1 | 10000 | 33 | $3.3 \cdot 10^5$ | $2.32 \cdot 10^5$ |
| 1.0 | 5000 | 660 | $3.3 \cdot 10^5$ | $2.45 \cdot 10^6$ |
| 1.0 | 10000 | 330 | $3.3 \cdot 10^5$ | $2.47 \cdot 10^6$ |
| 10.0 | 5000 | 7500 | $3.75 \cdot 10^5$ | $3.49 \cdot 10^7$ |
| 10.0 | 10000 | 3750 | $3.75 \cdot 10^5$ | $3.50 \cdot 10^7$ |
| 10.0 | 25000 | 1500 | $3.75 \cdot 10^5$ | $3.51 \cdot 10^7$ |

the result, and that therefore we can safely reduce the simulation particles from the original number of 25000 with great spare of computation time. In setting the lower superparticle number, one must remind the necessity of statistics to have correct information on the properties at the equilibrium. $N_{sim} \sim 10^3$ represents a fair statistical sample.

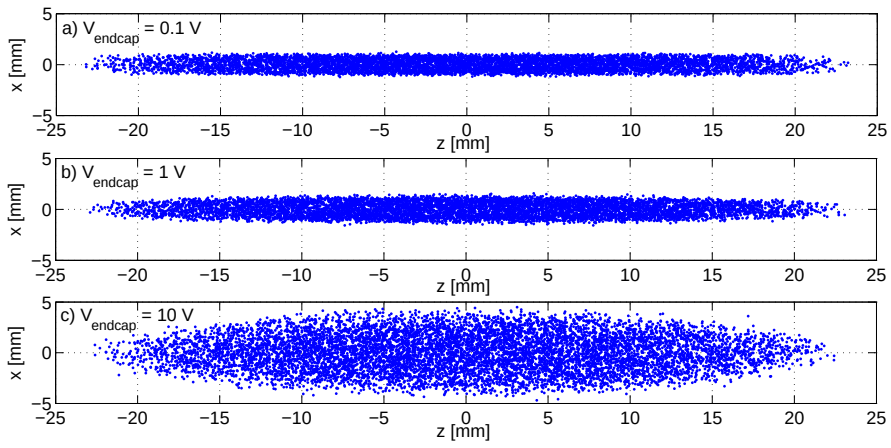


Figure 3.14: Equilibrium shape of an initially cylindrical cloud of singly-charged ions at the z-confinement limit in a cylindrical trap of length 48 mm and radius 24.75 mm, for different endcap voltages $V_{endcap}$. For (a) and (b) the Brillouin limit is not reached and no expansion occurs, whereas this is the case in subfigure (c).

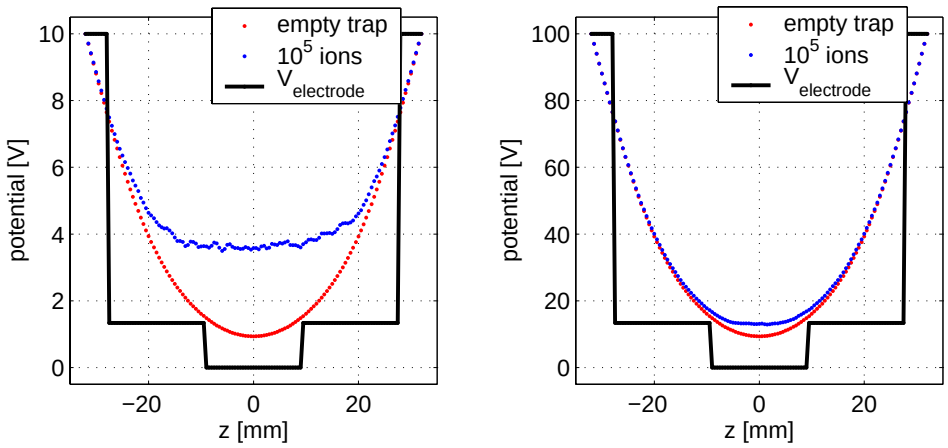


Figure 3.15: Potential flattening in the central nested trap of the Cooler Trap (length 64 mm and radius 17.5 mm) with $10^5$ $U^{92+}$ ions. A few Volts already efficiently trap the cloud, while the potential deformation becomes much less sensible at higher endcap voltages.

### 3.5.2 Highly charged ions

Coming to the actual conditions of interest, we have $10^5$ $U^{92+}$ ions in the central nested well of the Cooler Trap; the simulation volume has $r_w = 17.5$ mm and $L = 64$ mm with $\Delta z = 0.5$ mm, thus including three electrodes (plus 4 mm of the endcaps on each side, to reach a $2^n$-like number of grid points). Injection simulations yield a cloud radius $\rho_c \approx 1$ mm. With the abovementioned formulae, the z-confinement is $\approx 6.72 \cdot 10^4 \cdot V_{endcap}$ and the average density $n \approx 5 \cdot 10^5$ cm$^{-3}$, three orders of magnitude lower than the Brillouin limit $n_B \approx 4 \cdot 10^8$ cm$^{-3}$. Once the kinetic energy of the cloud has been reduced to the eV range (i.e. after electron cooling) as well as during the application of resistive cooling, the shape and density of the cloud will change. We will discuss these aspects in Sec. (4.3.4). For the moment we can anyway conclude that a potential of some Volts is sufficient to store the ion sample after electron cooling to 10 eV and no radial expansion is expected at this energy.

Simulations at different endcap potentials confirm what we said above. Let us just make a remark about the potential flattening on the axis. At low $V_{endcap}$ (Fig. 3.15), this effect is much more visible. A higher $V_{endcap}$ has nevertheless the effect of reducing the axial extension of the cloud. Since the potential deformation will result in frequency shifts that can affect detection and manipulation of the cloud, the choice of $V_{endcap}$ is therefore of great importance. We will come back to this point during the next chapter, when we extensively analyze the effects of the space charge on the detection and resistive cooling of the cloud.

# Chapter 4

# Simulation of the cooling mechanisms

The Cooler Trap has to bring the energy of the ion cloud down to 4 K. The use of highly charged or even bare nuclides puts severe constraints in terms of the cooling mechanisms that can be exploited. *Buffer-gas cooling*, where energy is carried away by collision with inert gases, is forbidden as charge exchange would depopulate the high-charge fraction of our sample. *Laser cooling* cannot be used with bare ions, since no electronic structure is available.

A suitable technique is *electron cooling*, an efficient tool to remove the ions' energy as far as electron-ion recombination does not play a major role. *Positron cooling* (which would avoid the problem of recombination) is based on the identical principle[1]. Another possibility is *resistive cooling*, where the flow of image charges induced by the particles on the electrodes is shortcut with a dissipative circuit, resulting in an energy loss by the ion cloud. This chapter will deal with the theoretical and simulation studies about these cooling mechanisms whose analysis is beneficial first of all in terms of design optimization. In addition to this, especially in the case of resistive cooling, a better understanding of the phenomenon is of broader interest in the trap community. As an example we can cite the experimental setup SPECTRAP (briefly described in Sec. 2.5), which is presently being installed at HITRAP and which will exploit the resistive cooling technique to perform laser spectroscopy on low-energy HCI [Vog05].

## 4.1 Electron cooling

The basic principle of electron cooling is the energy exchange via Coulomb collisions between a hot ion bunch and a colder electron sample. This technique has been extensively exploited to reduce transversal emittance and longitudinal

[1] *Proton cooling*, i.e. sympathetic cooling of hot ions with colder protons, had also been proposed for TITAN [Ryj05].

spread in storage rings where a collinear cold electron beam is merged with the circulating ions in a section of the ring and carries away energy before being deviated again from the ion path. The repetition of the process at each turn of the ion bunch with a new and cold electron beam yields a high ion beam quality within a few seconds [Pot90]. An example is the Experimental Storage Ring at GSI as we have already mentioned in Sec. 2.2.

Electron or positron cooling in traps has also been applied successfully in the last years, for instance at CERN in the antiproton traps ASACUSA [Ich01], ATHENA [Amo04], ATRAP [Gab99]. While in accelerators the cooling species is periodically renovated, traps store permanently the ions (or antiprotons) as well as electrons (or positrons). The electron sample is kept cold by energy loss via synchrotron radiation in the high magnetic field. This guarantees a fast ion cooling and makes this process attractive for HITRAP where the desired cycle time for loading the Cooler Trap is about 10 s. Nevertheless one should notice that there will be an intricate interplay between heating and cooling of the electron cloud, which will affect consequently the energy dissipation of the ion bunch. The whole process is highly nonlinear and disentanglement of the feedback effects must be evaluated numerically. In this Section we summarize the HITRAP-related studies on electron cooling that have been extensively presented and discussed in [Zwi05, Zwi06, Ner07].

The energy exchange between ions and electrons is described using some simplifying assumption. The conversion from the kinetic energy $E_i = \sum_{\mu}^{N_i} E_\mu$ of the $N_i$ ions to electron temperature $T_e$ is considered to be instantaneous and $T_e$ is assumed to be isotropic for further simplification. This can be written as follows:

$$\frac{3}{2} N_e k_B \frac{\mathrm{d}T_e}{\mathrm{d}t} = \frac{\mathrm{d}E_e}{\mathrm{d}t} = -\frac{\mathrm{d}E_i}{\mathrm{d}t} = -\sum_{\mu}^{N_i} \frac{\mathrm{d}E_\mu}{\mathrm{d}t} = -\sum_{\mu}^{N_i} m_\mu \frac{\mathrm{d}\vec{v}_\mu}{\mathrm{d}t} \cdot \vec{v}_\mu, \tag{4.1}$$

where $N_e$ indicates the number of electrons, $k_B$ the Boltzmann constant, $\mu$ a generic ion with position $\vec{r}_\mu$ and velocity $\vec{v}_\mu$. As ions are more energetic than electrons this represents a heating for $e^-$. On the other hand, the magnetic field $B$ will cause an exponential decay of $T_e$ to the ambient temperature $T_o \approx 4$ K by synchrotron radiation with a time constant

$$\tau_s = 3\pi\varepsilon_o \frac{m_e^3 c^3}{e^4 \mathrm{B}^2}, \tag{4.2}$$

where $\varepsilon_o$ is the dielectric constant, $m_e$ the electron mass, $c$ the speed of light, $e$ the electric charge. With $B = 6$ T one obtains a very short time constant $\tau_s \approx 0.1$. Notice now that the last term in Eq. (4.1) represents the energy loss of the ions as product of ion velocity and the force experienced by the ion itself. The latter is given by two contributions: the static electromagnetic field of the trap and the cooling force $\vec{F}$ exerted by the electrons. Summarizing,

the complete problem is described by the following system of equations:

$$m_\mu \frac{\mathrm{d}\vec{v}_\mu}{\mathrm{d}t} = qe\left(\vec{\mathrm{E}}\left(\vec{r}_\mu\right) + \vec{v}_\mu \times \vec{\mathrm{B}}\right) + \vec{F}\left(n_e, T_e, \vec{\mathrm{B}}, \vec{v}_\mu\right) \quad \forall \mu = 1, ..., N_i \tag{4.3}$$

$$\frac{\mathrm{d}T_e}{\mathrm{d}t} = -\frac{2}{3k_B N_e}\sum_{\mu}^{N_i}\frac{\mathrm{d}E_\mu}{\mathrm{d}t} - \frac{1}{\tau_s}\left(T_e - T_o\right), \tag{4.4}$$

where $n_e$ is the density of electrons. The crucial issue is to estimate correctly the cooling force. Its evaluation is complicated by the influence of the magnetic field, which breaks its isotropy and introduces a dependence on the direction of $\vec{v}_\mu$ relative to $\vec{B}$. Moreover, $\vec{F}$ is efficiently described by different models depending on the electron-ion relative velocity [Möl07]. It is not our purpose to discuss here the advantages and disadvantages of each of them. In our case, as we will show next, the heating of the electron cloud is very large, therefore the relative velocity is large too, and Coulomb collisions cause small energy transfers (weak coupling). In this regime, the small velocity exchange can be treated as a perturbation of the electron motion in a static electromagnetic field. A linear response method (in the framework of the dielectric theory) can therefore be used [Ner07]. A drawback of this method is the overestimation of the cooling force for ions moving parallel or almost parallel to the magnetic field lines. As this is a small fraction of all ions, the approximation is acceptable and comparisons with other methods (computationally more expensive) have shown a discrepancy of 20% at most.

Coulomb collision is not the only process we have to face: electron-ion recombination will certainly occur. Three-body recombination scales as $T_e^{-9/2}$ and is hence strongly suppressed by the massive electron heating. The dominant mechanism is radiative recombination (RR)

$$X^{q+} + e^- \rightarrow X^{(q-1)+} + h\nu \tag{4.5}$$

where the binding energy of the recombined ion-electron system is radiatively released. Using the RR cross section $\sigma_{RR}$ given in [Paj94], the instantaneous recombination rate for each ion $\alpha_{RR,\mu}(t)$ is the integral of the RR cross section times the electron-ion relative velocity $v_{r,\mu}$ over the electron distribution:

$$\begin{aligned}\alpha_{RR,\mu}(t) &= n_e \int \mathrm{d}^3 v_e v_{r,\mu}(t)\,\sigma_{RR}\left(v_{r,\mu}(t)\right)\cdot \\ &\cdot \left(\frac{m_e}{2\pi k_B T_e(t)}\right)^{3/2}\exp\left(\frac{m_e v_e^2}{2k_B T_e(t)}\right).\end{aligned} \tag{4.6}$$

The survival probability $P_{RR,\mu}(t)$, i.e. the probability that the $\mu$-th ion is still in the initial charge state at time $t$, is

$$P_{RR,\mu}(t) = \exp\left(-\int_0^t \mathrm{d}t' \alpha_{RR,\mu}(t)\right). \tag{4.7}$$

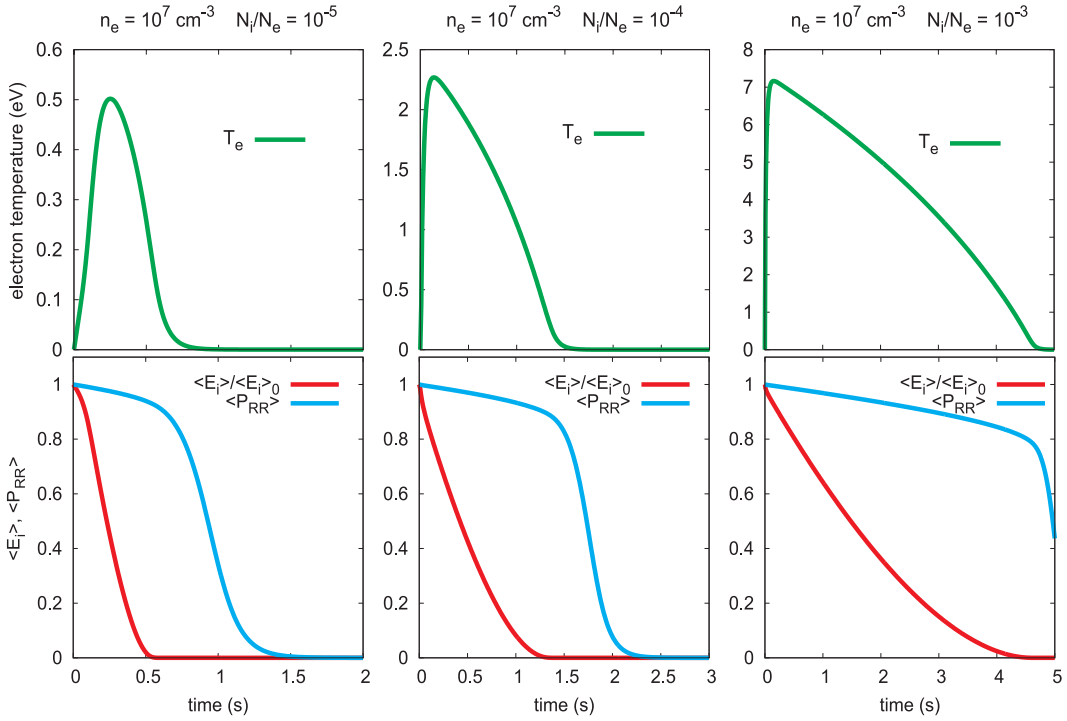


Figure 4.1: Electron cooling of $10^5$ $U^{92+}$ ions with different numbers of electrons. Diagrams in the top row show the electron temperature $T_e$ (green line) versus time where t=0 indicates the time of injection. On the bottom row, the red line indicates the mean energy $\langle E_i \rangle$ of the ions normalized to the initial mean energy $\langle E_i \rangle_o$. The blue line is the mean survival probability $\langle P_{RR} \rangle$ to electron-ion recombination. $n_e$ indicates the the density of electrons, $N_e$ and $N_i$ the number of electrons and ions, respectively.

Systematic studies have been performed to find a clear dependence of the recombination process on the number $N_e$ and density $n_e$ of electrons. The ion sample taken into consideration is that of the HITRAP Cooler Trap at injection: $N_i = 10^5$ $U^{92+}$ ions coming from the LEBT at 6 keV/u, decelerated to $1.5 \div 2$ keV/u by proper settings of the trap electrode potentials (see Sec. 3.3). The results are shown in Fig. 4.1 and 4.2. Qualitatively, electron cooling follows this scheme: As the ions are injected the Coulomb interaction starts and the ion energy $E_i$ drops continuously. The electron temperature conversely grows rapidly by about four orders of magnitude from $T_0 \approx 4$ K $\approx 0.35$ meV (cold electrons in equilibrium with the cryogenic temperature of the trap) to some eV. When the ion energy is sufficiently reduced, the energy exchange decreases and the cooling of electrons by synchrotron radiation dominates. At some point the ions would reach an equilibrium with the electron temperature and continue to cool down to $T_o$, but as ion and electron energies equalize radiative recombination increases and the HCI sample is progressively lost. It is therefore convenient to stop the process at some point by sweeping away the

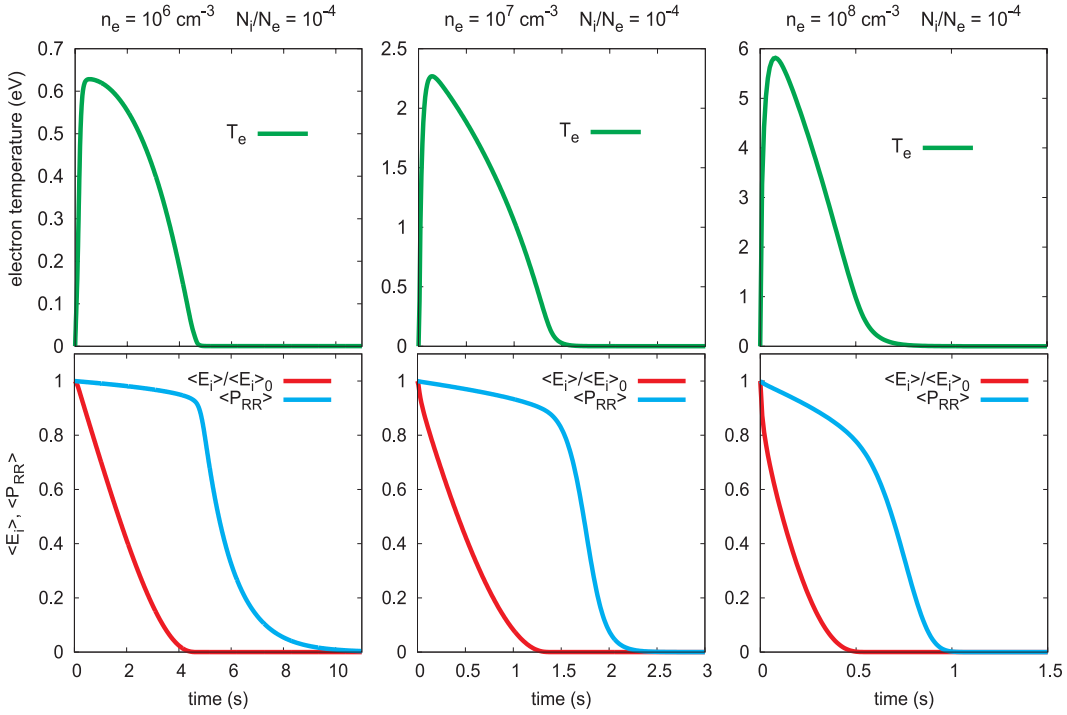


Figure 4.2: Electron cooling of $10^5$ $U^{92+}$ ions at different electron densities $n_e$. The ratio of ion and electron number $N_i/N_e$ remains constant. The electron temperature $T_e$ (green line) is shown in the top row, the ion energy (red line) and survival probability (blue line) in the bottom row. Notation follows Fig. 4.1.

electrons.

More quantitatively, Fig. 4.1 shows what happens while keeping constant $N_i$ and electron density $n_e$, but reducing the total number of electrons $N_e$. Less electrons to dissipate the same amount of energy means that their temperature rises faster in the beginning of the cooling process and reaches a higher maximum. The cooling force gets smaller at large $T_e$ and the cooling time increases. In principle the recombination rate decreases at higher $T_e$, but the increased interaction time prevails and the total amount of recombinations is bigger, i.e. the survival probability decreases for decreasing $N_e$ (from left to right in the picture). The conclusion is that a strong reduction of $N_e$ is disadvantageous.

Figure 4.2 shows the dependence of the electron temperature, the ion energy and the survival probability on the electron density at a constant ratio $N_i/N_e$. The cooling force has an almost linear relation to $n_e$ and increases with increasing $n_e$. Nevertheless a linear increase of $n_e$ does not result in a linear decrease of the cooling time, because the heating of the electrons is enhanced. Since the cooling force decreases at higher $T_e$, the energy loss of the ions is reduced. Comparing the three cases shown in Fig. 4.2 we can see that an increase of $n_e$ of one order of magnitude reduces the cooling time only of a factor $2 \div 4$. Equation (4.6) shows that the recombination rate depends linearly on

$n_e$. Conversely, $\alpha_{RR}$ is reduced at higher $T_e$. The examples show anyway that the density effect prevails and that for increasing $n_e$ the survival probability is lower.

Summarizing, the interplay between heating and cooling processes manifests in highly nonlinear effects which make estimates difficult when any parameter is changed. According to these simulations, the optimal settings are $n_e = 10^7$ cm$^{-3}$ and $N_e = 10^9$. Therefore these values were taken as design parameters for the Cooler Trap. With these settings (central diagram in Fig. 4.1 and 4.2) and stopping the electron cooling at an ion energy of 10 eV to limit recombination, we expect to have an efficient cooling of the ions in about $1 \div 1.5$ s and a survival probability of the ions' charge state of 90%. From this point on, electrons will be swept out of the trap by rapidly switching of the electrode potentials and resistive cooling will take over.

## 4.2 Theory of resistive cooling

Like laser [Bla06] or stochastic cooling[2] [Van84], resistive cooling is a ċlean' process [Maj04]. Here we mean that since no interaction with other particles is involved (which is the case, on the contrary, for electron or buffer-gas cooling), this technique does not substantially alter the content of the ion sample. The energy loss occurs in an external circuit, based on the same principle that is exploited for particle detection both in traps (where Dehmelt called it *bolometric* technique [Deh68]) and in accelerators (where it is known under the name of *Schottky* detection [Bos03]). Resistive cooling seems therefore a good candidate for the last part of the energy dissipation, where electron-ion recombination would change the charge state of the ion cloud. For the first part electron cooling is still preferred since it is definitely faster than resistive cooling, as we shall see.

In the following we introduce the concepts of image charge and image current. Their application in electronic detection and cooling of charged particles is presented with a focus on the features and problems of many-particles cooling.

### 4.2.1 Image charge

The presence of a boundary surface (e.g. a conductor held at a fixed potential) in the vicinity of a charged particle causes an apparent contradiction. The ion, inducing a surface charge density, would impose a different value of the electric potential on the boundary itself. A theoretical solution is given by the method

[2] Although most common in accelerators, stochastic cooling has been adapted to traps, too [Bev88, Bev88a]. Apparently it did not establish itself as a common technique, probably due to relatively long cooling times and the possibility of cooling directly only the center-of-mass motion of an ion cloud.

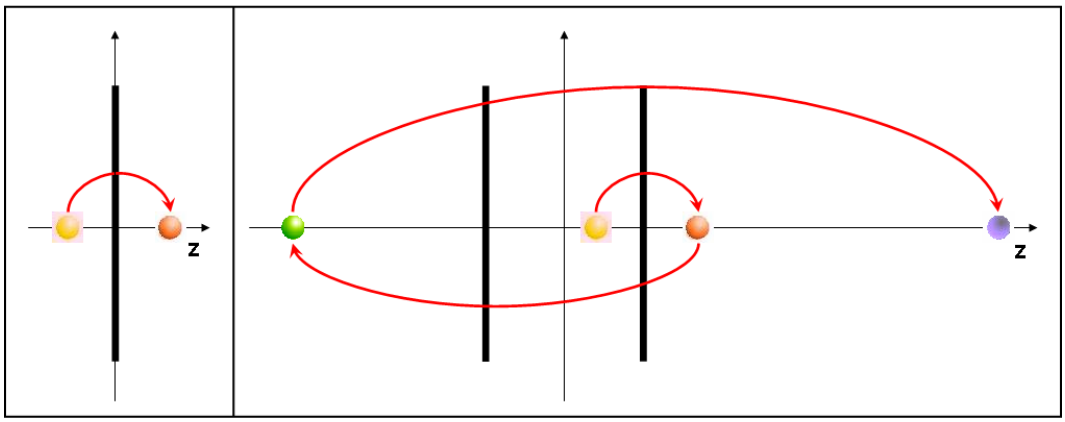


Figure 4.3: Scheme of the method of image charges. On the left, the charge placed on the left side of a plate induces an image on the right. On the right, the first image induces a subsequent one on the second plate and so on. An analogue series of images (not shown) is created starting from the left plate.

of *image charges* [Jac72]. This method considers a virtual charge of opposite sign, placed on the other side of the boundary, so that it mirrors the real charge and the result is a zero potential on the surface (see Fig. 4.3, left side).

One can evaluate the image charge by writing the potential given by both the real and image charges and then setting the result to zero. Gauss' law says then

$$q = \int_{\partial V} \sigma \mathrm{d}S = \int_{\partial V} \varepsilon_o \vec{E} \cdot \vec{n} \mathrm{d}S = \int_{\partial V} \varepsilon_o \vec{\nabla} V \cdot \vec{n} \mathrm{d}S. \tag{4.8}$$

Here $\sigma$ is the surface charge density, $\partial V$ the integration surface (i.e. the boundary), $\vec{n}$ the unit vector normal to $\partial V$, $\varepsilon_o$ the dielectric constant, $\vec{E}$ and $V$ the electric field and corresponding potential created by the charge and finally $q$ will be the total induced image charge. An analytical treatment of simple cases, such as a plate [Ble89] or a sphere [Jac72], is possible. It is indeed straightforward to write for a plate

$$\begin{aligned} q_{image} &= -\int_0^R \varepsilon_o E_z 2\pi r \mathrm{d}r = \\ &= -\int_0^R \frac{q}{2\pi} \frac{z}{\left(r^2+z^2\right)^{3/2}} 2\pi r \mathrm{d}r = -q\left(1 - \frac{z}{\sqrt{R^2+z^2}}\right) \end{aligned} \tag{4.9}$$

where R is the radial extension of the plate and $z$ the distance of the charge from the plate. If the plate extends to infinity, one obviously gets $q_{image} = -q_{real}$.

For boundaries with more complex geometries the solution is less trivial. In a capacitor made from two parallel plates, the image charge created on the other side of one of the plates has an effect on the other one an so on and so

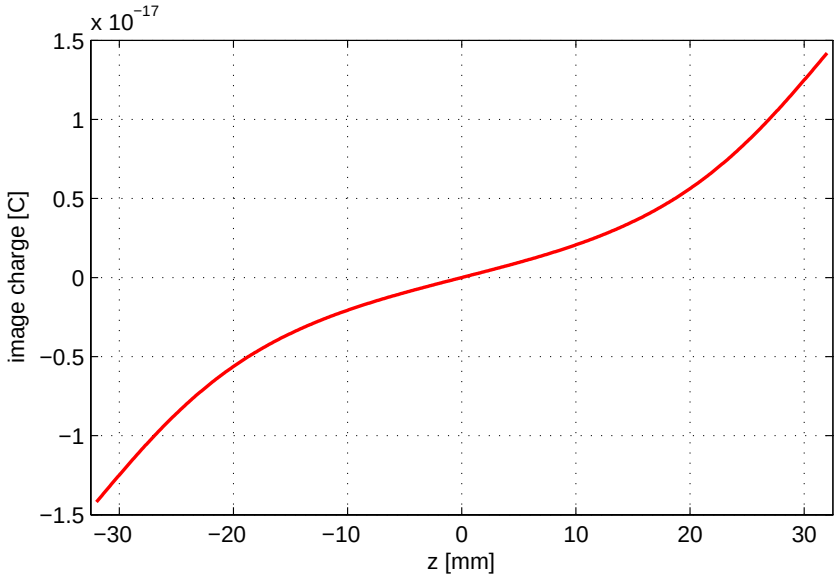


Figure 4.4: Net image charge $\Delta q^N_{cap}$ induced by a $U^{92+}$ ion trapped between the plates of a capacitor. The radius of the capacitor plates is $R = 17.5$ mm and their distance $d = 64$ mm. These values are chosen to simulate the central nested trap of the Cooler Trap. $z$ indicates the position of the ion between the two plates.

forth, giving rise to an infinite series of images (see Fig. 4.3, right side). The *i-th* image $q_i$ on the left ($L$) or right ($R$) plate is [Win06]

$$q_i^{L,R} = q(-1)^i \prod_{j=0}^{(i-1)/2} \frac{z_{2j+1}^{L,R}}{\left(R^2 + \left(z_{2j+1}^{L,R}\right)^2\right)} \prod_{j=1}^{(i-1)/2} \frac{z_{2j}^{R,L}}{\left(R^2 + \left(z_{2j}^{R,L}\right)^2\right)}, \tag{4.10}$$

where $z$ is the ion distance from the center of the capacitor, halfway inbetween the two plates, and $z_i^{L,R} = (2i-1)\frac{d}{2} \mp z(-1)^i$, and after some orders one can truncate the series since the influence of $q_i$ decreases for large $i$, especially if $R$ is large with respect to $z$. Connecting the two conductors to an external circuit one can measure the induced net charge (truncated to the $N-th$ contribution):

$$\Delta q^N_{cap} = q^L - q^R = \sum_{i=1}^{N} q_i^L - \sum_{i=1}^{N} q_i^R. \tag{4.11}$$

It is interesting to notice (see Fig. 4.4) that close to the center the image charge goes linearly with the axial displacement $z$ while, when getting closer to the plates, higher-order contributions become apparent. We will come back to this point later as it is of crucial importance.

In a hyperboloidal Penning trap or in a cylindrical trap with closed endcaps, the endcaps used as pick-ups electrodes for the induced images can be approximated by spheres or plates in case of hyperboloidal trap or closed cylindrical

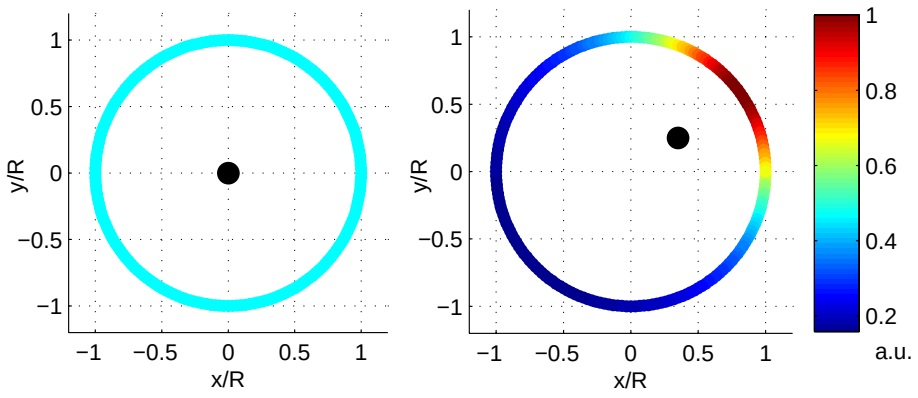


Figure 4.5: Charge density (colour-coded) on a conducting ring due to an ion (in black). The density is homogeneous if the particle is centered (a), and angular-dependent if the particle is off the center (b), due to the varying distance from the wall.

geometry, respectively. This is surely not possible in an open-endcap geometry, where the image charge is collected on the surface of ring electrodes. Therefore we carried further the approach sketched above to calculate the charge density in the case of a particle enclosed within a cylinder. Since the geometry is more complex, a fundamental simplification is required, namely the assumption that the ion moves only along the symmetry axis of the cylinder. Since we are interested only in the effect of the axial motion and do not consider the angular charge distribution in the transverse plane, this is acceptable. Indeed in a two-dimensional space, an ion induces a charge density with radial symmetry if the particle is put in the center of a conducting circular ring. An angular dependence arises upon a displacement from the center (see Fig. 4.5), but for Gauss' law the total charge integrated over $2\pi$ must be the same.

A further and non-trivial complication is the fact that in this case the image charge is represented by a continuous ring of charges with a radius larger than the circular electrode, compensating the potential of the real particle inside the conductor. But the presence of a continuous and homogeneous ring of images created by a charge in the center does not change the slope of the induced charge image versus the axial position. The only effect is to make the electric field at the wall stronger by a factor $\gamma$. This correction factor has not been derived analytically, but it can be evaluated numerically for each specific geometry and is in the range $1 \div 2$. In the geometries we will consider we found it to be close to 1.

With the abovementioned assumptions, we write the Gauss' law (Eq. (4.8))

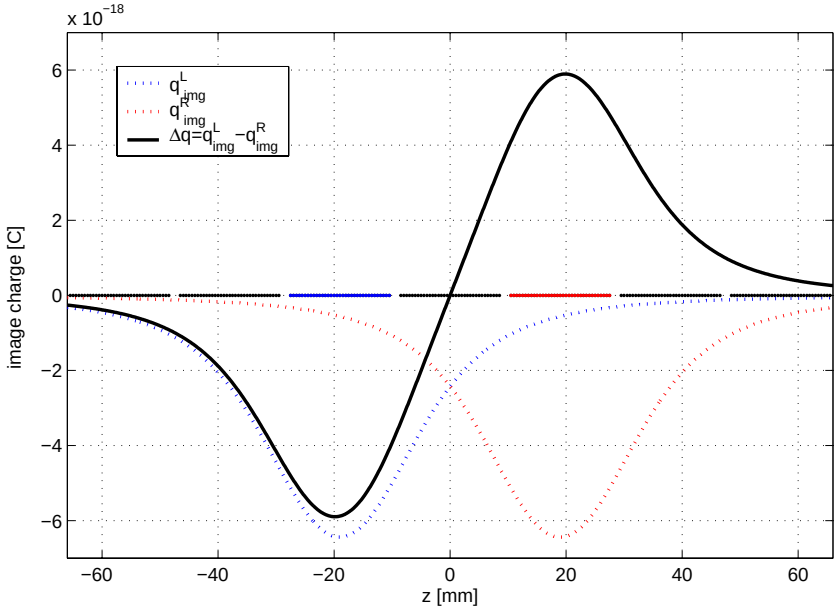


Figure 4.6: Image charge induced on the electrodes of a Multi-Ring Trap versus the position of the particle (here $U^{92+}$). The blue and red segments indicate the considered electrodes and the dotted lines the respective detected charge. The difference (net charge) is depicted in black. Geometrical parameters reproduce the Cooler Trap features.

for an infinitely long cylinder:

$$q = \int_{\partial V} \varepsilon_o \gamma \vec{E} \cdot \vec{n} \mathrm{d}S = \int_{-\infty}^{\infty} \int_0^{2\pi} \varepsilon_o \gamma E_r R \mathrm{d}\theta \mathrm{d}z = \frac{\gamma q}{4\pi} \int_{-\infty}^{\infty} \frac{2\pi R^2}{(R^2 + z^2)^{3/2}} \mathrm{d}z. \tag{4.12}$$

Let us now restrict the integral to a finite region, i.e. to a ring electrode. Its position with respect to the trap center is defined by the coordinates $[z_1, z_2]$. If the ion's instantaneous position is $z$, we get

$$q_{ring} = \gamma \frac{qR^2}{2} \int_{z_1 - z}^{z_2 - z} \frac{1}{(R^2 + z'^2)^{3/2}} \mathrm{d}z' = \gamma \frac{q}{2} \left[ \frac{z'}{(R^2 + z'^2)^{1/2}} \right]_{z_1 - z}^{z_2 - z}. \tag{4.13}$$

The image charge is then simply $q_{image} = -q_{ring}$ and, connecting two rings to an external circuit, the net image charge will be again the difference between the two contributions (see Fig. 4.6).

### 4.2.2 Image current through an external circuit

It is intuitive to imagine that, if an electric circuit shortcuts the electrodes of a trap, the movement of a trapped ion with an axial velocity $v_z$ will generate

a current $i$ due to the variation in time of the image charge $\Delta q$ induced on the electrodes' surfaces. This is described by

$$i = \frac{\mathrm{d}}{\mathrm{d}t}\Delta q = \frac{\partial}{\partial z}\Delta q \cdot \frac{\partial z}{\partial t} = v_z \frac{\partial}{\partial z}\Delta q. \tag{4.14}$$

Insertion of an impedance in the circuit gives then access to information and manipulation of the particle. This method is well known in the trap community: it was suggested already by Dehmelt [Deh68] and Wineland [Win75] who gave a thorough explanation of the phenomenon by showing the equivalence of a trap to an electric circuit. As a matter of fact, the system *trap + ion* can be modeled as a lumped circuit where the trap acts as a capacitor. A so-called *tuned circuit*, i.e. including LC elements, can be used for the detection of the ion axial oscillation if made resonant (tuned) with the frequency of the ion oscillation. Similarly, the radial motions can be observed, too, if an azimuthally-split ring electrode is used as pick-up and the image charge difference between the radial sectors is measured.

### 4.2.3 Dissipation of the image current

If the circuit that shortcuts the pickup electrodes includes a resistance, the effect is an energy loss by ohmic dissipation. The periodic motion of a particle is therefore assimilated to an alternate current whose amplitude is reduced in time. This corresponds to cooling of the ion oscillation. The minimum energy achievable is given by the ambient temperature at which the *circuit+trap* system is located. The minimum temperature represents a thermal noise (*Johnson noise*) which prevents the image current generated by the ion motion from being seen. The circuit will therefore be placed in the same 4-K environment of the trap. In reality, to accomplish this objective the use of a complex impedance (parallel RLC) is the common routine: the tank circuit[3] allows at the same time the observation of the ion's motion and a high effective resistance, i.e. a high dissipation of the image current and consequently of the ion energy. This would not be achievable with an ohmic resistor. Practically, an inductive coil is built while $C$ is given by the parasitic capacitance of the whole circuit including the trap electrodes. An index of the RLC circuit characteristics is given by the *quality factor (Q-factor)* which is defined as

$$Q = \frac{\omega_{RLC}}{\Delta\omega}. \tag{4.15}$$

Here $\omega_{RLC} = 1/\left(LC\right)^{1/2}$ is the resonance frequency and $\Delta\omega$ the bandwidth of the RLC circuit, defined as the width of the resonant peak 3 dB below the maximum. The peak resistance of the RLC given by

$$R = \frac{Q}{\omega_{RLC} C}. \tag{4.16}$$

[3]The RLC circuit is also called *tank* circuit because inductive and capacitive elements store energy.

To maximize the dissipation, the axial oscillation frequency of the ions $\omega_z$ must coincide with $\omega_{RLC}$. The evident drawback is the bandwidth of the RLC: particles oscillating with a frequency too far off $\omega_{RLC}$ will experience an effective resistance orders of magnitude lower than the peak value. We will see later that a broader bandwidth might be preferable to a high peak resistance. The common practice is anyway to aim for a high Q-factor when building the circuit and to artificially make it worse if requested. The resonant frequency is not a completely free choice as it depends on constructive parameters and the location of the whole system in the magnet bore puts space limitations. The coil for the resistive cooling in the Cooler Trap (being built and tested at the moment of writing) will have a Q-factor about 800 at $\omega_{RLC} \approx 400$ kHz, yielding (with an estimated $C$ of some tens pF) a peak resistance of $20 \div 40$ MΩ. A trapping potential of $\sim 100$ V in a nested trap of five electrodes is required to bring $\omega_z$ in resonance. The influence of these parameters on resistive cooling will be discussed in the next Section. More technical details on the electronics will be given in Sec. 5.3.

An estimate of the cooling process is straightforward in the approximation of a charge $q$ sinusoidally oscillating between two infinite plates at distance $D$ (a rough but fair first-order approximation of a hyperboloidal Penning trap). In this case the net transfer of charge $\Delta q$ is equal to $q$ when the particle moves from one conductor to the other. With an axial velocity $v_z$, the current is simply

$$i = \frac{q}{D} v_z. \tag{4.17}$$

Since the ohmic dissipation in the effective resistance $\mathbf{R}$ is[4] $P = \mathbf{R} I_{eff}^2$ and $v_z^2 = 2E_z/m$, the total energy loss of the axial component[5] follows the law

$$P = \frac{\mathrm{d}E_z}{\mathrm{d}t} = \frac{\mathbf{R}q^2}{mD^2} E_z \tag{4.18}$$

that yields an exponential decay with time constant

$$\tau = \frac{mD^2}{\mathbf{R}q^2}. \tag{4.19}$$

This result is also approximately valid when the pick-up electrodes are not infinite plates but finite slabs or rings as in a real cylindrical trap. Indeed as Fig. 4.4 and 4.5 show, in the central region the slope of the image charge is linear and for small oscillations the current formally follows Eq. (4.17) if $D$ is replaced by an effective distance

$$D_{eff} = -V_o \left( \left. \frac{\partial V}{\partial z} \right|_{z=0} \right)^{-1} \tag{4.20}$$

[4] $I_eff = \frac{i}{\sqrt{2}}$ is the efficient current: in the case of sinusoidal current $i$, the mean value of its square is $\langle i^2 \rangle = i_o^2 \left\langle (\cos(\omega t))^2 \right\rangle = \frac{1}{2} i_o^2 = \frac{q^2}{mD^2} E_z$. This explains a factor 2 otherwise missing.

[5] In the center, the energy is purely kinetic. The velocity varies sinusoidally and so does the current, therefore the footnote above holds.

with $V_o$ trapping depth.

Within this approximation, when $N$ ions of equal mass and charge state are trapped inside the capacitor, only the center-of-mass (CM) motion induces a net current. In the following, we will omit the index z for readability. Indeed for the j-th particle $v_j = v_{CM} + u_j$ and $\sum_{j=1}^{N} u_j = 0$ with $v_{CM}$ the velocity of the center of mass and $u_j$ the velocities in the CM frame. Hence the image current reads

$$i = \sum_{j=1}^{N} i_j = \frac{q}{D} \sum_{j=1}^{N} v_j = N \frac{q}{D} v_{CM}. \tag{4.21}$$

Now it would be intuitive to say that since the instantaneous dissipated power is proportional to $N^2$, the cooling time constant of the CM motion is $\tau_{CM} = \tau/N$, i.e., that the CM cooling is $N$ times faster than the damping of a single particle. On the contrary, it can be shown (see for instance [Maj04]) that due to the phase difference between the particles in the ensemble, the power dissipation, averaged over the sample and assuming that all particles have the same $\omega_z$ (which means also that $\omega_C M = \omega_z$), is $\propto N$ and therefore $\tau_{CM} = \tau$. We will notice in our simulations that a clear determination of $\tau_{CM}$ is rather difficult and ambiguous due to the time modulation of the amplitude of the CM motion and the frequency spread of $\omega_z$.

The important message is that while the CM motion experiences an effective cooling, the other degrees of freedom, which increase with the number of particles and therefore contain most of the energy in a large sample, are completely untouched. This is particularly intuitive when thinking of a 'breathing' motion (the $(2, 0)$ mode as we have defined it in Sec. 3.2), where the center of mass does not move but the ion cloud axially expands and contracts periodically: the charge induced on the two pick-up electrodes is the same and the net effect is null.

The real situation is anyway different, since the linear approximation of Eq. (4.17) is not really correct: one can see from eqs. (4.11) and (4.13) that higher orders of the axial position z come into play for high oscillation amplitudes. In general, the image of a charge $q_j$ can be written as a polynomial series of $z$

$$q_j = a_o + a_1 z_j + a_2 z_j^2 + a_3 z_j^3 + ... = \sum_{k=0}^{n_{max}} a_k z_j^k. \tag{4.22}$$

Making use of Eq. (4.14) the j-th image current will be

$$i_j = a_1 v_j + 2a_2 z_j v_j + 3a_3 z_j^2 v_j + ... = \sum_{k=1}^{n_{max}} k a_k z_j^{k-1} v_j \tag{4.23}$$

and the total current

$$i = a_1 v_{CM} + \sum_{k=2}^{n_{max}} k a_k \sum_{j=1}^{N} z_j^{k-1} v_j, \tag{4.24}$$

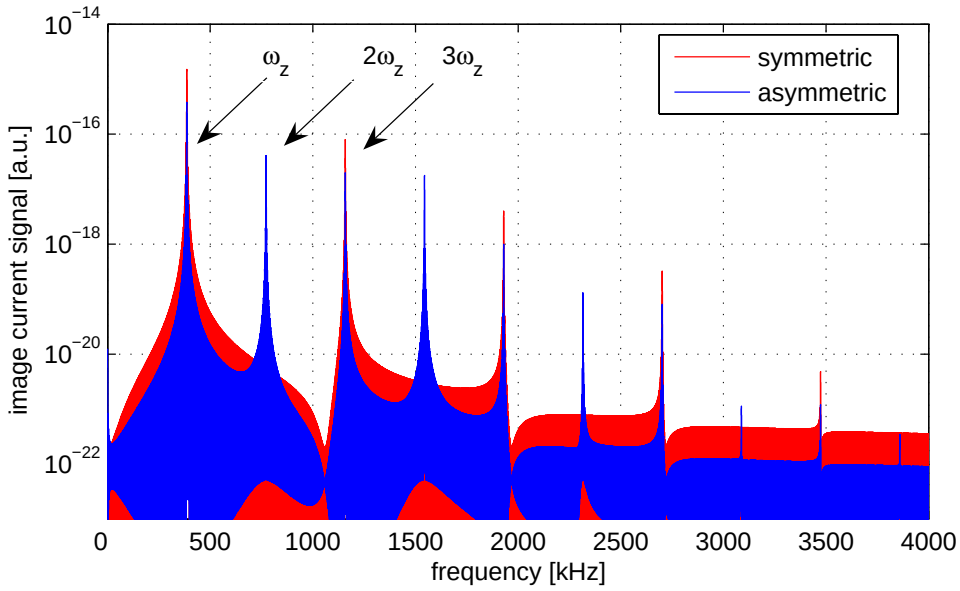


Figure 4.7: Spectrum of the image current induced by the motion of a $U^{92+}$ion on the pick-up electrodes with symmetric and asymmetric coupling. Higher harmonics visible due to the nonlinearity of the relation between ion motion and induced current (see Eq. (4.13)).

showing an additional term that will be dissipated beyond the pure CM motion. This contribution will be in general far smaller, resulting in a long cooling tail.

There are other causes that make the internal cloud motions ìvisible' in terms of an induced image current which can be damped. First of all there are unavoidable ìmperfections' of the real case in contrast to the ideal situation:

- anharmonicities in the trap electrostatic potential experienced by the particles either due imperfections or to very large amplitudes (since V deviates from a parabolic shape far from the center);

- the presence of partially recombined ions that leads to a displacement between the center of mass and the center of charge or, in other terms, to a fraction of ions with a different $\omega_z$ and therefore a variable phase shift.

Second, one can voluntarily choose an asymmetric coupling: instead of connecting the tuned circuit to two pick-up electrodes symmetrically placed with respect to the trap center, the detection of the image current can be done only on one side or with any axially asymmetric coupling scheme in order to be sensitive even to breathing-like motions. The effects of nonlinear correlations between ion motions and image current will be further investigated in the next Section, where we will obtain more quantitative results with the help of the

PIC code. Just as an example, Fig. 4.7 shows the spectra of the image current which is induced by a single $U^{92+}$ion in the case of symmetric and asymmetric coupling. The ion motion has a large amplitude ($\pm$18.8 mm) and enters the region of nonlinear function between ion motion and image current (see Eq. (4.13)), giving rise to higher harmonics of $\omega_z$. While the symmetric coupling renders visible only the odd ones, the asymmetric connection is sensitive to the even ones, too. Obviously its signal is lower when compared to the symmetrically coupled circuit, since only one pick-up electrode is use instead of two and the total detected current is lower.

The last and important remark regards the fact that we have only considered the cooling of the axial motion. Radial and azimuthal degrees of freedom also contain energy which has to be dissipated but will not be directly affected by axial cooling. A coupling of the transversal and axial motions is possible by resonant quadrupole excitation at the sum of the interested motions' eigenfrequencies. Therefore the transversal energy components can be indirectly damped by transfer to the axial motion, which is continuously cooled (*axialisation*). The limits for an efficient energy transfer are given by the spread of the eigenfrequencies of interest and the space charge of the cloud, screening the radiofrequency excitation applied to the electrodes. The overall result is an increase of the cooling times which we present in the next Section. Unfortunately our code cannot address this issue since it is built in $rz$-symmetry. Experimental investigations will therefore be necessary to give quantify these effects.

## 4.3 Simulation of resistive cooling

In this Section, after a brief explanation on the implementation in the PIC code, we will present the results obtained with our simulations on the mechanism of resistive cooling of highly charged ion clouds. As underlined in the introduction to this chapter, the purpose of the systematic studies is manifold. Besides the use in the Cooler Trap and the ensuing need for both an optimized design and a reference on the dynamics to guide the experimentalist, this cooling technique is also of interest for other Penning trap experiments. Systematic investigations are required not only for a deeper understanding of the cooling process, but also as a consequence of the limitations of the simulation code itself. The time span of the resistive cooling, as we shall see, covers at least several seconds. In Sec. 3.4 we have shown that the accuracy of our code is guaranteed only for few seconds, at most, with the chosen discretization parameters. Simulation of 1-second cooling time requires several days. Therefore an improvement in accuracy would be made at the expense of unacceptable periods of time for simulation. As a consequence, to limit the computational effort it is not possible to simulate a full cooling cycle under real experimental conditions as it will become clear from the presented examples. The study

of extreme cases can give an insight on the characteristic features of resistive cooling.

The benchmarking of the code is based on the only one published reference on resistive cooling of highly charged ions in a Pennning trap, i.e. the Mainz *g-factor* experiment on $C^{5+}$ [Häf00, Häf03]. The experimental finding will be compared with our simulations and interpreted. Subsequently, the properties of resistive cooling are analyzed as a function of the number of particles, the cooling power of the external circuit and the presence of contaminants. There are two advantageous circumstances for using the Mainz *g-factor* experiment for benchmarking: First, the simulation environment is smaller than the Cooler Trap and, as a consequence, the computation time is reduced by a factor $2 \div 4$. Second, we shall see that this setup and the Cooler Trap, although very different in size, have in common several features.

We shall then discuss resistive cooling in the Cooler Trap. Extensive simulations have been performed to gain information on the expected performance of the device.

### 4.3.1 Implementation in the PIC code

The most straightforward way to implement the resistive cooling in the simulation code is to evaluate the voltage drop on an external effective resistance as $\Delta V = R \cdot I$ and feeding back the cooling via a restoring force

$$F_z = qE_z \approx -q\frac{\Delta V}{D_{eff}} \tag{4.25}$$

counteracting the particle motion. $D_{eff}$, called effective electrode distance, is the separation between the infinitely extended plates of the ideal capacitor that would give the same electric potential as the real trap [Ota07]. Therefore, the axial electric field is approximated to the voltage drop over this length and the single-particle cooling time constant is directly given by Eq. (4.19).

Since this routine simply adds the restoring force on the electric field calculated via the Poisson solver, the result is correct only if the number of particles is very small and no space charge effect alters the field distribution. If this is not the case, the real force experienced by the ions is shielded by space charge and pure superposition overestimates $F_z$. A self-consistent implementation of the resistive cooling scheme in the PIC code requires therefore to incorporate a few intermediate steps in the main loop of Fig. 3.8:

- the calculation of the image current, accomplished using Eq.( 4.13);
- the calculation of the resulting voltage drop on the external RLC circuit $\Delta V = Z \cdot I$. If the impedance $Z$ is real (pure resistance) the voltage drop is simply the product of current and resistance. Otherwise $\Delta V$ is evaluated with a numerical time-domain routine that solves the second-order differential equation describing the circuit;

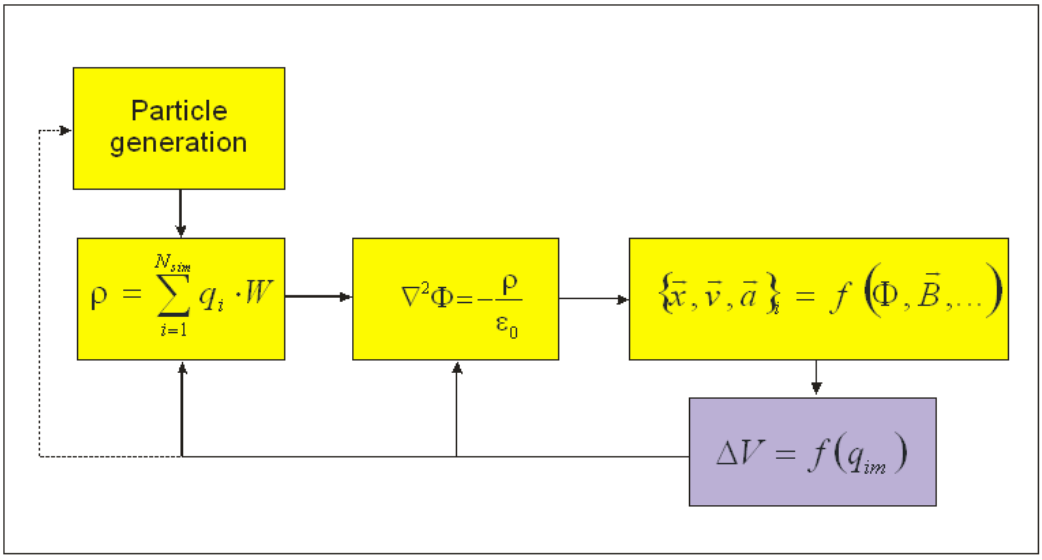


Figure 4.8: Scheme of the PIC code after introducing the feedback on electrode potentials (i.e. boundary conditions) due to image charge. An intermediate step is inserted in the main loop of Fig. 3.8. The particle movement creates an image current and a subsequent voltage alteration on the trap electrodes, creating new boundary condition for the Poisson equation.

- the feedback of $\Delta V$ to the pick-up electrodes which will modify the boundary conditions for the electrostatic potential in the Poisson solver routine.

The modified scheme is shown in Fig. 4.8. After advancing the ions one time step further, their new coordinates not only determine the charge density to be accounted for in the Poisson equation, but generate together with the velocities new boundary conditions via the image current.

Before we discuss the results of the simulations, we would like to make here some general remarks which we shall later give for granted unless otherwise stated:

- The clouds simulated in the following have been created with an initial random space distribution (i.e. uniform density) and a Gaussian velocity distribution. Since the resistive cooling acts directly only on the axial component, the mean energy of the sample we will refer to is always the axial component of the kinetic energy $E_{k,z}$. In principle, this component is the only one affected by the cooling process.

- At equilibrium, no center-of-mass (CM) motion is present. Since we want to study the cooling of the CM as well as internal motion the generated particle cloud will have (if not otherwise stated) part of the energy stored in the rigid CM oscillation.

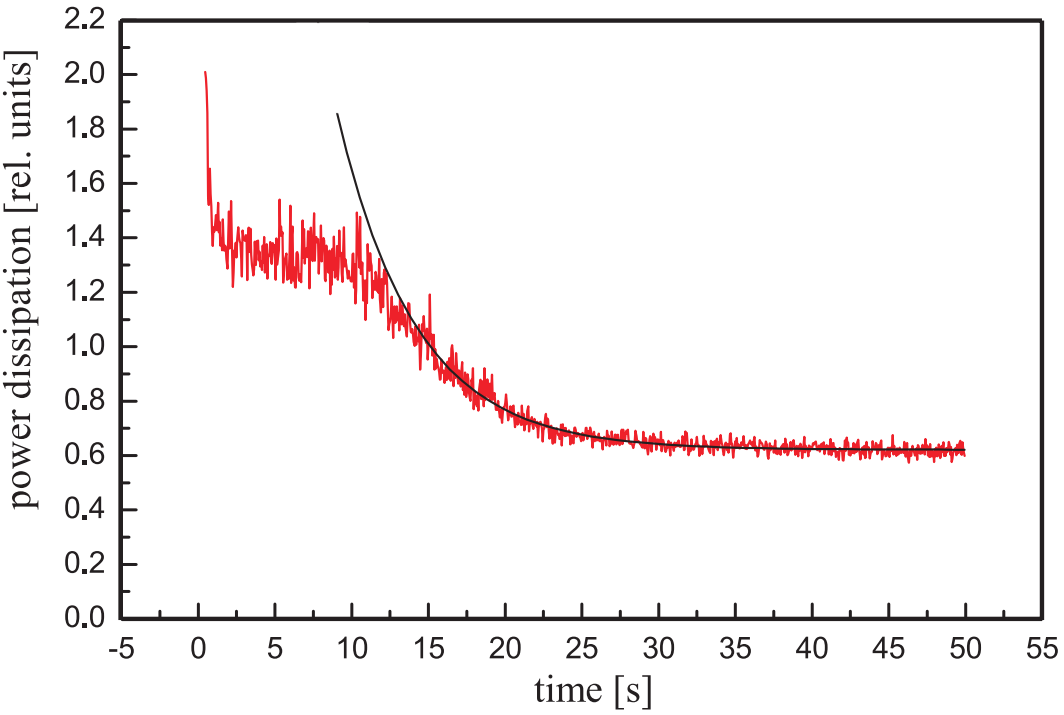


Figure 4.9: Experimental result for cooling of thirty $C^{5+}$ ions in a Penning trap [Häf03]. The black solid line is an exponential with decay constant $\tau = 5.2$ s fitting the experimental curve for $t \geq 10$ s (cooling of the internal motions of the cloud). The lower limit is set by the electronic noise at 4 K.

- As there is no direct collision mechanism in the PIC, the radial distribution is not influenced by axial resistive cooling unless the increase of space charge due to the axial compression causes a radial expansion.

- Although the experimental observable in electronic, non-destructive detection trap techniques is the induced current or power loss, the diagrams showing the time evolution of the ion cloud will essentially plot the kinetic energy as a function of time. The reason is the following: To first order, the two quantities are directly proportional as we have already shown in Sec. 4.2.3. They are thus exactly equivalent for CM motion. The linear relation is altered by the additional terms coming from anharmonicities and non-CM motions. Therefore, if our purpose is to clarify what is really happening to the ion sample, the current might not be the proper quantity.

### 4.3.2 The $C^{5+}$ trap: comparison with a real case

As stated in the beginning, the benchmark case for testing our code is the Mainz trap used for the g-factor experiments on $^{12}C^{5+}$ [Häf00, Häf03] since it

represents so far the only published experiment dealing with resistive cooling of a cloud of highly charged ions in a Penning trap. In the experiment, a sample of thirty $C^{5+}$ ions was trapped in a cryogenic, orthogonally-compensated cylindrical Penning trap. The endcap-to-endcap length was 16 mm, the diameter 7 mm and the magnetic field was 3.8 T. The trap was equipped with an RLC circuit of peak resistance R= 10 MΩ and quality-factor Q=1000, connected asymmetrically to an endcap and an adjacent correction electrode. The ion cloud had an initial mean kinetic energy of 13 eV and was confined by a trapping potential of 10 V. In these conditions, the axial frequency $\omega_z$ is about 800 kHz. As we mentioned before, the conditions for the HITRAP Cooler Trap are, although very different in size, quite similar to those of the Mainz *g-factor* trap: $U^{92+}$ has m/q= 2.6 and a $\omega_z \approx 2\pi \cdot 400$ kHz (in the central nested trap at 100 V trapping potential) while $C^{5+}$ has m/q is 2.4.

In the experiment, a single particle and also particle clouds were cooled. The measured single-particle cooling time constant $\tau_s = 132$ s is in agreement with the theoretical prediction of Eq. (4.19). The experiment on 30 ions presented more intriguing and unclear properties. Figure 4.9 shows the power dissipation in the RLC circuit measured over one minute[6]. The evident features are the very fast initial decay, an intermediate plateau and a successive, slower decay (*cooling tail*) whose time constant $\tau_{tail}$ is about 5.2 s. Häffner et al. interpreted the first fast slope of the dissipation process shown in Fig. 4.9 as cooling of the CM motion and the slower tail as decay of the internal motions in the ion cloud. A conclusive explanation of the intermediate plateau could not be given.

Due to accuracy loss and excessive computational effort, our simulations cannot cover the full time span of one minute which was experimentally observed but only few seconds. In order to have useful results within the affordable simulation time, we maintained all parameters of the experiment except for the peak resistance: this was increased to $R = 10^{10}$ Ω, i.e. by three orders of magnitude. The underlying assumption, that the physics of cooling is not qualitatively altered, is justified as far as the voltage drop due to the image current is a small distortion of the trapping potential. In other words, the cooling force acting on the ions must not become strong enough to turn from a damping force to an excitation drive. We verified that even with our boosted resistance we do not encounter this problem.

Figure 4.10 shows the result of a cooling simulation of a single $C^{5+}$. The sinusoidal oscillation (not resolved in the diagram) of the particle motion, shown on the left, is damped exponentially. The same happens to the axial component $E_{k,z}$ of the kinetic energy, plotted in the logarithmic plot on the right. To better understand the picture, we recall that the total energy of the particle being the sum of potential ($E_p$) and kinetic ($E_k$) energy, both oscillate with a phase shift of $\pi/2$. The observation of the decay of one component is

[6]To avoid confusion we remark that this is the only experimental data diagram we show in this chapter. All pictures that follow present the results of our simulations.

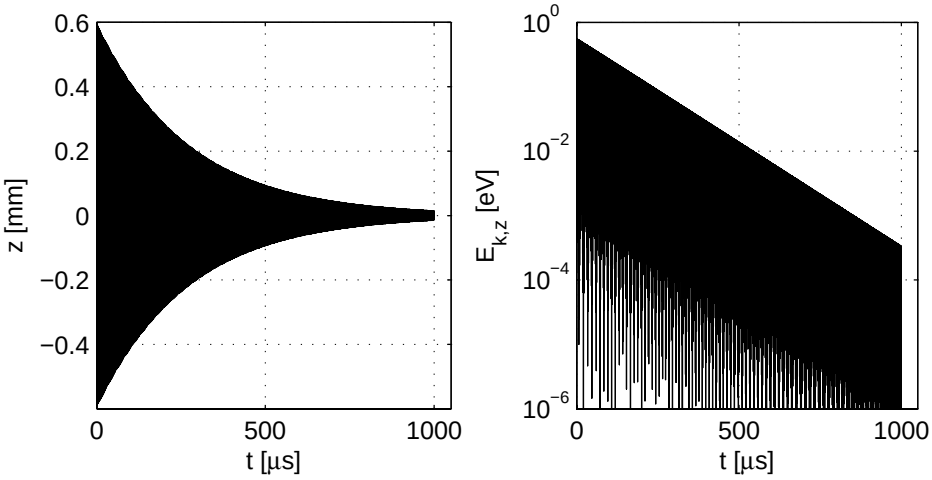


Figure 4.10: Simulated resonant resistive cooling of a single $C^{5+}$ ion simulated with the geometrical conditions of the trap described in [Häf03]. On the left, the axial motion is plotted. The oscillation at $\omega_z$ (not resolved here) is exponentially damped and the axial component of the kinetic energy (on the right) decreases with $\tau = 134$ $\mu$s. As expected, this is 1000 times faster than observed experimentally, due to the use of a peak resistance 1000 times higher than the one used in the experiment.

sufficient and it is indicated by the slope of the maximum values of either $E_k$ or $E_p$ over a period. In this as well as in the upcoming plots, the decay can be seen as the slope of oscillation maxima.

The time constant extracted from the simulation is $\tau = 134$ $\mu$s, i.e. three orders of magnitude smaller than in the experiment. Scaling inversely with the 1000-fold increased resistance value, experiment and simulation agree perfectly with each other. Systematic variation of the resistance showed the expected dependence between $\tau_s$ and $R$ as given in Eq. (4.19).

Simulation of the cloud of 30 ions yields a striking result. Figure 4.11 shows both the CM kinetic energy and the mean total $E_k$. The qualitative agreement with the experimental slope shown in Fig. 4.9 is evident, as fast damping, plateau and slow tail are visible in the mean energy plot. We have seen in Sec. 4.2.3 that the cooling time constant of the CM motion should be equal to the one of the single particle. Unfortunately, the amplitude of the CM oscillation (even for an undamped motion) is modulated and this makes the determination of $\tau_{CM}$ very ambiguous. The CM plot gives nonetheless an unexpected information: although most of the CM energy has been damped in the first part ($t \lesssim 50$ ms) and no cooling takes place in the plateau ($t \lesssim 548$ ms), there is still another fast decrease at $t \approx 548$ ms followed by a slow decrease of the energy (the cooling tail) for $t \gtrsim 550$ ms. slow tail sets in after the stationary part. This agrees only fairly with the explanation given above for the experimental result and suggests the presence of a more complex

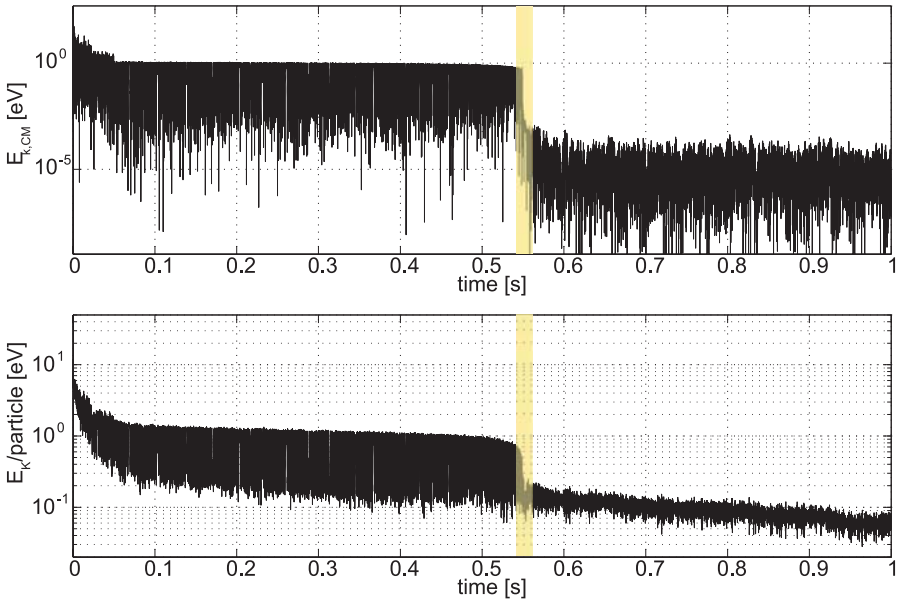


Figure 4.11: Simulated cooling of thirty $C^{5+}$ ions with an RLC circuit. Peak resistance R=$10^{10}$ Ω is 3 orders of magnitude higher than in the experiment. The upper diagram shows the evolution of the axial component of the center-of-mass kinetic energy $E_{k,CM}$. The lower diagram shows the total axial kinetic energy $E_k$ per particle (mean kinetic energy).

phenomenon.

For the interpretation of this feature it is helpful to look at the Fourier transform of the image current which gives the frequency information on the detected signal. The frequency spectra of Fig. 4.12 have been taken at the start ($t = 0$) and the end of the simulation ($t = 1$ s). At the beginning the broad energy distribution of the ions makes the spectrum very noisy: the frequency spread is large and $\omega_z$ (theoretically at 800 kHz) hardly identifiable in a broader and shifted peak. Cooling has two effects which are visible from the spectrum taken at $t = 1$ s. The first is a decreasing signal amplitude, since part of the ion energy has been dissipated and the image current is reduced. The second is a much clearer and sharper spectrum where the peak broadening is strongly reduced and the CM axial frequency frequency at $\omega_z = 800$ kHz and its higher harmonics become clearly visible. The asymmetric coupling renders visible the even harmonics, too. Notice that the second and third harmonic are very strong, indicating the presence of anharmonic components in the power dissipation (either due to nonlinearities in the ion-image current relation or to anharmonicities of the high-amplitude ion oscillations). Other frequencies are also present and are candidates for other plasma modes, i.e. non-CM motions.

The reason for this evolution can be better understood by looking at a

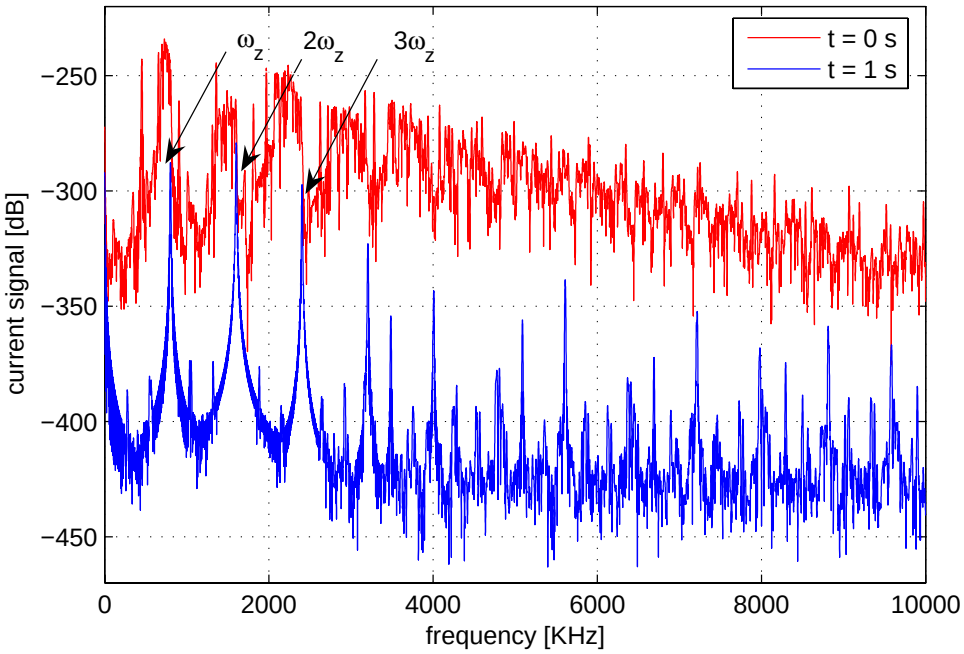


Figure 4.12: Frequency spectrum of the current induced by the axial motion of a cloud of thirty $C^{5+}$ ions before and after cooling for 1 second. The axial frequency $\omega_z$ and several higher harmonics are indicated.

spectrogram where the frequency spectrum is plotted versus time. The most significant part is depicted in Fig. 4.13 recorded in the time window of the energy jump (indicated in yellow in Fig. 4.11), between 0.54 and 0.56 s. Since the peak resistance of the RLC circuit is at the theoretical value of $\omega_z$, the feedback signal is maximum for the ions whose oscillation is close to that frequency and forces all ions towards the same frequency. The initial frequency distribution is progressively shifted and narrowed until there is only a sharp peak at the optimum axial eigenfrequency $\omega_z = \omega_{RLC}$. This effect is most easily noticed at the higher harmonics, where it looks magnified. The fast decrease in energy takes place at $t = 547.6$ ms, at the end of this frequency rearrangement. Afterwards the frequencies do not change further. The only variation is in the intensity of the signal which is damped with a cooling time constant $\tau_{tail} \approx 0.52$ s.

Summarizing, we can interpret the plateau as a region where the main process is the reorganization of the ion motion under the effect of cooling. This reduces their axial frequency broadening after which further cooling can take place, both for the CM and the internal motions.

As a final remark notice that the time constant of the tail resulting from the simulation (0.52 s) is just ten times smaller than the experimental value (5.2 s) while the peak resistance was increased in the simulation by three orders

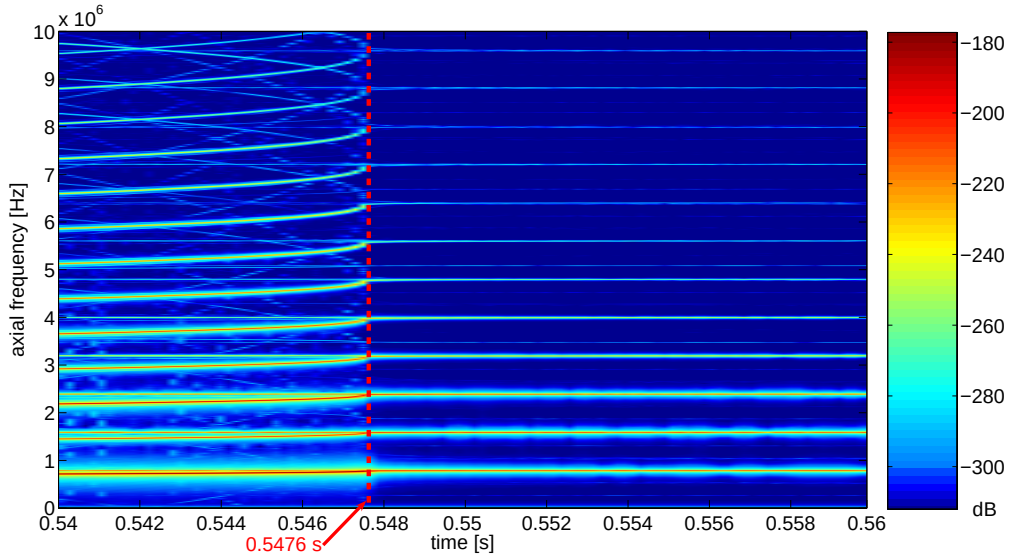


Figure 4.13: Frequency spectrum of thirty $C^{5+}$ ions during cooling in a Penning trap as a function of time for $0.54 \leq t \leq 0.56$ ms, i.e. the time interval indicated in yellow in Fig. 4.11. The time $t = 547.6$ s of the fast energy decrease at the end of the plateau is indicated by the red dashed line.

of magnitude. The cooling tail sets in at $t \approx 0.5$ s against the 10 s of the experiment shown in Fig. 4.9, i.e. only 20 times faster than in reality. This indicates a very limited influence of the peak resistance value on the cooling of the non-CM motions.

### 4.3.3 Systematic studies on the $C^{5+}$ trap

In this Section the scaling of resistive cooling will be investigated in order to obtain estimates for experimental conditions, i.e. when large ion ensembles are cooled by the use of a real tank circuit of limited peak resistance. We also address the influence on cooling when ions with different m/q are present in the cloud. All simulations start with ion clouds that have a mean axial kinetic energy in the order of 10 eV. This is the initial energy for the ion clouds of both the Mainz experiment (our starting point for these studies) and the Cooler Trap after the electron cooling is stopped.

#### Scaling of cooling with the number of particles

The number of possible internal modes and, accordingly, the energy stored in non-CM motions increase with the number of particles in the cloud. The cooling time of the slow tail $\tau_{tail}$ becomes then more and more important and, intuitively, the proportionality between dissipated power and remaining kinetic

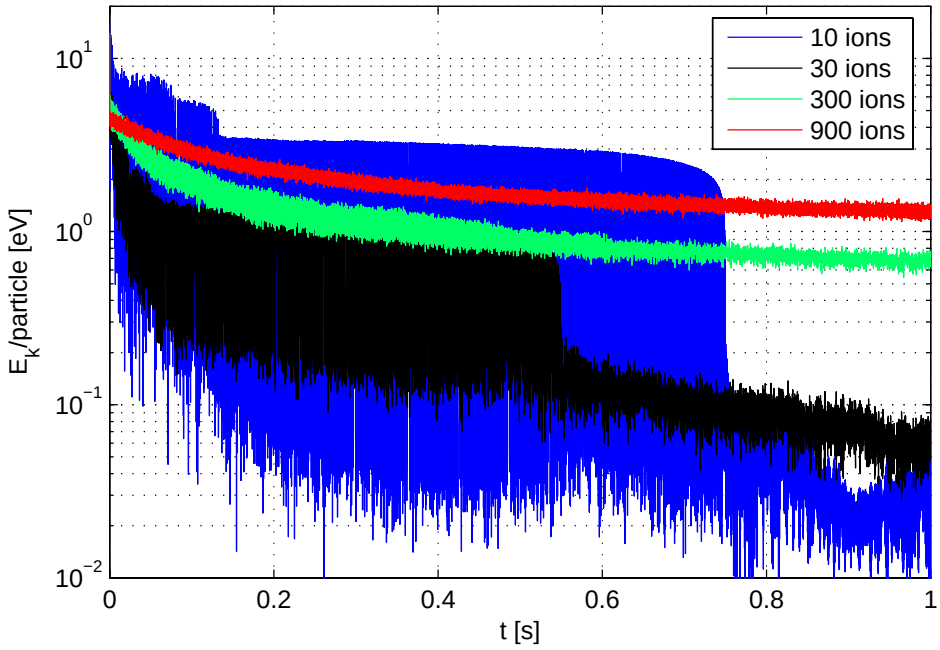


Figure 4.14: Simulated cooling of the axial kinetic energy of different numbers of $C^{5+}$ ions with an RLC circuit. Although hardly visible due to the initial fast cooling of the CM motion, the initial energy of all samples is about 10 eV.

energy deviates stronger and stronger from linearity making direct theoretical estimates impossible. Simulations of $N = 30 \div 900 C^{5+}$ ions stored in the Mainz trap have been performed using always an RLC tank with a peak resistance of $10^{10}$ MΩ. The total simulation time was limited to $1 \div 2$ s.

As it can be seen in the Fig. 4.14, showing the mean axial kinetic energy per particle versus time, $E_k$ decreases slower with increasing number $N$ of particles. Moreover, the plateau gets shorter and the fast decay at the end of the plateau, very evident for low numbers of ions, disappears completely for more than $\sim 100$ ions. The CM energy shows the same behaviour. These features can be once again explained with the help of frequency spectra of Fig. 4.15, where initial and final spectra of the image current induced by 300 ions are plotted. These present qualitatively the same features as the simulation with 30 particles: an initially broad distribution of frequencies (more and more smeared with increasing $N$) which collapses to $\omega_z$ and its higher harmonics when progressively cooled (again with some additional frequencies attributed to collective modes). The disappearance of the plateau and of the following steep energy decrease for $N \geq 300$ can be explained as an effect of slower cooling where the more gradual narrowing of the frequency distribution corresponds to a reduced and more continuous energy loss. This explains also why the tail sets in at an increasing energy value for increasing $N$. Notice that

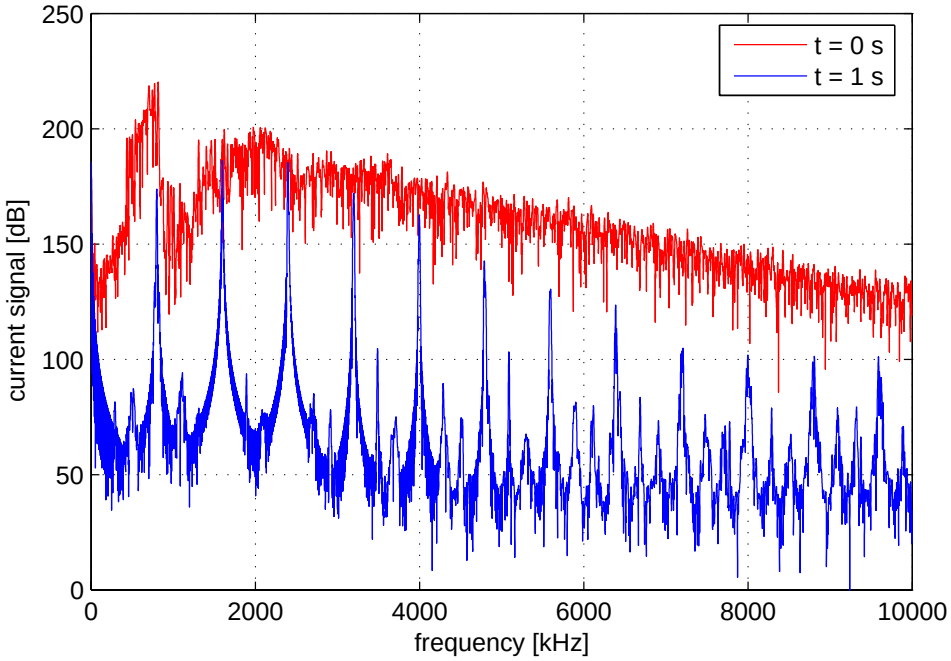


Figure 4.15: Frequency spectrum of the current induced by the axial motion of a cloud of 300 $C^{5+}$ ions before and after cooling for 1 s.

for low number of $C^{5+}$ ions (see curve for $N = 10$ in Fig. 4.14), the cooling curve ions shows some clearly resolved additional energy jumps in the first part ($t \leq 133$ ms), interpreted as the shifts of individual or part of the ions towards $\omega_z$.

Table 4.1: Cooling time constant $\tau_{tail}$ of the slow tail as a function of ion number for clouds of $C^{5+}$ ions cooled by an RLC circuit.

| Ion number | $\tau_{tail}$ [s] |
|---|---|
| 30 | 0.52 |
| 60 | 0.92 |
| 150 | 2.30 |
| 300 | 3.13 |
| 900 | 4.33 |

Despite the disappearance of the plateau and of the following fast energy decrease, the tail can be still be identified and its time constant $\tau_{tail}$ determined. Indeed we can define the tail as the part where no CM energy is dissipated anymore. An exponential fit of the energy slope yields then $\tau_{tail}$. $\tau_{tail}$ versus the particle number $N$ is reported in Table 4.1 and in Fig. 4.16.

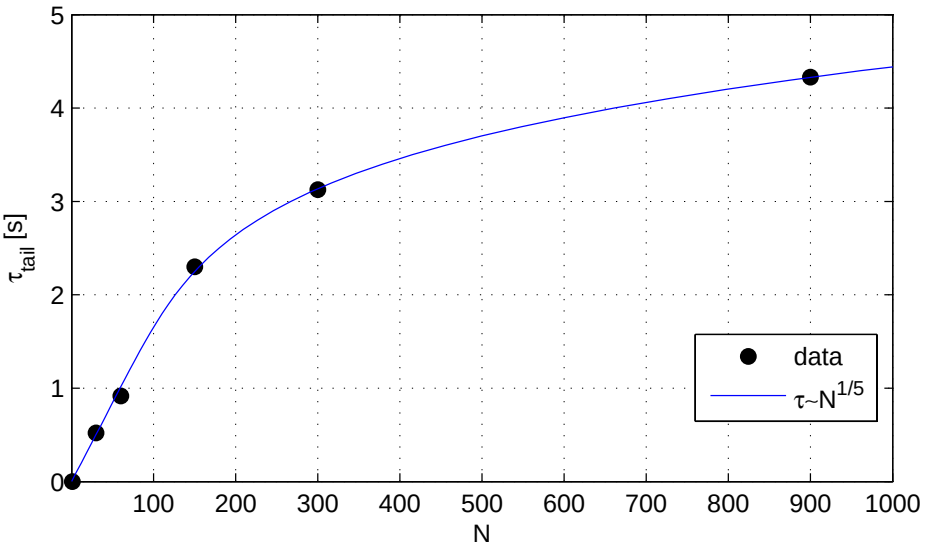


Figure 4.16: Cooling time $\tau_{tail}$ as a function of the number of $C^{5+}$ ions confined in a cylindrical Penning trap and cooled by a tank circuit of peak resistance $10^{10}$ Ω.

Although $\tau_{tail}$ is always larger than the single-particle time constant, the data clearly show that the growth of $\tau_{tail}$ with $N$ is much slower than a simple linear proportionality. Given the absence analytical predictions so far for the cooling of ion clouds, this result is of great importance: it suggests indeed that cooling of large clouds might be possible without having to face unacceptably long cooling times. The complexity of the relationship between the motion of many ions and the cooling force makes it impossible to fit the data based on a thorough physical basis. To get an indication for higher $N$ we have nevertheless made polynomial fits of the type $N = \sum_{i=0}^{M} \tau^i$ trying to minimize the norm of residuals (quadratic deviations). As expected, high-degree polynomials (fourth and fifth degree[7], for the six data points) give the best fits with $\tau_{tail} \sim N^{1/5}$ or $\sim N^{1/4}$. The extrapolation from 900 to $10^5$ particles yields a cooling constant between 12 s (for $\tau \sim N^{1/5}$) and 14.5 s (for $\tau \sim N^{1/4}$).

The severe frequency broadening seen in the spectra (see Fig. 4.12 and 4.15) suggest the investigation of resistive cooling with a broadband tank circuit. As an extreme case, we have simulated cooling with a resistance of $10^{10}$ Ω and infinite bandwidth, i.e. an ohmic resistance (see Fig. 4.17). As expected, the resistive cooling is much more efficient: the initial fast damping is immediately followed by a tail (for $t \gtrsim 0.1 \div 0.2$ s) without the appearance of the intermediate plateau either in the CM or in the total axial kinetic energy. The tails in the logarithmic plot of Fig. 4.17 show a complicated damping that cannot be fitted by a simple exponential with only one decay time. The varying slope

[7]Obviously the maximum polynomial degree $M$ is one unity lower than the number of data points. Considering $\tau_{tail} = 0$ for $N = 1$, we have six data points.

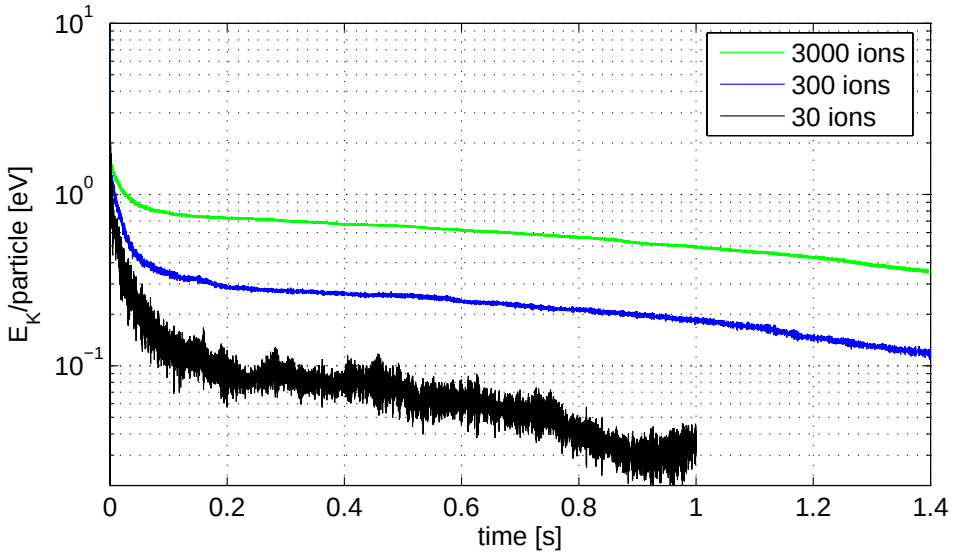


Figure 4.17: Cooling of different numbers of $C^{5+}$ ions with an ohmic resistance $R = 10^{10}$ Ω.

of the tail is not fully understood. The quasi-exponential part from 0.2 s to 1 s yields time constants of 0.65, 1.74 and 1.99 s for 30, 300 and 3000 ions, respectively. Comparing these values with those given in Table 4.1 for the RLC cooling, we notice that for high numbers of particles the cooling is faster which we interpret as more efficient damping of the frequency spectrum. Indeed the spectrogram of the image current induced by 3000 particles (Fig. 4.18) confirms the fast narrowing and shifting of the induced signals towards $\omega_z$. After about 0.1 s of cooling the tail sets in and only $\omega_z$ together with its higher harmonics is clearly visible.

As the number of ions increases, the space charge becomes significant and two effects are observed: first, a shift of $\omega_z$ from the theoretical value of 800 kHz down to 790 kHz for $N = 3000$, second, the strong axial energy cooling results in a reduced axial extension of the cloud and therefore in an increased space charge. This causes a radial expansion of the ellipsoidal cloud. A sample of $N = 3000$ with an initial length $L = 4.5$ mm and radius $R = 0.25$ mm is axially compressed to $L = 2$ mm and radially enlarged to $R = 1$ mm after 2 s of cooling.

### Scaling of cooling with the external resistance

Obviously am ohmic resistance of 10 GΩ is not achievable in reality. A further investigation addressed the dependence of the cooling process on the value of the ohmic $R$. Simulation of 30 ions showed that the decrease in $R$ affects severely the initial phase of the cooling process, as expected from the theory.

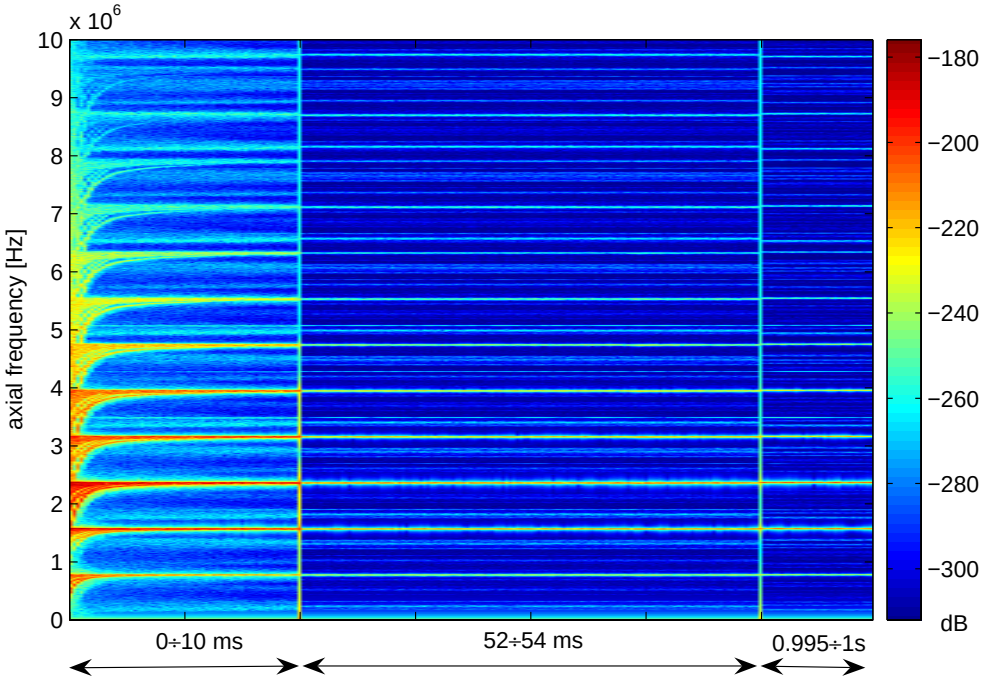


Figure 4.18: Frequency spectrum of the axial motion of 3000 $C^{5+}$ ions in a Penning trap as a function of time. The cloud is cooled by a pure resistance of $10^{10}$ Ω.

The waiting time before the tail sets in is consequently increased with lower $R$. Figure 4.19 shows clearly this feature. Notice that for $R = 10^7$ Ω the initial cooling is so long that no tail can be observed. For higher $R$ the tail becomes visible and a very weak dependence on $R$ of the tail slope itself is observed. Table 4.2 list $\tau_{tail}$ for $R = 10^8 \div 10^{10}$ showing a time constant variation of

Table 4.2: Dependence of $\tau_{tail}$ on the resistance of the dissipating circuit. Data for 30 $C^{5+}$ions and ohmic resistances. $\tau_{tail}$ is calculated over a time interval of about 1 s.

| R [Ω] | $\tau_{tail}$ [s] |
|---|---|
| $10^8$ | 0.93 |
| $10^9$ | 0.84 |
| $10^{10}$ | 0.65 |

a factor 4 over an $R$ spanning two orders of magnitude. Extrapolation to $10^7$ and $10^6$ Ω yields cooling times for the tail about 1 to 3 s and 2 to 10 s, respectively. However, as we discussed above, the slope of the tail has not a constant exponential decrease as later cooling seems to proceed faster. We can anyway draw the qualitative conclusion that a broadband tank circuit may

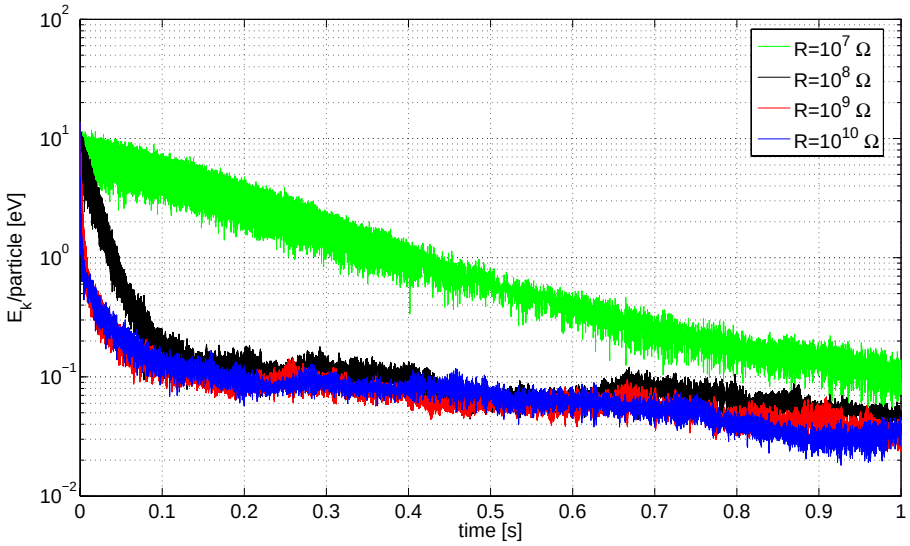


Figure 4.19: Cooling of thirty $C^{5+}$ ions in a Penning trap by use of different ohmic resistances.

have beneficial effects despite the lower peak resistance.

### Influence of contaminants

We have mentioned in Sec. 4.2.3 that an additional improvement in terms of cooling speed could come from the presence of contaminants like partially recombined ions. Ions of different m/q have different oscillation frequencies and the center of mass does not coincide anymore with the center of charge. The result is easily understandable for the case of the damping of two particles. If their initial energy and position is the same but they move in opposite directions, two equal particles have no CM motion and no induced current would be detected with a symmetric coupling. If the particles have a different m/q, their relative phase will change in time and a current is detected leading to a damping of both the CM and relative motion. The strength of the effect increases nonlinearly with the difference in the mass-to-charge ratios of the two species [Tho08]. However, a real tank circuit has a finite bandwidth and frequencies too far from the resonance are poorly cooled. This might reduce the influence of contaminants.

We simulated a sample of 300 ion with $C^{5+}$as main component and a $10 \div 20\%$ admixture of $N^{5+}$ with a mass of 13 amu. We used a different mass instead of a different charge state of C just for convenience of our PIC code since m/q is the decisive factor. Unfortunately, our results are not conclusive. This is evident from Figure 4.20 which shows a comparison between the evolution of the mean axial kinetic energy of two clouds of 300 particles cooled by an RLC

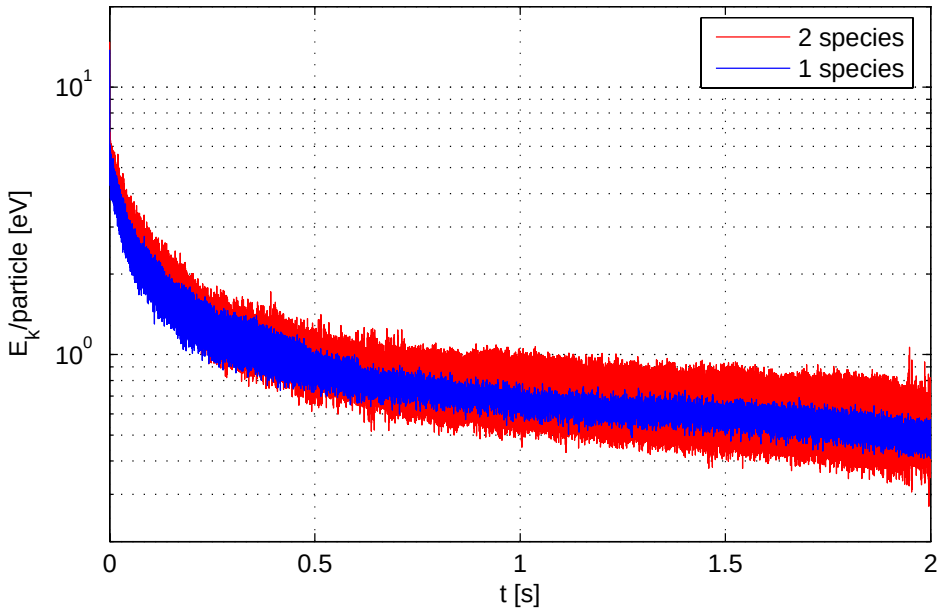


Figure 4.20: Mean kinetic energy of a pure and contaminated ion sample. The blue curve refers to 300 $C^{5+}$ and the red one to a mixture of 240 $C^{5+}$with 60 $N^{5+}$ ions.

circuit with peak resistance of $10^{10}$ Ω and same Q-factor as used throughout all our systematic investigations. The blue curve refers to 300 $C^{5+}$ ions and the red one to a mixture of 240 $C^{5+}$ with 60 $N^{5+}$ ions. The slopes are qualitatively not very different and the cooling times of the tail differ by 25% only. The energy of the mixture exhibits larger oscillations due to the periodic exchange between the degrees of freedom.

The mean kinetic energies of the two fractions in the mixture (not shown) also follow the same behaviour, in particular the mean $E_k$ of the $C^{5+}$ ions, being the dominant part, is almost identical to the energy of the mixture. The spectrum of the induced image current after two seconds of cooling[8], reproduced in Fig. 4.21, shows the additional peak at the axial frequency $\omega_z = 2\pi \cdot 762$ kHz of $N^{5+}$. Notice that the $N^{5+}$ peak is stronger since the species was cooled less effectively with its frequency falling outside of the bandwidth of the tank circuit. A further very strong peak appears at 381 kHz which we interpret as an internal mode and whose strength comes from the presence of two species. Higher harmonics of all peaks are visible.

To summarize, this simulation shows no evident benefit of the presence of contaminants. The reason is the limited bandwidth of the RLC circuit. An accurate description of the phenomenon would require extensive systematic studies to clarify the dependence of the cooling process on the difference in

[8]The initial spectrum is very blurry and practically identical to the one of 300 $C^{5+}$ shown in Fig. 4.15.

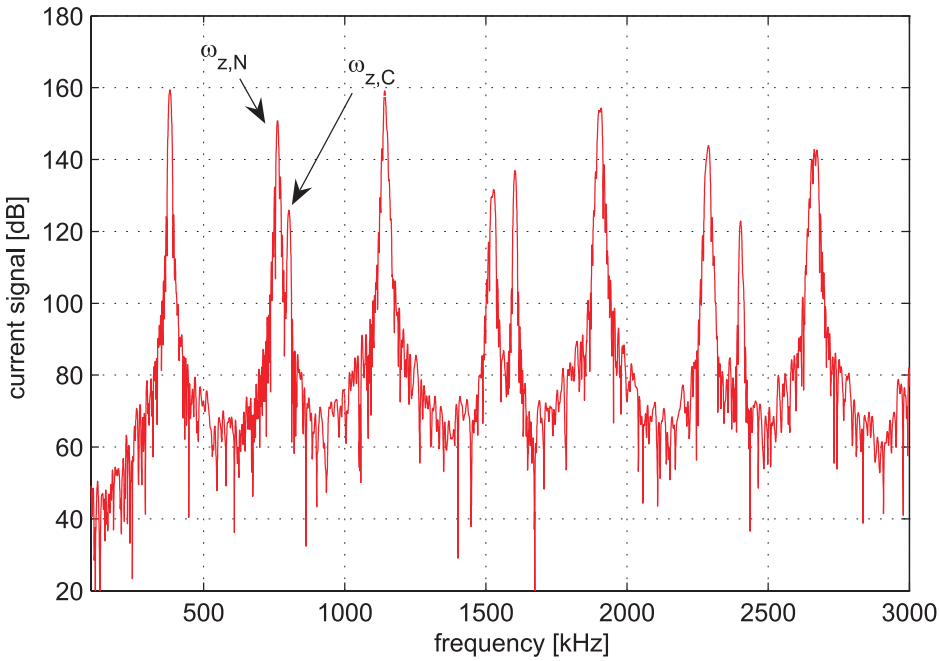


Figure 4.21: Spectrum of the image current induced by a two-species sample consisting of 240 $C^{5+}$ and 60 $N^{5+}$ ions. The axial frequencies of both $C^{5+}$ and $N^{5+}$ are visible at 803 and 762 kHz, respectively, and also their higher harmonics. A strong peak, presumably an internal mode, appears at 381 kHz.

m/q, relative fractions of the two species and bandwidth of the cooling circuit. The effects of the variation of these parameters are closely intertwined.

### Conclusions on the systematic studies

Summarizing our studies on $C^{5+}$, we have demonstrated the qualitative reproducibility of the Mainz *g-factor* experiment and interpreted the trend of the energy loss showing the tight relationship between the cooling process, the frequency spectrum and the dissipation mechanism. We have extended our investigations to the scalings of the cooling power in the low-energy tail with the number of particles and the characteristics of the cooling circuit. They have been shown to be highly nonlinear. Qualitatively, the nonlinearity is a positive feature as the increase of the cooling time is not proportional to those parameters. We can draw some preliminary conclusions. Cooling times of some tens of seconds can be expected for a cloud of $10^5$ ions if the peak resistance is in the order of $10^7$ Ω and the bandwidth of the tank circuit is broad enough to cover the axial frequency spread. Experimental investigations are nevertheless essential to find the optimal compromise.

Furthermore, we have addressed the possible influence of contaminants in

the ion sample but the additional complexity of the process demands more systematic studies to draw definitive conclusions.

### 4.3.4 Simulations on the HITRAP Cooler Trap

In this Section, simulations on HCI stored in the Cooler Trap are discussed. The purpose is to prove qualitatively and quantitatively the feasibility of resistive cooling in the Cooler Trap as well as getting information on its optimal parameters.

#### Single-particle cooling

The resistive cooling of highly charged ions in the Cooler Trap will be done in a nested trap created by five electrodes in the center of the stack. The simulations are performed in this environment and take into account $U^{92+}$ ions in a potential well of 100 V. This yields an axial frequency $\omega_z = 2\pi \cdot 383.15$ kHz. As we have seen in the previous Sections, the cooling of a single particle is well understood and reproduced by simulations. For a $U^{92+}$ ion with a kinetic energy of 10 eV and in resonance with an RLC of peak resistance $10^{10}$ $\Omega$ the cooling time constant is $\tau_s = 328$ $\mu$s or 651 $\mu$s when a symmetric or asymmetric coupling are used, respectively. The pick-up electrodes are the so-called correction electrodes, i.e. the ones adjacent to the central ring. The symmetric coupling has the advantage of doubling the detected current which consequently halves the cooling time of a single particle as well as of the CM of a larger ensemble. Symmetric coupling was therefore initially chosen for the Cooler Trap. In the following we will discuss the opportunity of this choice, whose disadvantage is the insensitivity to axially-symmetric modes when more than one particle is stored.

#### Space charge effects

Moving to $N \gg 1$, the space charge strongly influences the properties of the ion cloud determining its phase-space equilibrium configuration as well as frequency broadening and shifts. These must be accounted for in resonant detection and cooling. Table 4.3 shows the dependence of the mean axial frequency broadening versus the number of particles for a column with a radius of 1 mm at an energy of some 10 eV as it will be the end of the electron cooling phase. With increasing number of particles $N$, the distortion of the harmonic potential causes a frequency spread $\Delta\omega$ of the axial frequency $\omega_z$ of a single particle and a decreasing mean value $\overline{\omega}'_z$. These can be at least partially compensated by proper adjustment of the voltage applied to the correction electrodes adjacent to the central ring. The space charge would also be reduced if a the radius of the cloud were increased. Another possibility is the use of a lower trapping potential, resulting in a more elongated cloud. However, this conflicts with constructive issues for the inductive coil of the RLC circuit whose resonant

Table 4.3: Axial frequency shifts as a function of particle number N. The mean axial frequency, which appears shifted from the sincle-particle eigenvalue 383.15 kHz, is indicated by $\overline{\omega}'_z$. $\Delta\omega_z/\omega_z$ indicates the maximum deviation from the mean value in the distribution and $\sigma(\omega_z)$ the standard deviation..

| N | $\overline{\omega}'_z$ | $\Delta\omega_z/\omega_z$ | $\sigma(\omega_z)$ |
|---|---|---|---|
| $10^3$ | 379.72 KHz | $8.95 \cdot 10^{-3}$ | 1.77 kHz |
| $10^4$ | 374.91 KHz | $2.15 \cdot 10^{-2}$ | 6.93 kHz |
| $10^5$ | 362.05 KHz | $5.51 \cdot 10^{-2}$ | 24.70 kHz |

frequency should be lowered accordingly to match the smaller $\omega_z$. Possible solutions are presently investigated.

Another design parameter influenced by trapping potential and space charge is the choice of the pick-up electrodes. The maximum possible detection efficiency is obviously desired. The pick-ups should therefore be as close as possible to the cloud. But as it could be noticed from Fig. 4.6, for an efficient cooling, all ions should have an amplitude not larger than the axial position of the center of the pick-up electrodes. Ions outside this region are pushed further away by the feedback from the center of the potential well. In other words, the feedback has a heating instead of a cooling effect on the motion of these ions. All electrodes were designed with a length of 17 mm and the interelectrode spacing is 2 mm. Therefore, in order to use the correction electrodes as pick-ups, the axial extension of the cloud must be smaller than 38 mm. This requirement is well matched when the cloud of $U^{92+}$ ions at 10 eV is trapped by a potential of 100 V which yields a cloud length of about 20 mm. If a much lower trapping voltage is used, it might be necessary to use electrodes placed further away from the trap center as pickups.

Space charge will influence the dynamics of $10^5$ particles during the whole cooling process down to the envisaged low energy of 4 K, corresponding to $\sim$ 0.35 meV. Since a full simulation of the cooling process reproducing the real experimental conditions is prohibitive we have created and analyzed $U^{92+}$ samples at energies of 10 eV and below. Indeed, assuming a slow enough cooling process, the evolution of the cloud can be approximated by a succession of equilibrium states and as a consequence the cooling mechanism is not relevant for the properties of the ensemble. Therefore we implemented a so-called *generic cooling* or *Langevin cooling* routine in the PIC code to produce equilibrium distributions at the desired energies. This routine introduces in the equations of motion a velocity-proportional damping constant $\lambda$, a friction term, typical of buffer-gas cooling for instance. A random term $\vec{f}(t)$ is added to simulate thermal noise. We obtain a modified equation of motion

$$m\frac{\mathrm{d}\vec{v}_i}{\mathrm{d}t} = qe\left(\vec{\mathrm{E}}\left(\vec{r}_i\right) + \vec{v}_i \times \vec{\mathrm{B}}\right) - \lambda\vec{v}_i + \vec{f} \tag{4.26}$$

Table 4.4: Cloud properties at different mean energies. The length $L$, the radius $R$, the density $n$ and the axial frequency of the CM motion, all affected by the space charge, are listed as a function of the mean axial kinetic energy $E_k$.

| Mean $E_k$ [eV] | L [mm] | R [mm] | n [$cm^{-3}$] | $\omega_{z,CM}$ |
|---|---|---|---|---|
| 10 | 18 | 1 | $2.13 \cdot 10^6$ | 356.0 |
| 1 | 15 | 1 | $2.84 \cdot 10^6$ | 354.6 |
| 0.1 | 14 | 1.1 | $2.43 \cdot 10^6$ | 354.3 |
| 0.01 | 13 | 1.2 | $2.40 \cdot 10^6$ | 354.0 |

for the *i-th* particle, called Langevin equation [Cof04]. It can be demonstrated that the solution of this equation results in a Maxwell-Boltzmann equilibrium where the mean energy of the sample depends on the amplitude of the damping and of the random term. Implementing this function in the code we obtained stable ion clouds at the energies reported in Table 4.4. The length $L$ of the cloud reduces with decreasing energy although the contraction is rather limited as the space charge tends to flatten the bottom potential (as seen already in Fig. 3.15). Together with the axial length reduction we observe a slight radial expansion. The density stays roughly constant at $2.5 \cdot 10^6$ $cm^{-3}$. The table also indicates the CM axial frequency whose value is further down-shifted by space charge effects. As the mean kinetic energy reaches below 10 meV, Coulomb interactions will play an increasing role and the formation of a Coulomb crystal might take place[9] [Gil88]. The occurrence of such a phenomenon is predicted by the coupling parameter $\Gamma$ which is a ratio between the Coulomb interaction and the thermal energy of the ensemble. It is defined as

$$\Gamma = \frac{q^2}{4\pi\varepsilon_o a E} \tag{4.27}$$

where $q$ is the charge of the ions in Coulomb, $n$ the density of particles, $\varepsilon_o$ the dielectric constant, $E$ the mean energy and $a = [3/(4\pi n)]^{(1/3)}$ (*Wigner-Seitz radius*). A Coulomb crystal is observed when $\Gamma \gtrsim 178$. As Fig. 4.22 shows, the transition to a crystalline structure should appear around 1.5 meV, corresponding to 17.5 K, for a $U^{92+}$ ion density about $2.5 \cdot 10^6$ $cm^{-3}$. As far as cooling is concerned, the creation of a crystal has to be avoided, since the normal mode frequencies of the cloud will disappear to be replaced by the intrinsic vibration modes of the crystal and further energy dissipation might be more difficult.

[9]The reader should remind that PIC simulations using mean fields cannot reproduce such states since the full molecular dynamics should be calculated.

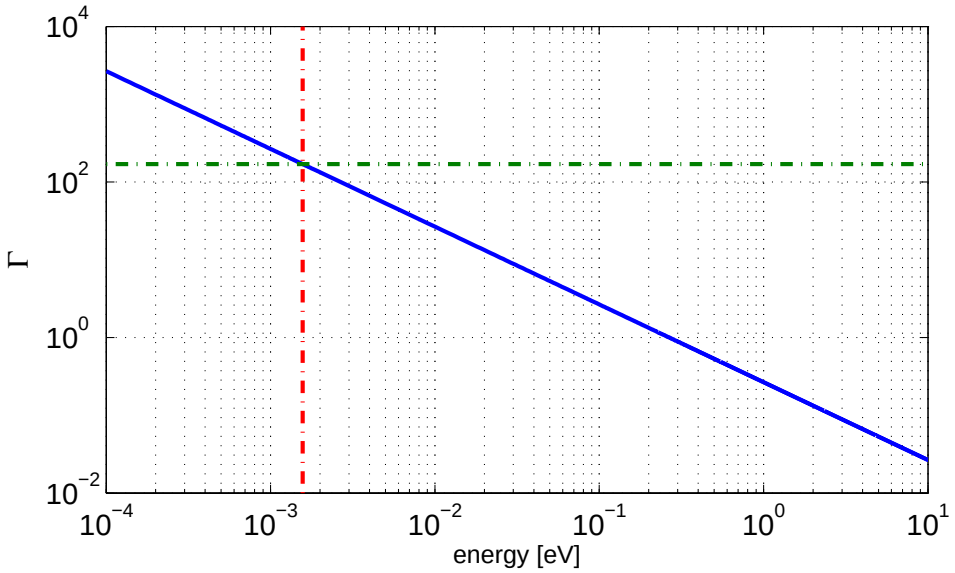


Figure 4.22: Coupling parameter Γ as a function of cloud energy for a cloud of $10^5$ $U^{92+}$ions with a density of $2.5 \cdot 10^6$ cm$^{-3}$ (blue line). The intersection between the dashed-dotted lines indicates the aproximate point of the transition to a Coulomb crystal at $\Gamma \approx 178$, $E_k \approx 1.5$ meV.

### Simulations on the cooling of a $U^{92+}$cloud

The systematic studies presented for the $C^{5+}$trap made clear that it is not straightforward to draw quantitative conclusions on the feasibility of resistive cooling under the realistic conditions. Nevertheless we have performed simulations for the case of $U^{92+}$ stored in the Cooler Trap of the HITRAP facility in order to obtain criteria for the design of this trap.

First some simulations concerned the study of ion samples with different energy contents stored essentially in the non-CM motions in order to get an indication of the damping rate of the tail. We have already shown that the CM cooling is rather fast and well explained but the critical point is the cooling of the low-energy tail. Distributions of 50 $U^{92+}$ions with no CM energy contents were created. The mean initial $E_k$ (Gaussian-distributed) was 20, 4 and 0.1 eV. The cooling was performed by a symmetrically-coupled tank circuit with a peak resistance of $10^{10}$ Ω and the same bandwidth expected for the real Cooler Trap RLC.

Figure 4.23 shows the damping of the distribution with mean $E_k = 20$ eV. In absence of CM energy to dissipate, only the slow tail appears with a $\tau_{tail}$ about 1.3 s. Simulations with lower initial mean energy gave $\tau_{tail}$ between 1.5 and 2.1 s. For comparison the cooling of a sample with mean initial $E_k$ and with identical parameters but asymmetric coupling was simulated yielding a $\tau_{tail} \approx 3.7$ s. The slower cooling is not surprising: the reason is the lower

detected current with this coupling scheme.

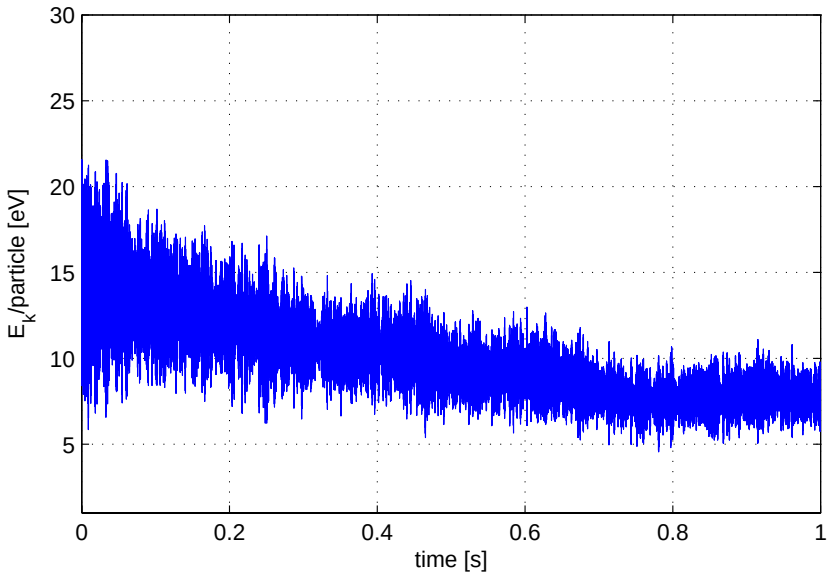


Figure 4.23: Resistive cooling of a cloud of 50 $U^{92+}$with a tank circuit of $10^{10}$ $\Omega$ peak resistance. The study was performed in absence of CM energy to observe only the cooling of the tail whose time constant is about 1.3 s.

As for $C^{5+}$, a simulation with an ohmic resistance was performed to give complementary information. A cloud of $10^5$ $U^{92+}$ions with mean kinetic energy about 10 eV and non-zero CM energy was used. Since the systematic simulations on $C^{5+}$ proved the weak dependence of $\tau_{tail}$ on R, for this simulation we chose R= $2 \cdot 10^7$ $\Omega$. This is approximately the peak value estimated for the real RLC circuit and therefore the simulation parameters are closer to what is attainable in reality. Figure 4.24 shows a trend qualitatively very similar to what observed for the Mainz *g-factor* trap. The most striking result is a $\tau_{tail} \approx 3.7$ s. If compared to the numbers obtained for the cooling of just thirty $C^{5+}$ ions with an ohmic resistance (see Table 4.2) this value is relatively modest. The frequency spectrum of the induced image current reveals again an evident initial line broadening which will result in a slower cooling when a a real RLC dissipative circuit is used. Once again the optimal compromise between a lower peak resistance and an enhanced bandwidth will require experimental tests.

### Conclusions on resistive cooling

Our studies on resistive cooling in Penning traps show that reaching the meV and sub-meV energy range is possible for the cooling of $U^{92+}$ in the HITRAP Cooler Trap, although the process is too slow to be performed in 10 s, i.e. the

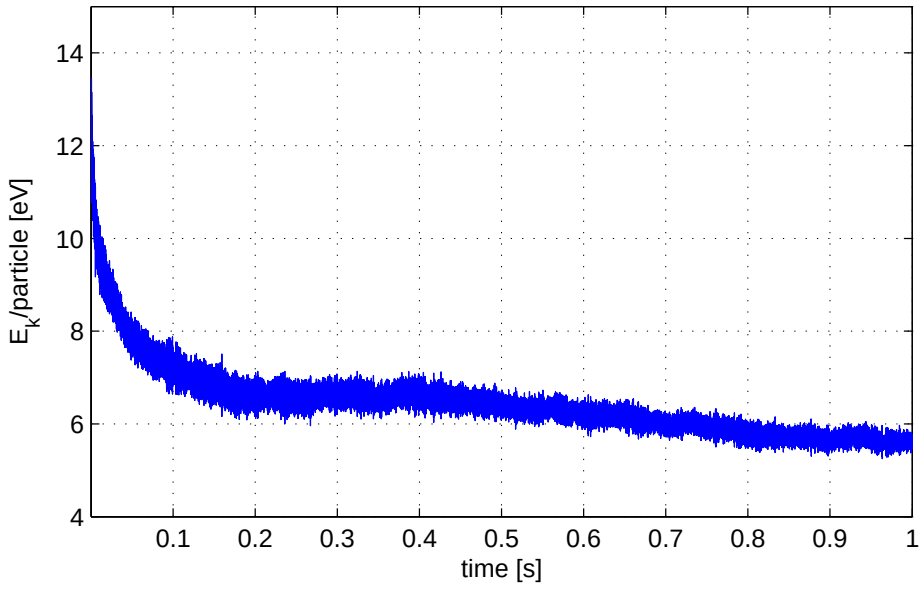


Figure 4.24: Resistive cooling of a cloud of $10^5$ $U^{92+}$. The ensemble is cooled by an ohmic resistance of $10^7$ Ω. The low-energy tail (with $\tau_{tail} \approx 3.7$ s) sets in after the first rapid loss of CM energy, which is accomplished in 0.1 s circa.

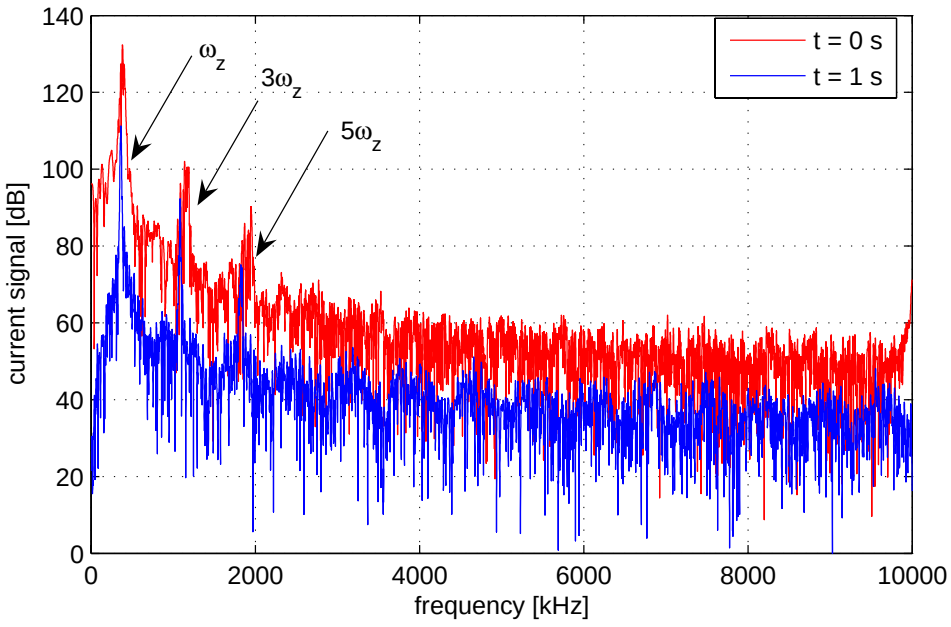


Figure 4.25: Frequency spectrum of the image current induced by a cloud of $10^5$ $U^{92+}$ during resistive cooling by a symmetrically coupled ohmic resistance. The spectrum refers to the simulated cooling process shown in Fig. 4.24.

rate at which ions can be decelerated, cooled and ejected out of the storage ring and fed to the HITRAP facility. Depending on the characteristics of the ion cloud (namely the effects of energy distribution and space charge) as well as of the cooling circuit, we can expect cooling time constants in the order of several tens of seconds. Nevertheless, the examples show that the mechanism is working and provide significant input for an optimal design. For instance, we have shown that despite the lower peak resistance a broadband RLC could be advantageous for cooling of ion clouds dominated by space charge. Similarly, we have evidenced that an asymmetric coupling is sensitive to the symmetric modes of the cloud and its enhanced diagnostics possibilities would be of great advantage even at the expense of less cooling power. If the bandwidth of the cooling circuit were large enough, one could also gain in cooling power due to the otherwise impossible cooling of symmetric modes. Nevertheless we point out that the optimization must necessarily be accompanied by experimental tests.

# Chapter 5

# Technical design and commissioning

The Cooler Trap complexity presents a series of challenging technical requirements with regards to space limitations, cryogenic conditions and mechanically as well as electrically accurate specifications. This chapter discusses those issues and presents the unique solutions that have been developed. The construction is in an advanced stage: the electrode stack is machined as well as the box for cryogenic electronics and the cabling connection system. The magnet has been set up and tested. Power supplies are available. Therefore we will also summarize the tests performed with the parts already available at GSI.

## 5.1 Trap vacuum

Storage of highly charged ions for several seconds in the trap demands very stringent ultra-high vacuum (UHV) conditions. Since it cannot be measured directly within the environment of a Penning trap, the pressure is generally estimated from the storage time, which is limited by charge exchange with the residual gas. Pressures in the order of $10^{-16}$ mbar have been reached in precision traps built and operated in Mainz [Häf03], where lifetimes of longer than a year have been achieved. This vacuum standard is more difficult to reach in the Cooler Trap. First of all the bigger volume implies a larger outgassing surface. Second and most important, in contrast with the Mainz precision traps the Cooler Trap is an open set-up communicating with the warm environment of the adjacent beamlines. For the use of the trap as cooling device, with a storage time limited to seconds or minutes, on the basis of charge-exchange cross section calculations (see Chapter 2, where the same argumentations are worked out for the Low-Energy and Vertical beamlines) we require a pressure better than $10^{-13}$ mbar at least, for which losses below $10^{-3}$ (i.e. negligible if compared to electron-ion recombination) can be expected during a complete cooling cycle. In the future, a more ambitious goal would be to store the ion sample as long as possible and to deliver it to the experiments whenever

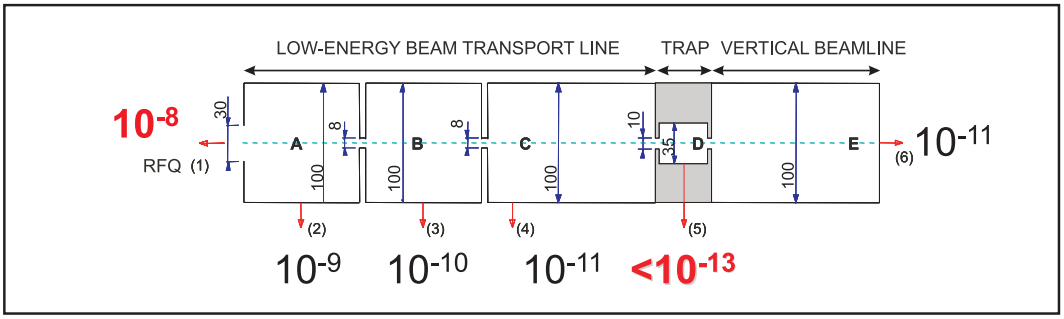


Figure 5.1: Sketch of the pressure in the HITRAP line from the exit of the RFQ to the Vertical Beamline (horizontal part only, up to the first diagnostic chamber. See also Fig. 2.15). The pressure was calculated with a concentrated parameter model based on the electrical analogy. Letters indicate the vacuum vessels. Numbers indicate the position where, setting a pumping speed and/or an outgassing source, the pressure is calculated. Given the pressures at number (1) (Radio Frequency Quadrupole) and (5) (desired value for the Cooler Trap), the pressure in each volume is determined depending on the geometry of the diaphragms. All pressures in mbar, all diameters in mm.

demanded. A better vacuum might be necessary, but in such a large set-up, accurate predictions on the sample lifetime during longer storage are hard to obtain and experimental observations will be needed.

This requirement consequently affects the volumes close to the trap. As we have discussed in Sec. 2.4.3, charge exchange calculations have shown that a pressure $\leq 10^{-10}$ mbar is also necessary in the long Vertical Beamline to preserve the highly charged sample. Nevertheless the RFQ will operate in a pressure regime not better than some $10^{-8}$, hence multiple differential pumping stages will be necessary on the upstream side. In addition to the diaphragms represented by endcap electrodes EC1 and EC2, two barriers are located in the LEBT line (see Sec. 2.4.1). The results of a calculation based on the formal analogy between hydraulic and electrical circuits [Ber92, Laf98] are illustrated in Fig. 5.1. In the electrical analogy, the set of pipes and pumps is replaced by a concentrated parameter model where each vacuum volume is represented by a conductor with a specific resistance, gas flows (i.e. outgassing and pumps) are equal to currents and pressures to potentials. Given the pressure of in the RFQ and the desired vacuum in the trap, it is possible to determine the necessary pressure in all vessels and the pumping speed of the pumps. The diameter of the diaphragms can therefore be optimized. The calculation was performed taking into account flow of different species, as water, air and hydrogen and realistic pumping elements (see next paragraph). The sketch shows the pressure achieved in the different sections from the RFQ to the Cooler Trap and demonstrates that it is possible to match the required $10^{-13}$ mbar.

The attainable pumping speed is defined by the maximum conductance of

the beamline vessels, whose diameter is 150 mm at most. In these conditions, the speed cannot exceed 300 l/s. Therefore turbopumps with this pumping speed will be placed at the ports located on the flanges at each side of the magnet and another one is installed at the beginning of the LEBT line. Two ion-getter devices are mounted on the two vessels that house the LEBT Einzel lenses (see also 2.4.1). The cryogenic temperature in the trap environment is also instrumental in achieving a low partial pressure for most of the residual gas species, as the described calculations also confirm. The most critical species are those with light mass ($H_2$, He), for which the partial pressures are highest.

## 5.2 Mechanical design

### 5.2.1 The superconducting magnet

Conventional or permanent magnets cannot provide the 6-Tesla field strength required to confine highly charged ions, therefore the Cooler Trap is enclosed within a custom-built superconducting machine purchased from the company CRYOGENIC. The magnet has a cold bore and is built using cryogen-free technology, i.e. the inner bore of the magnet is at cryogenic temperature and there is no flow of liquid helium around the superconducting coils. Refrigeration of a *cold head* occurs by expansion of high-pressure He in a Gifford-McMahon cycle [Gif65], driven by a SUMITOMO compressor with a specified capacity $\dot{Q}$=1.5 W at 4.2 K. Thermal contact of the cold head with the internal structure of the magnet ensures efficient removal of the heat load. Pre-cooling by flow of liquid $N_2$ in a dedicated loop is exploited to speed up the cool-down phase. Temperature-wise, the volume is divided in two stages. In the first one the transition from room temperature to $30 \div 90$ K (depending on the heat load) is accomplished, while the inner part, separated by a metallic shield, reaches the lowest temperature, i.e. about 4 K. An actual heat load of 0.65 W could be inferred from the second-stage temperature of 3.5 K reached in the tests at CRYOGENIC [Mit08]. The trap stack is inserted in the inner bore (150 mm diameter) of the magnet, which is adjustable with respect to the magnetic field axis (see Fig. 5.2 and 5.3). Due to the thermal contact with the cold bore, the trap is maintained at low temperature without any separate cooling system.

The setup is passively shielded by a massive iron structure with a length of 1635 mm and outer diameter of 935 mm, so that the magnetic field is suppressed outside the region of interest. Figure 5.4a shows that at the axial distance of 1 m from the trap center the field on the axis is $\approx$ 0.6 mT. The homogeneity of the magnetic field, which we can estimate from $\Delta B/B$ with $\Delta B$ deviation from the mean value of $B$, is crucial for stable confinement and for exploiting resonant manipulation of the ions' eigenfrequencies. We took as a reference a similar setup, i.e. the MUSASHI-ASACUSA antiproton trap at CERN. In their case a maximum inhomogeneity $\Delta B/B \leq \pm 5 \cdot 10^{-3}$

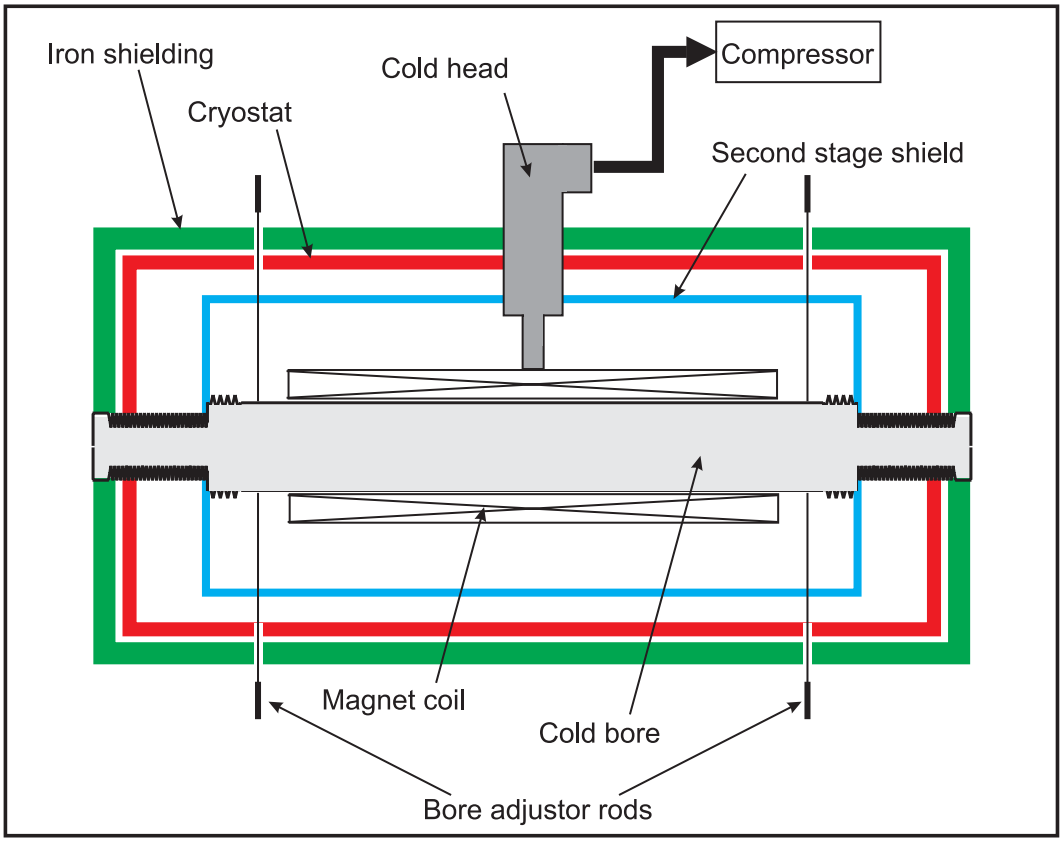


Figure 5.2: Schematics of the magnet. The magnet vacuum container (cryostat) is enclosed within an iron shield and cooled by a helium compressor via thermal contact with the cold head. The second-stage shield separates the volume where the transition from room temperature to $30 \div 90$ K is achieved (first stage) from the inner region where the magnet windings are placed and a temperature of about 4 K is reached (second stage). The trap (not depicted) is inserted in the magnet inner bore, which is also cold due to thermal contact. Adjustor rods are used to align the bore with respect to the magnetic field.

over a region extending for 10 mm in diameter and 1100 mm in length was specified and successful operation was demonstrated [Kur05]. As a conservative constraint we required a maximum inhomogeneity $\Delta B/B \leq \pm 10^{-3}$ over a volume of 10 mm in diameter and 400 mm in length, i.e. for a radial extension equal to the maximum injection diameter and along the whole trap axis. This guarantees a maximum B-field dependent frequency shift $\Delta\omega/\omega \leq \pm 10^{-3}$, i.e. within the bandwidth of the resonant detection circuits.

Two cycles comprising cool-down of the system (excluding the trap), magnet energization to nominal value and warm-up were successfully performed in the ReInjection Tunnel, thus demonstrating reproducible and stable operation. Using liquid $N_2$ pre-cooling for about 6 hours, the system was brought to stationary conditions, i.e. to a temperature of the second stage around 4

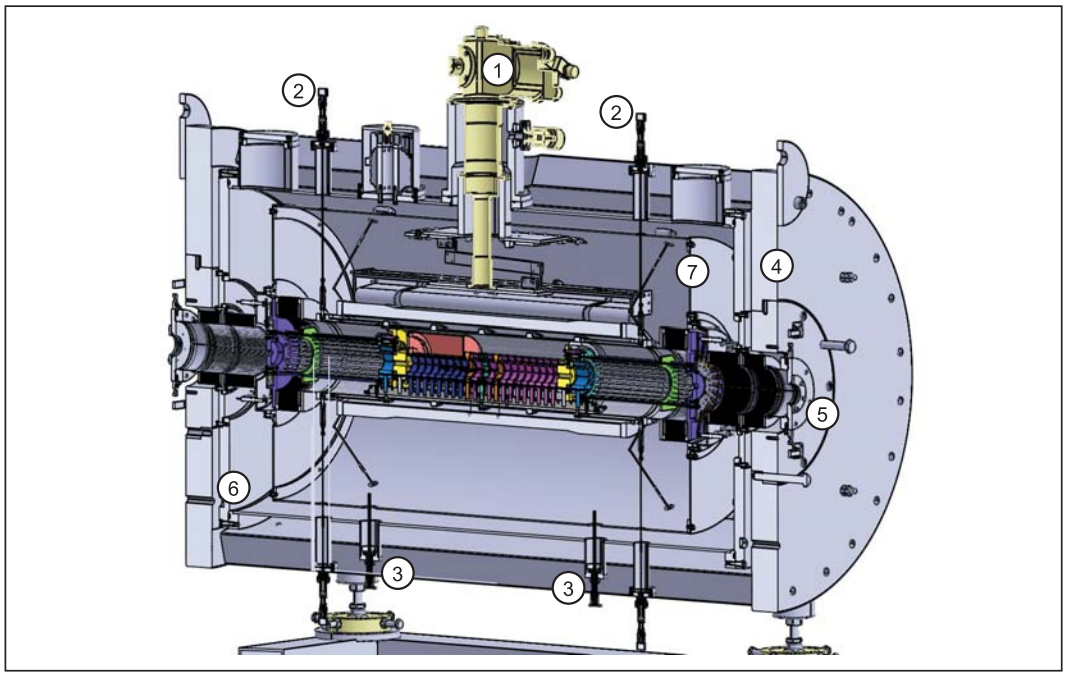


Figure 5.3: Three dimensional view of the magnet and trap system (longitudinal cut). 1) Cold head. 2) Adjustment rods for alignment of the cold bore with the magnetic field. 3) Ports for liquid $N_2$ pre-flushing. 4) Iron shield. 5) Removable lid for electrode stack insertion (on both sides). 6) Vacuum container (cryostat). 7) Second-stage shield.

K, in about two and half days (see Fig. 5.5). Energization follows this scheme (deenergization follows a qualitatively similar scheme in reverse order):

- Heating the superconducting switch, the electrical circuit of the magnet coils is opened and coupled to the power supply;
- Ramp-up to the nominal current (112.2 A, corresponding to 6 T) begins (*transient mode*). Since the heat load increases with the circulating current, the ramp rate is decreased stepwise according to Table 5.1;

Table 5.1: Ramp rate of the magnet.

| Field range [B] | Current range [A] | Ramp rate [A/s] |
|---|---|---|
| $0 \div 3$ | $0 \div 56.1$ | 0.0213 |
| $3 \div 5$ | $56.1 \div 93.5$ | 0.016 |
| $5 \div 6$ | $93.5 \div 112.2$ | 0.0104 |

- The switch heater is turned off so that the switch is brought into the superconducting regime and the circuit is closed. Therefore the magnet

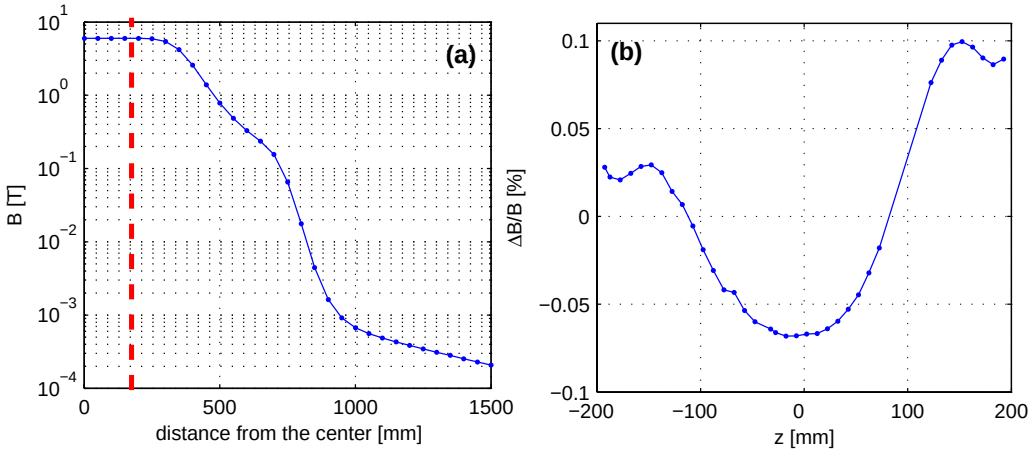


Figure 5.4: Magnetic field and inhomogeneity on the longitudinal axis. (a) The calculated $B_z$ is plotted as a function of the axial distance from the center. Outside the trap region (i.e. on the right of the dashed red line at 200 mm from the center) the field rapidly decays to some Gauss. (b) The field inhomogeneity along the axis, measured over the whole trap length, is plotted. The maximum deviation $\Delta B$ from the mean value $B$ reaches $\Delta B/B = 0.17\%$. Data points are missing in a region where the gradient is too high for the used NMR probe.

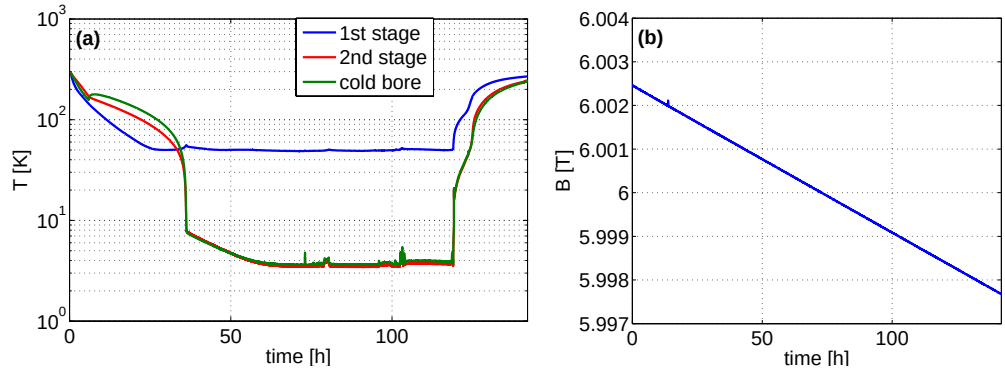


Figure 5.5: Magnet cool-down and field stability. On the left, the temperatures of first stage, second stage and of the cold bore are plotted versus time. A final temperature of $\sim$ 4 K is reached within less than three days. On the right, the magnetic field strength measured for six days after cool-down and energization. The field is stable: the decrease ($3.78 \cdot 10^{-5}$ T/h) is the expected field decay.

is in the so-called *persistent mode*, i.e. it is electrically disconnected from the power supply and the current flows without ohmic losses in the closed loop. The power supply is maintained at the final current value for safe and quick reconnection at the moment of deenergization.

The stability of the field was measured. The field was stable over the whole span of a week, with a linear decay of $3.78 \cdot 10^{-5}$ T/h (*flux creep*). This is the expected value confirmed by the manufacturer and it is supposed to reduce with time. A measurement of the field homogeneity with a NMR probe was also performed. The inhomogeneity goes up to a maximum of $1.7 \cdot 10^{-3}$ (see Fig. 5.4b), that is well within the requirements. The magnet setup includes an additional layer of shim coils for adjustment of the magnetic field. The homogeneity could be possibly improved by a proper setting of the current in the shims, which were not used in the described tests.

### 5.2.2 The electrode stack

As discussed before, the physics of the Cooler Trap set demanding constraints on its design, namely a length of 400 mm to catch the ion bunch (see Sec. 3.3). On the other hand, a magnetic field of 6 T with the specified high homogeneity over such an extended region is a significant expense. To contain the financial cost, one has to set a limit on the diameter of the cold bore. The compromise choice of a 150-mm diameter bore, together with a length of 861 mm, puts additional compelling demands on the technical design of the electrode stack, which must be mounted outside and inserted as a whole in the bore. The main issues can be summarized as follows:

- the abovementioned radial space limitations, namely the outer diameter of 150 mm and the necessity to save space for the cryogenic electronics;
- manual accessibility (insertion and removal) within the narrow and long magnet bore;
- electrical as well as vacuum insulation (implying also a careful choice of materials) simultaneously with good thermal conductivity in order to get fast and efficient cooling to 4 K);
- extreme mechanical accuracy to avoid discharges or false contacts as well as to achieve by default a good alignment.

The technical solution we have developed is based on the fundamental idea of coupling each electrode to a stack holder via an insulating rod (see Fig. 5.6). A groove is milled in a structure which is screwed into the bore itself. The insertion and removal of the stack is perfomed by sliding it along this groove. Figure 5.6 offers a clear image of the mounting scheme. Each rod can be inserted independently in a groove carved in the holder. The elements are

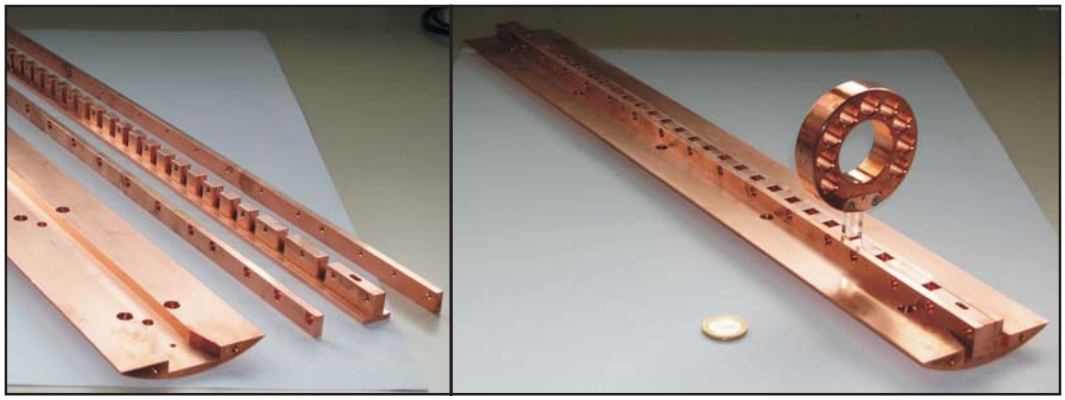

Figure 5.6: Electrode stack holder. The sapphire stands connected to the electrodes are inserted in the holding bar and firmly clipped by screwing in the lateral plates. The holder is then slided along the groove of the counterpart, which is permanently screwed into the cold bore.

then clipped together by screwing the lateral plates on each side of the holder. The assembly is then slided along the longitudinal groove of its counterpart, which is permanently attached to the cold bore (not shown in the picture). A technical drawing of the complete assembly is portrayed in Fig. 5.7.

The coupling of the rod with the electrode is done in a similar way: the rod is inserted in a groove of the electrode (see Fig. 5.8) and clipped on both sides by plates screwed in the electrode body. All electrodes and the stack holder have been machined in the GSI workshop. In order to get the lowest possible magnetic susceptibility, they are made of oxygen-free high conductivity (OFHC) copper. They will be gold-plated to prevent oxidation. As insulating material we have chosen sapphire, i.e. $Al_2O_3$ in crystalline form and 99.999% pure, which guarantees a good thermal conductivity while being an electrical insulator (see Table 5.3). The sapphire rods' elongated shape (36x8x8 mm) leaves a large amount of free space around the electrodes. The rather large outer diameter of the electrodes (69 mm) was chosen for providing a good coupling with the sapphire rod, which both secures good thermal contact and minimizes misalignments. The effect is enhanced at low temperature, where thermal shrinking significantly affects the copper electrode but not the sapphire stand. Repeated immersions of a prototype in liquid $N_2$ have shown that the connection is stable and cool-down/warm-up cycling does not create deformation or loosening problems. Holes are milled in the electrode body to reduce the weight.

Coupling regions must satisfy narrower tolerances than the usual $\pm 0.1$ mm to ensure good thermal contact. The same holds as far as surface polishing, edge smoothening and cleanliness are concerned. All tolerances regarding the coupling regions and the surfaces of facing electrodes are set to 10 $\mu$m. We have mentioned before (see 3.3.1) that electric field distortions due to misalignments

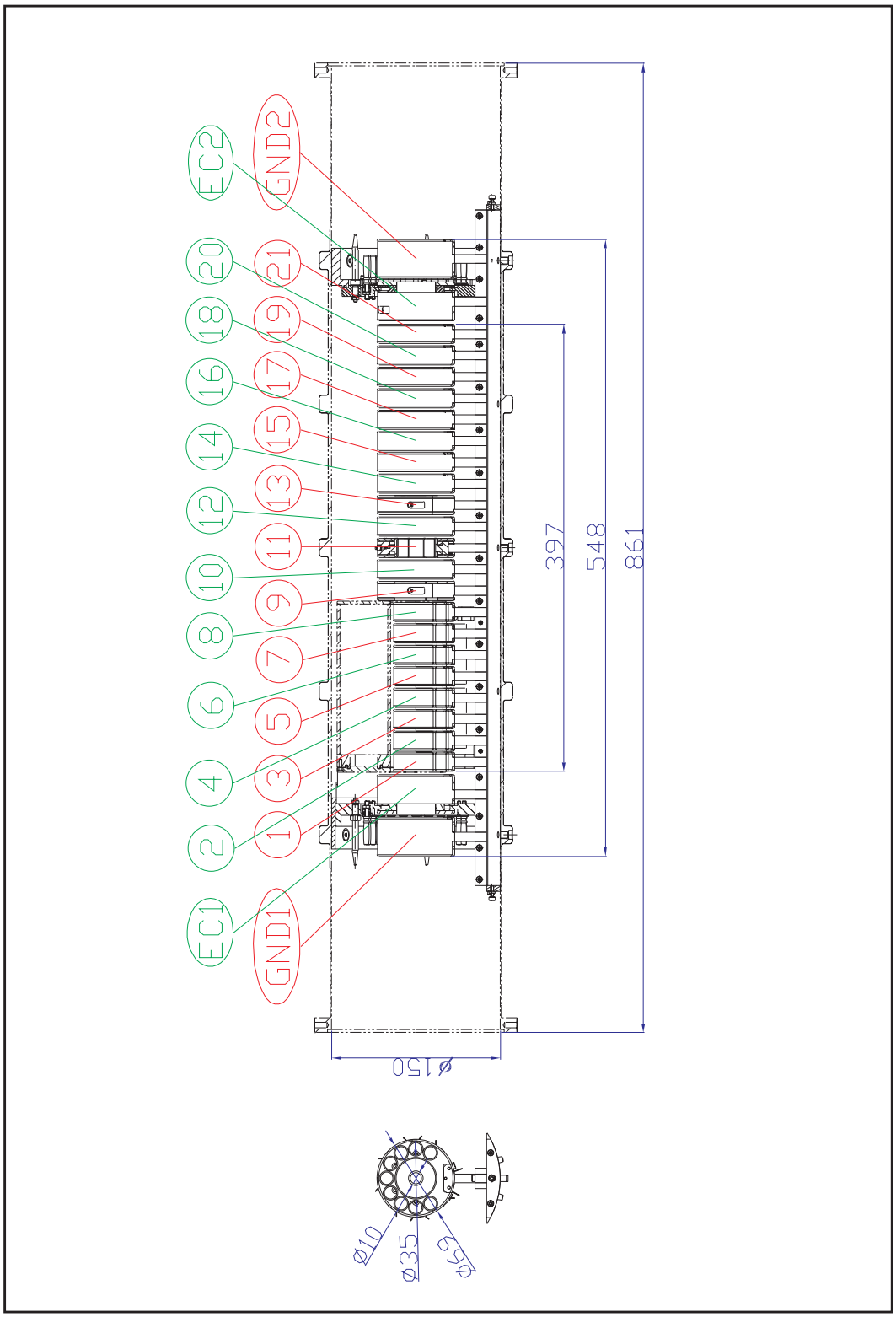


Figure 5.7: Technical drawing of the trap stack. The inner electrodes ($1 \div 21$) have the same length (17 mm) and inner radius (17.5 mm). The outer radius of electrodes $1 \div 8$ is reduced to make space for the electronics box. Endcaps (EC1, EC2) have an extended length and smaller diameter for effective trapping and differential pumping. Vacuum caps (see Fig. 5.10 and Table 5.2) screwed on the outer face of EC1, EC2 act as differential pumping barriers. Grounded outer electrodes (GND1, GND2) define the electric field outside the trap. All dimensions in mm.

Table 5.2: Description of the Cooler Trap electrodes. For each electrode type, the number as of Fig. 5.7 and 5.17 is reported. The geometry is given. IR stands for inner radius, OR for outer radius, L for length. The abbreviation used in the text for each element is explained together with a brief description on the purpose of the item and the reference to the corresponding photograph.

| Type | Electrode # | Abbreviation | Dimensions | Purpose | Figure |
|---|---|---|---|---|---|
| 1 | $10, 12, 14 \div 21$ | IE | IR=17.5 mm<br>OR=34.5 mm<br>L=17 mm | inner electrode | 5.8 |
| 2 | GND1, GND2 | GND | IR=17.5 mm<br>OR=34.5 mm<br>L=34.75 mm | (grounded) outer electrode defining the electric field outside the trap | 5.9 |
| 3 | $1 \div 8$ | MIE | IR=17.5 mm<br>OR=20 mm<br>L=17 mm | modified inner electrode with reduced OR for housing of electronics box | 5.8 |
| 4 | 11 | IE8 | IR=17.5 mm<br>OR=34.5 mm<br>L=17 mm | eightfold-split inner electrode for azimuthal detection and excitation, rotating wall compression | 5.11 |
| 5 | $9, 13$ | IE2 | IR=17.5 mm<br>OR=34.5 mm<br>L=17 mm | twofold-split inner electrode for azimuthal detection, resonant coupling of axial and radial motions | 5.12 |
| 6 | EC1, EC2 | EC | IR=5 mm<br>OR=34.5 mm<br>L=17 mm | endcap electrode for bunch trapping | 5.9 |
| – | – | VC | OR=76 mm (VC1)<br>OR=66 mm (VC2) | vacuum cap, screwed to EC1, EC2 (electrically insulated) | 5.8 |

Table 5.3: Thermal conductivity of various construction materials (from [Mar08, Huk08]). Electrical insulators are marked with an asterisk. Notice that sapphire (crystalline $Al_2O_3$ 99.999% pure), although electrically insulating, has a relatively high thermal conductivity, also compared to common $Al_2O_3$. Data are given at room temperature since the conductivity is in many cases unknown at cryogenic temperature.

| Material | Thermal conductivity [W/m/K] |
|---|---|
| OFHC copper | 391 |
| stainless steel | 16 |
| glass* | 0.93 |
| plastics* | $< 1$ |
| macerite* | 1.7 |
| $Al_2O_3$* (99.5% pure) | $25 \div 30$ |
| sapphire* | 41.9 |

are very limited. Nevertheless high-precision machining is necessary in order to avoid possible false contacts or interelectrode discharges that could occur due to the high voltages (some 100 V to some kV) applied to the trap elements. Studies and observations on discharge voltages inside a UHV region indicate that 10 kV/mm at the cathode and 5 kV/mm at the anode are tolerated [Lat95, Moo02]. With a conservative choice, we set a distance of 2 mm between inner electrodes and of 3 mm at EC and GND electrodes, where potentials as high as some kV are achieved: with a trapping voltage of $\sim 18$ kV against a bottom potential of $\sim 11$ kV, the resulting gradient will be $\sim 2.5$ kV/mm.

Construction-wise, electrodes are of six different types. Table 5.2 summarizes their main features and establishes the conventional names and abbreviations we will use in the following. In brief, all electrodes apart from the endcaps have an inner radius of 17.5 mm. The endcaps (see Fig. 5.9 left) have a reduced radius of 5 mm which together with the bigger length with respect to the inner electrodes is essential in reinforcing the electric field in order to catch the incoming ion bunch and also acts as a differential pumping barrier. On their outer face so-called vacuum caps (see Fig. 5.10) are mounted. These OFHC copper lids create a chicane at the inner surface of the bore and represent therefore another vacuum barrier (see Fig. 5.14). The two caps are not symmetric since the insertion of the stack can take place only along the beam direction. Special feedthroughs in the caps allow the passage of electrical wires out of the trap maintaining the vacuum separation. Outside the EC, a further electrode of the same length but normal diameter is placed to define the field outside the trap (see Fig. 5.9 right).

Some of the inner electrodes have a special design. Eight of them (see Fig. 5.8) have a reduced outer radius to allow space for the electronics box which houses the cryogenic electronics. If more space were needed, inner elec-

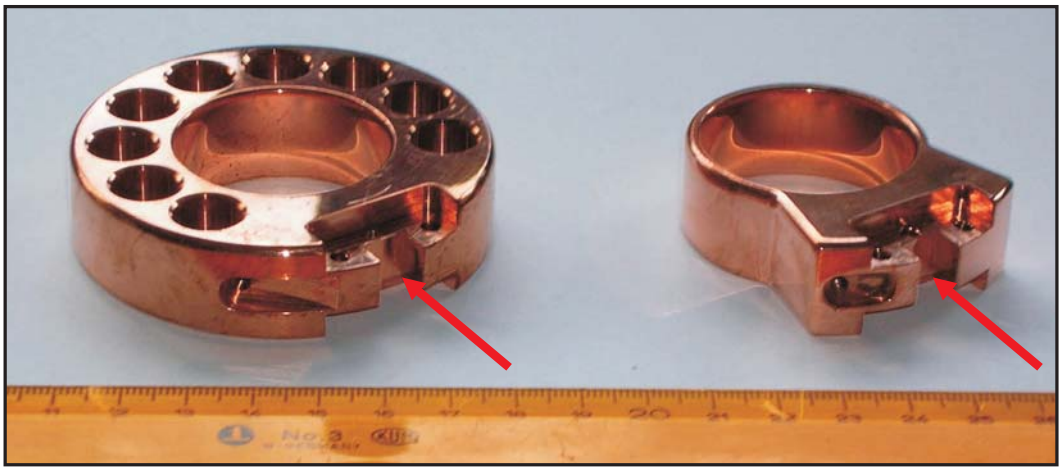

Figure 5.8: Electrodes of type 1 (left) and type 3 (right). Both are inner electrodes with length 17 mm and diameter 35 mm. The smaller outer radius of type 3 is required to house the electronics box in the cold bore. The arrows indicate the groove where the sapphire rod is inserted.

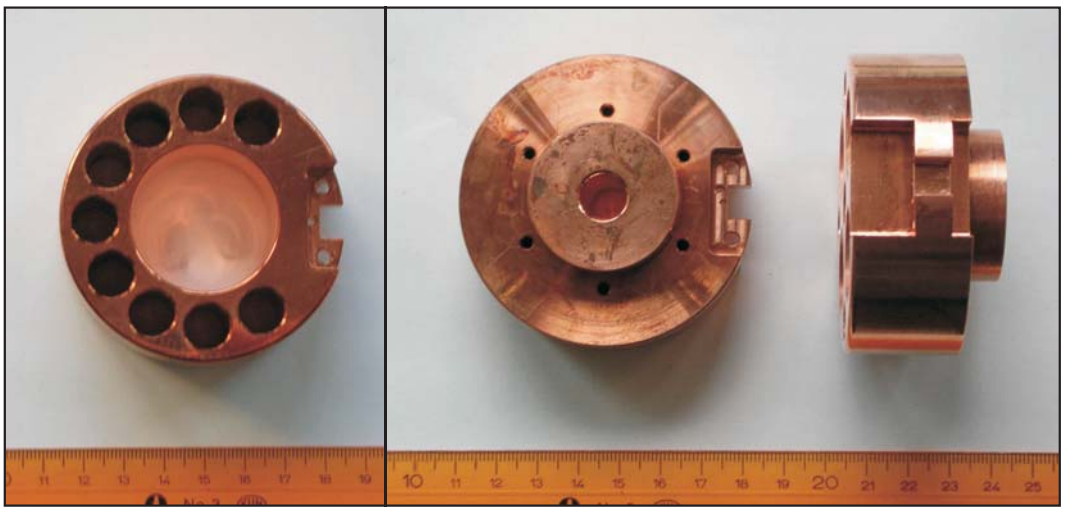

Figure 5.9: Electrodes of type 2 and 6. On the left, electrode type 2 (GND1, GND2 in Fig. 5.7) which define the field outside the trap. On the right, the endcaps EC1, EC2 (type 6). The vacuum caps (see Fig. 5.10) are screwed on the visible face. The small inner diameter (10 mm) reinforces the trapping field and acts as a vacuum barrier.

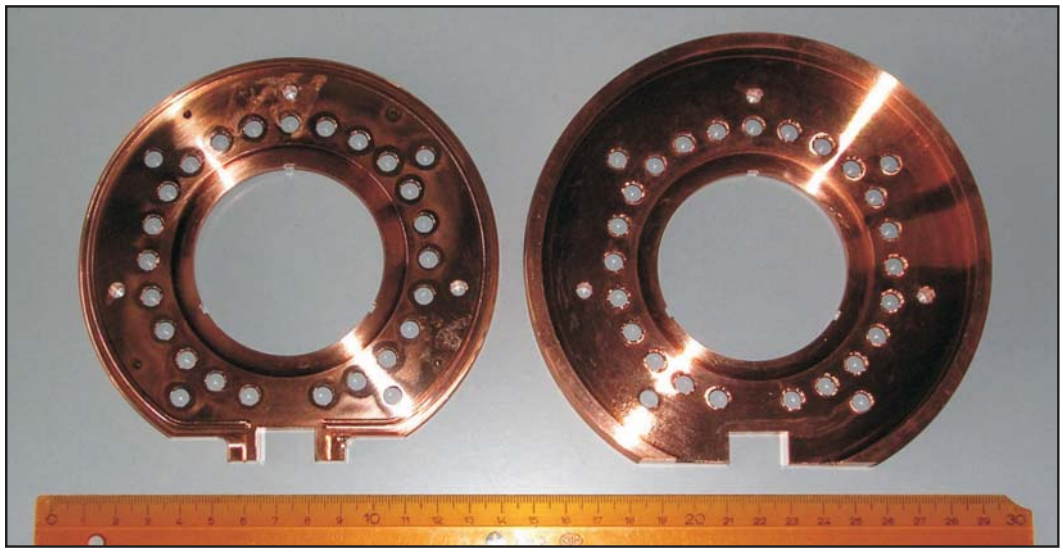

Figure 5.10: Vacuum caps. The vacuum caps are screwed on the outermost face of the endcaps and act as differential pumping barriers. Feedthroughs for all electrical connections of the trap will be installed in the holes.

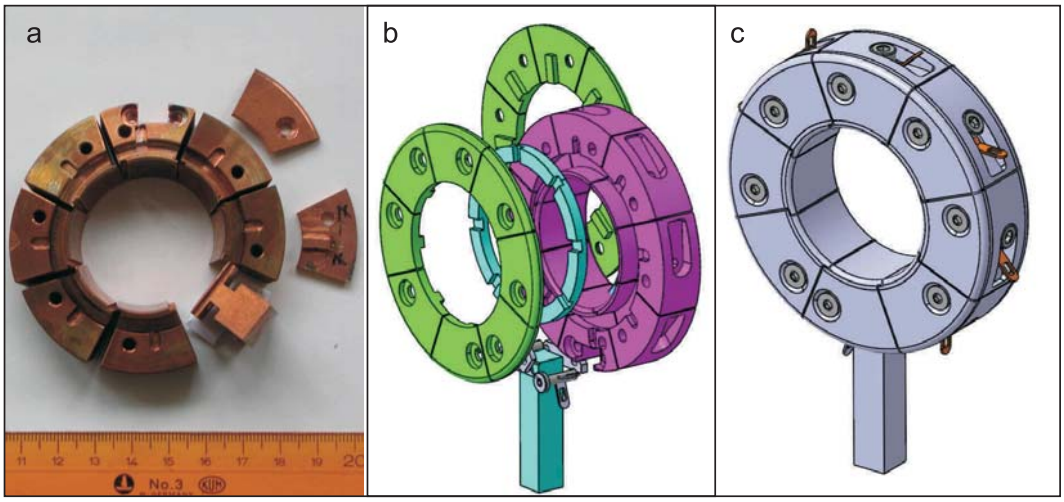


Figure 5.11: Electrode type 4. (a) Photograph of the sectors of the eigthfold-split electrode with two of the covering plates. (b) and (c) Exploded and assembled view of the electrode. Sapphire rod and ring are depicted in light blue in (b). In all views, notice the grooves on the sectors and on the sapphire ring, with the corresponding counterpart on the plates for correct positioning. Azimuthal play and ensuing contact is thus hindered.

Figure 5.12: Electrode type 5. Electrodes #10 and #12 are twofold-split for detection and excitation of ion motions in the radial plane. In the figure, an example of the assembly with a sector and the two sapphire rings blocked and held in position by the cover plate.

trodes of Type 1 could be replaced with these. The central electrode (see Fig. 5.11) is eightfold-split to enable ion manipulation (rotating wall compression or radial resonant excitation). Similarly, two other elements (see Fig. 5.12) are twofold-split to allow coupling of the axial and radial motion during the cooling phase. The sectors of these electrodes are held together by a sandwich technique depicted in Fig. 5.11. A sapphire ring is inserted in a groove on each side of the sectored inner part. Covering plates are screwed on top, locking the rings inside. Both the sapphire rings and the sectors have a groove which fits to a counterpart on the inner face of the covering plates, so that radial centering is guaranteed and no false contact can occur due to azimuthal movements. Since the sapphire elements should not be visible to the ion cloud, the radial cut of each sector ends with a chicane close to the electrode inner surface.

### 5.2.3 Electronics box and connection system

The total number of AC and DC voltages to be fed to the 25 electrodes (some of them being split) sums up to 50. Therefore 50 wires must reach out of the trap enclosure and the magnet shield. Due to the technical complexity of the set-up, this is done in several steps which are well shown in Fig. 5.13 and 5.14. 50 kapton-insulated wires depart from the electrodes and are fed into the so-called *electronics box*, a horsehoe-shaped OFHC copper box surrounding part of the electrode stack and attached to the electrode holder (see Fig. 5.15). The box must be set inside the cold environment because it houses the cryogenic electronics, which gain in signal-to-noise ratio by the reduced Johnson thermal noise at low temperature (see also next Section). In addition to this, since the Q-factor of the coil for resistive cooling is affected by the parasitic capacitance of the cables, the electronics box must be placed as close as possible to the pick-up electrodes used for resonant detection and cooling.

The kapton-insulated wires getting out of the electronics box are connected

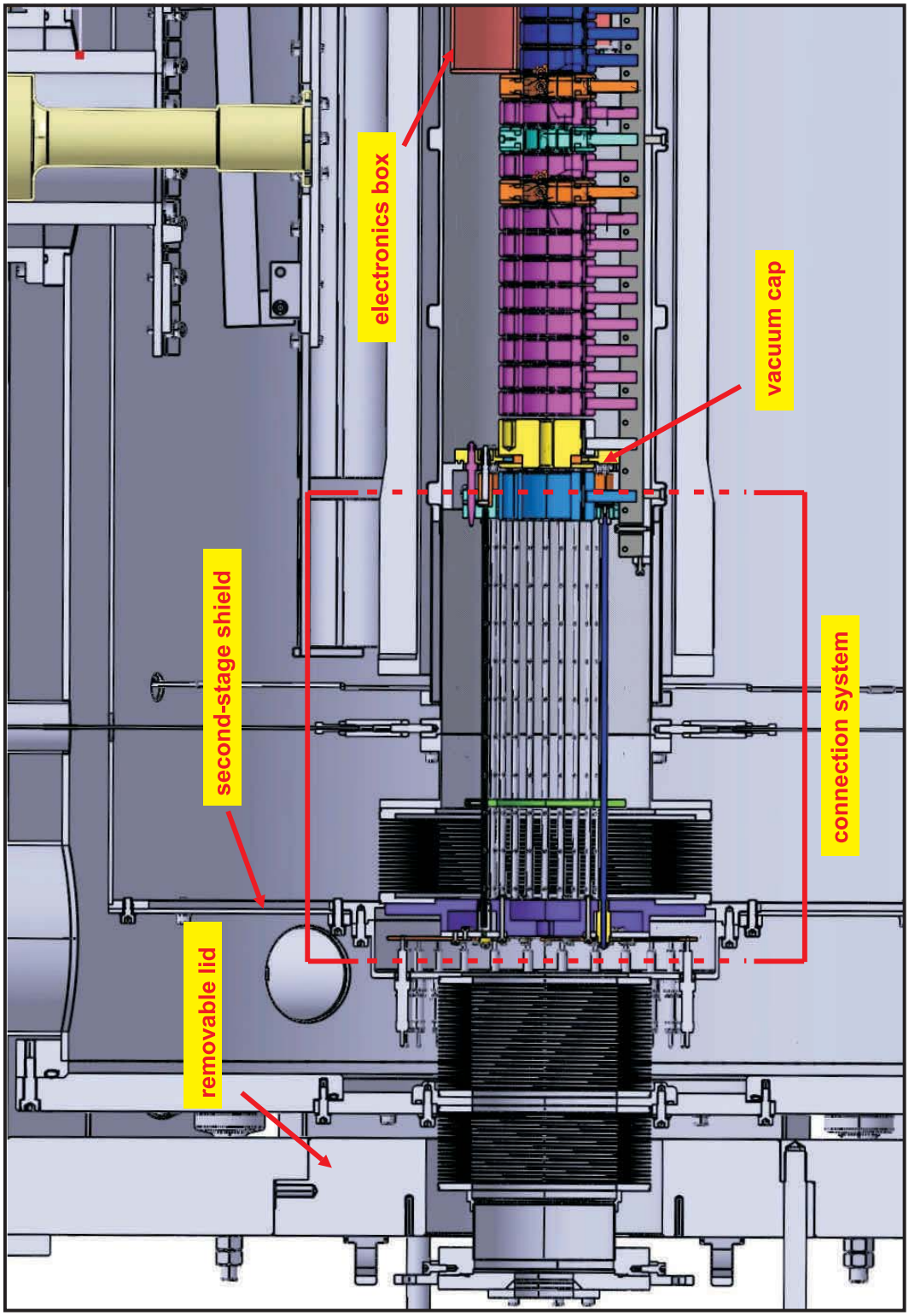


Figure 5.13: Drawing of the trap electrical connection system. Electrical wires (not depicted) connect the electrodes to the electronics box. Wires are drawn to the feedthroughs on the vacuum caps and the connection system leads them to the feedthroughs on the second-stage shield. Details are shown in Fig. 5.14.

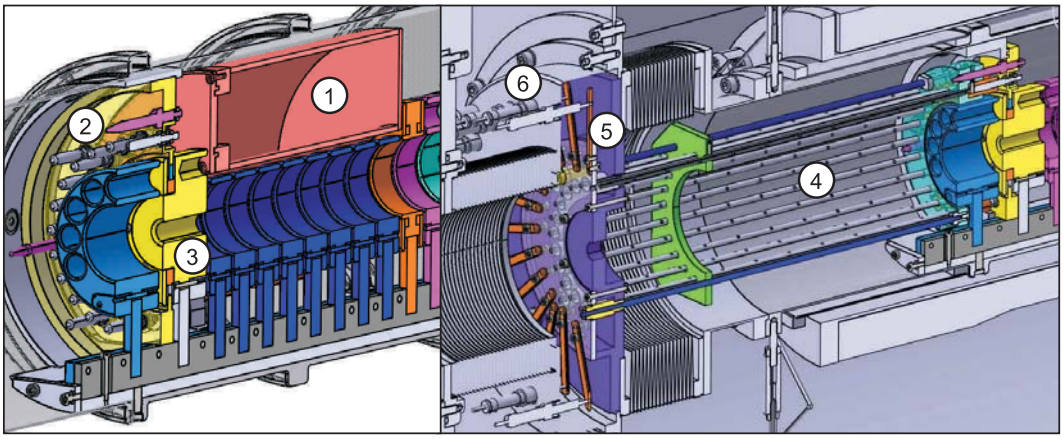


Figure 5.14: Detailed views of the trap electrical connection system. On the left, electrical wires (not depicted) connect the electronics box (1) to the feedthroughs placed in the trap vacuum cap (2). The latter are mounted on the outer face of the endcap (3). On the right, the connection system is shown. This is plugged into the feedthroughs at the vacuum caps. Wires are carried in the ceramic tubes (4) up to the radial connector strips (5), which are in contact with the feedthroughs (6) at the second stage shield. From there the connections are brought outside the magnet enclosure.

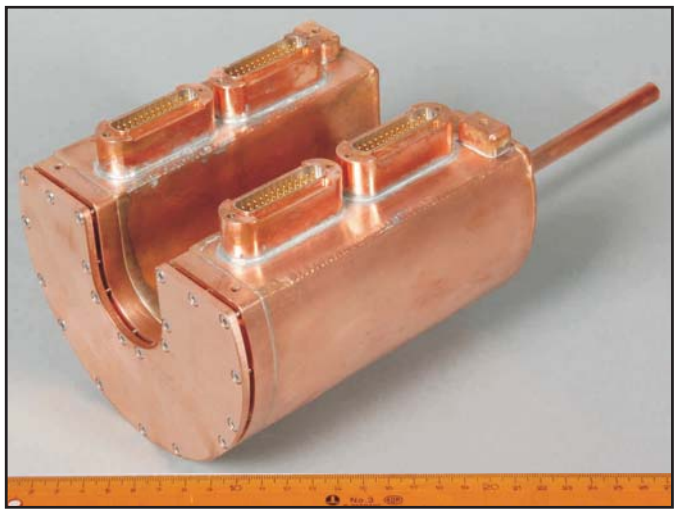

Figure 5.15: Photograph of the electronics box. The four multipin feedthroughs, providing 25 connections each, are visible.

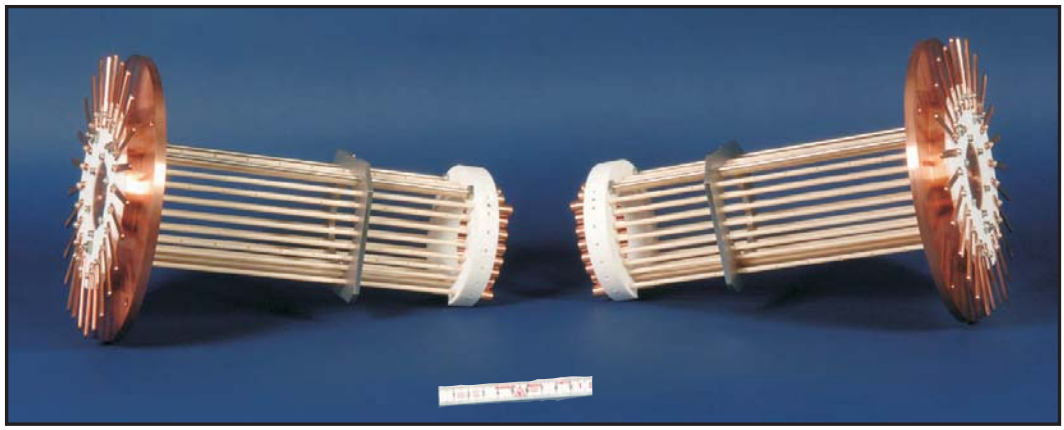

Figure 5.16: Photograph of the two connection system devices.

to the feedthroughs located on the vacuum caps mounted on EC1, EC2. The connection from the trap to the second-stage shield is achieved with the so-called *connection system*, consisting of the two devices shown in Fig. 5.16. Each one is made of a series of ceramic tubes arranged in a circle. These house the electrical wires, which can be therefore be safely plugged into the vacuum cap feedthroughs with a push & pull system without exerting a force on the wires themselves. Outside the second-stage shield, the cables must be carried to a diameter larger than the CF100 bellow. Therefore at the other end of the connection system, the electrical connections are carried to a larger circumference by radially-directed metal strips in contact with a ring of feedthroughs. From this point the cables are carried to the feeds placed on the removable lid of the outer shield of the magnet. The same scheme is applied on both sides of the trap, carrying out 25 connections on each side. To access the trap it will be necessary to open the shield lid, remove the connection system and then extract the trap stack.

## 5.3 Trap electronics

The electrodes EC1 and EC2 must provide the trapping of the 1.2-$\mu$s, 6-keV/u ion bunch coming from the LEBT line (see Fig. 3.5) and therefore the rise time of the potential at EC1 has to be shorter than the time $\tau_{out}$ the bunch needs to reach EC1 after being reflected at EC2. The whole electrode stack will be kept on a base voltage of $\sim$ 11 kV to decelerate the bunch to 2 keV/u. Applied to a trap length of 400 mm, this scheme yields a time $\tau_{out} = 400$ ns to raise the potential on EC1 from 11 to $\sim$ 18 kV [Her06a]. EC1 and EC2 will therefore be equipped with fast Behlke switches (push-pull MOSFET, HTS 161-06-GSM type), capable of handling a voltage difference of 16 kV with a rise time $\leq 60$ ns [Beh08].

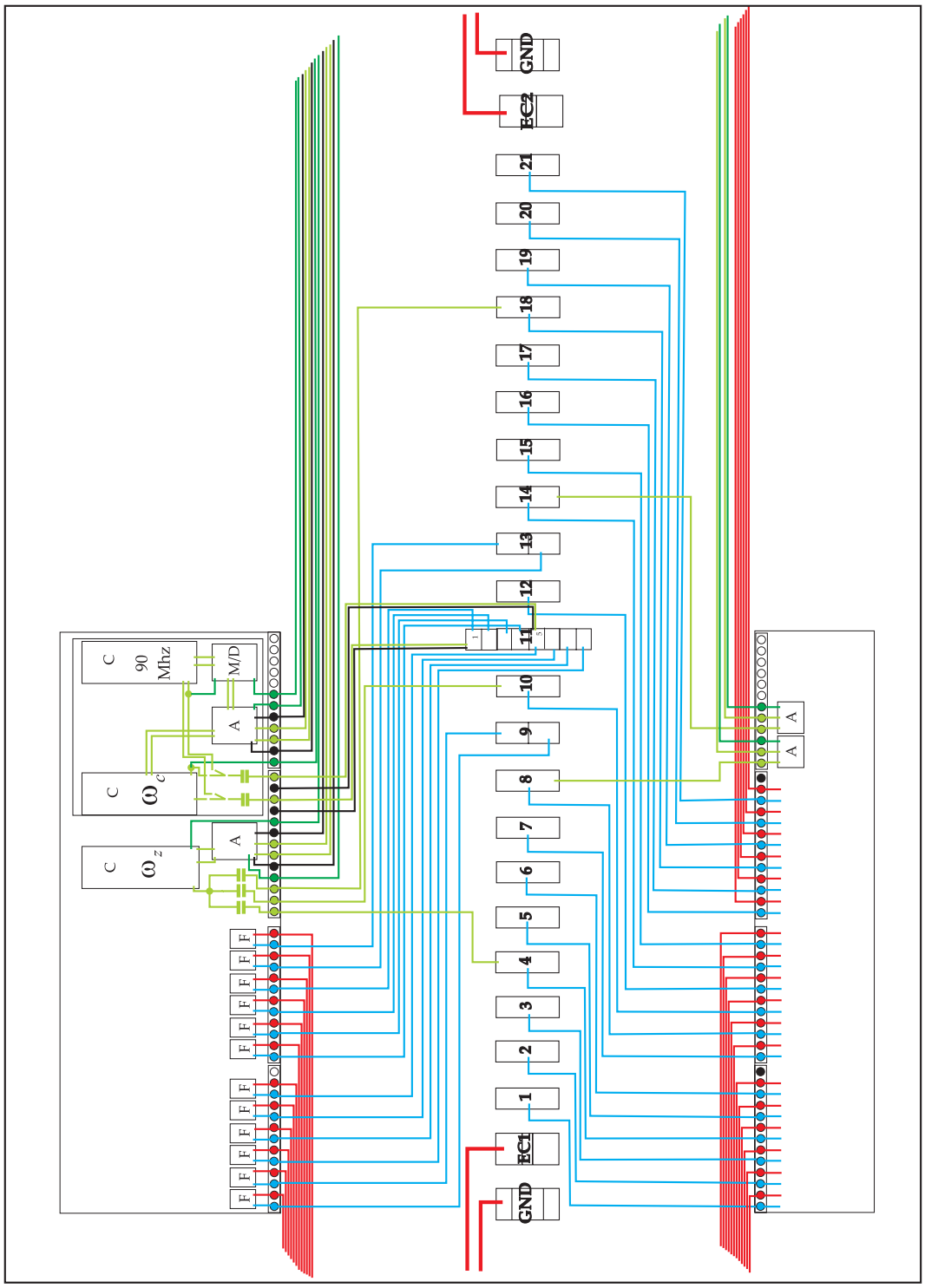


Figure 5.17: Scheme of the trap electronics. Inner electrodes are fed by the electronics box. EC1 and EC2 are handled directly via fast Behlke switches. The electronics box houses the coils (C) for the detection of axial and cyclotron motion of highly charged ions, the amplifiers (A) and the frequency mixer (M/D). A coil for future $\omega_c$ detection of antiprotons (90 MHz) is envisaged. (F) indicates the filters.

As mentioned in the Section above, all DC and AC electrode voltages will be handled by the electronics box (see Fig. 5.17). The location in the cold bore at 4 K minimizes the Johnson thermal noise $u_{eff} \propto \sqrt{k_B T}$, which affects the accuracy of set voltages, resonant detection and resistive cooling. Therefore the electronics box will house a printed board with the electronic circuitry and two coils (inductors) with their preamplifiers. One will be dedicated to ion detection and excitation around the cyclotron frequency $\nu_c = 35.5$ MHz[1]. The second, with an estimated Q-factor about 800, will be used for detection, excitation and cooling at the axial frequency $\nu_z \approx 400$ kHz at a trapping voltage $\approx 100$ V (see also Section 4.2.3 for details). As it is technically challenging to place a coil with such characteristics in the limited volume of the electronics box, coils with other parameters might also be finally used. The construction of the electronics devices and investigations on the most feasible and convenient solutions (subject of the upcoming thesis of Stephen Koszudowski) are ongoing.

The DC voltages in a range $\pm 200$ V will be applied to the inner electrodes. Stable voltages will be essential especially during the low-energy phase of the storage cycle, when resistive cooling is applied and noise sources translate into particle heating. The minimum electronic noise (ripple) at the power supply is in the order of 150 mV at maximal rated voltage. Linear digital power supplies will be used to reduce it to $20 \div 30$ mV. Lowpass filters in the electronics box will discriminate frequencies above 400 kHz.

The trap will be electrically connected to a high-voltage cage housing the power supplies which has been installed aside the HITRAP beamline. The trap will be remotely controlled from a container on the experimental platform, where a PC will control the power supplies via an optical fiber connection.

## 5.4 The test ion source

In order to test the Cooler Trap without requesting beam from the ESR, we intend to perform off-line routines of ion trapping and cooling. To this purpose we need a suitable ion source. Beam currents that can provide a total of $10^7$ charges are easily obtained with a wide variety of devices. However, to guarantee $10^{-13}$ mbar in the trap, the source (mounted at the entrance of the LEBT line) has to operate with a pressure of about $10^{-8}$ mbar. Therefore a suitable commercial ion source (SPECS IQO 12/38) has been purchased.

The IQO 12/38 is an electron impact ionization device working with $H_2$ and He gas (mass-to-charge ratio of ionized species $1 \div 4$ and therefore close to heavy and highly charged species). A differential pumping stage separates the ionization chamber (operating at $10^{-5} \div 10^{-4}$ mbar) from the main chamber, where a lower pressure can therefore be achieved (see Fig. 5.18). The manufacturer indicates a main chamber pressure $< 10^{-8}$ mbar. In our preliminary

[1] $U^{92+}$ eigenfrequencies have been taken as reference for the preparation of the coils.

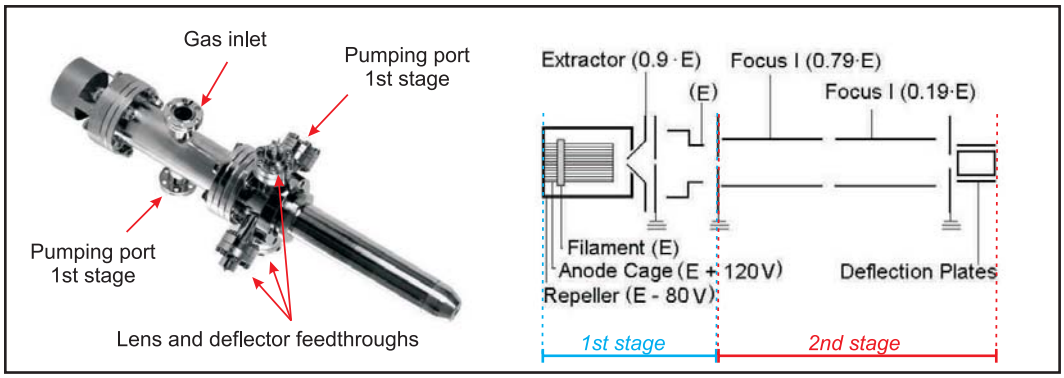


Figure 5.18: Test ion source. The sketch on the right shows the main elements and the optimized settings for $He^+$ ions. $E$ is the ion energy, defined as $E = q \cdot V_a$, with $V_a$ acceleration voltage. The two stages are divided by a diaphragm ensuring differential pumping. The working regime for the first stage (ionization region) is $10^{-5} \div 10^{-4}$ mbar. The goal is to achieve $10^{-8}$ mbar in the second stage. Photograph on the left taken from [SPE07].

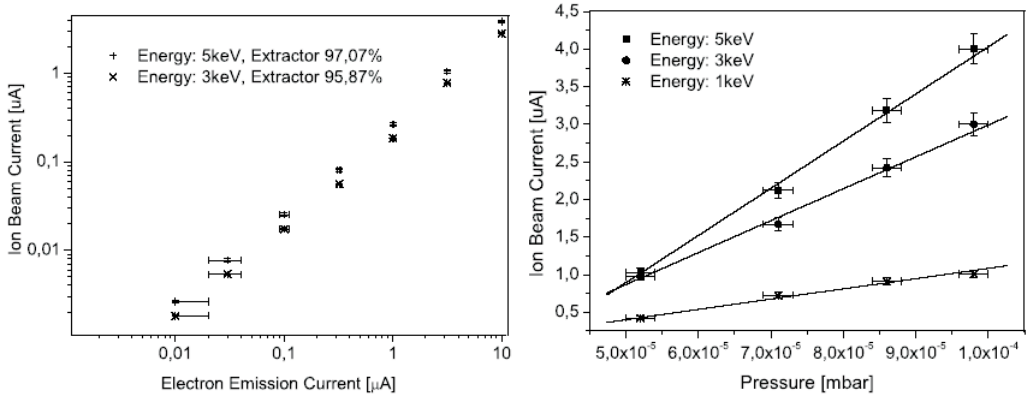


Figure 5.19: Ion current extracted from the test ion source. On the left, the $He^+$ ion beam current versus electron current. Extractor voltage is indicated as percentage of the acceleration voltage. On the right, ion beam current as a function of the pressure in the ionization chamber. As the ion beam increases with the pressure in the chamber, the limit will be given by the compromise with the required $10^{-8}$ mbar in the main chamber.

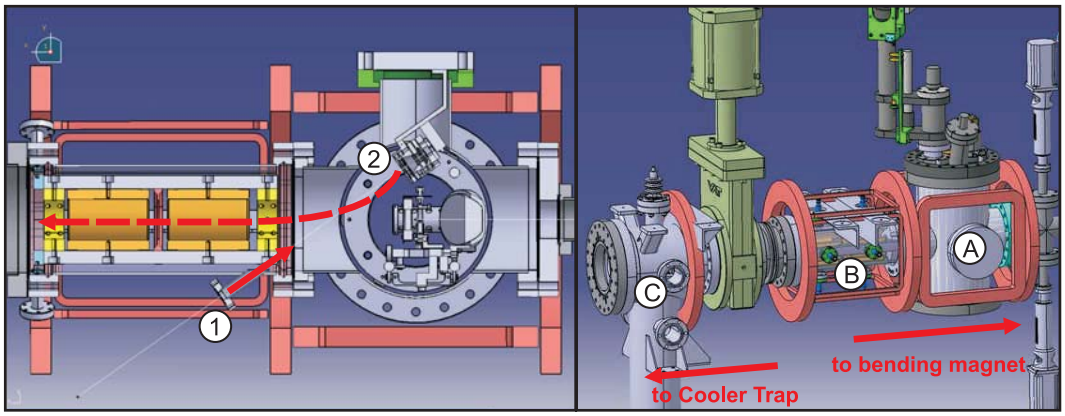


Figure 5.20: Photoelectron source. The UV laser beam coming from the laser source (1) impinges on the photocathode (2) placed off-axis in the diagnostics chamber. A pulse of $10^9$ emitted electrons (dashed line) is guided towards the Cooler Trap by the magnetic field produced by a set of magnets arranged in a so-called *saddle-coil* configuration (coils are depicted in pink). On the right, a 3D view of the Vertical Beamline immeditely after the Cooler Trap, up to the diagnostics chamber (A), shows the complete set of coils. The guiding field is about 200 G. (B) indicates the electrostatic quadrupole, (C) the turbopump flange directly outside the trap magnet.

tests with He gas we had a simple tabletop set-up, where the limited pumping capacity allowed only a vacuum between $6 \cdot 10^{-7}$ and $2 \cdot 10^{-6}$ mbar. Figure 5.19 shows the systematic studies on the ion current as a function of electron current and ionization chamber pressure. It can be seen that currents in the $0.01 \div 1$ $\mu$A range were measured, which guarantee trapping of a sufficient number of ions. We expect to match the pressure requirements and extend the range of our investigations during the upcoming trap injection tests with the source at the entrance of the LEBT line (summer/fall 2008).

## 5.5 Electron sources

The $10^9 \div 10^{10}$ electrons needed for electron cooling will be provided by a photoionization source presently being developed by A. Wolf and collaborators at MPI-K in Heidelberg. This uses a 262 nm UV laser shooting on a photocathode. A single-pulse injection is foreseen. The operation parameter must therefore be optimized to produce a pulse of at least $10^9$ electrons, short enought to be trapped as a whole. With a 100 ns laser pulse of power 2.9 $\mu$J/pulse it is possible to produce more than $10^9$ electrons (peak current 1.6 mA) with a kinetic energy of 300 eV. This gives a pulse length about 100 ns, corresponding to a length of about 1 m. Therefore the complete bunch can be trapped and a single pulsed injection is expected to provide the required

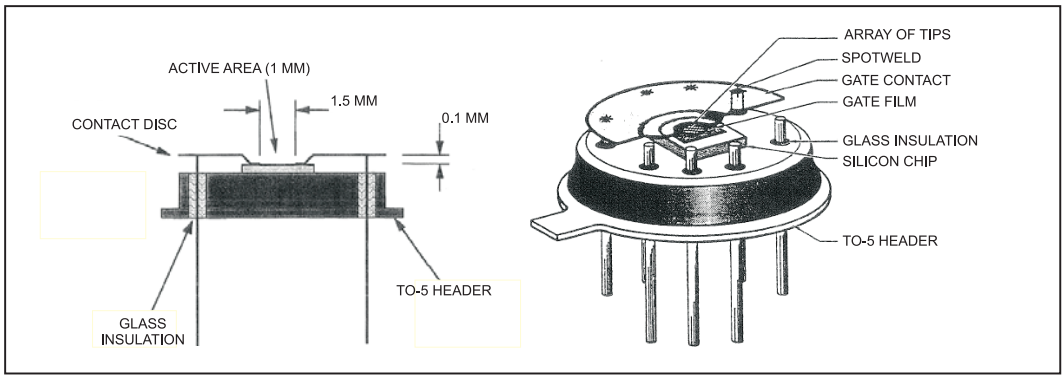


Figure 5.21: Spindt-type field emission array [SRI04]. The active area consists of a matrix of sub-$\mu$m tips producing an electron current on the basis of the field emission principle. The cathode is mounted on a TO-5 header.

amount of electrons. As it can be seen in Fig. 5.20, the source will be located inside a diagnostics box behind the trap. Minor modifications to the diagnostic chamber and the adjacent electric quadrupole have been applied in order to allow laser access. Since the production target is off-axis, electrons will be deviated on the axis and guided towards the trap by the magnetic field of an additional coil arrangement (*saddle coil*). A rather weak field of 200 G is sufficient to effectively focus and direct the electron beam [Orl08].

Alignment of the trap electric and magnetic axis is not possible by means of this electron source, since it is placed off-axis and the beam is steered by an additional magnetic field. For this purpose the assembly and installation of a Spindt-type field-emitter array (FEA) [SRI04] is presently ongoing. This device will be set behind the bending magnet at the end of the beamline in the ReInjection Channel (see Fig. 2.15). The alignment technique consists of a measurement of the electron current injected in the trap and reflected by the trapping electrode at the farthest end. A radially-segmented Faraday cup detects the reflected current on the different sectors, which will not be equal if electric and magnetic axis do not coincide. Another alignment option is via the detection of the electron beam with a phosphor screen installed at the other end of the trap, as used at RIKEN [Kur08]. Misalignment with respect to the magnetic field would result again in an off-centered image.

Since the Vertical Beamline and photoelectron source will be assembled in a later stage, we intend to use the Spindt cathode for the first tests of the Cooler Trap not only as alignment tool but also to load the trap with electrons, placing the source behind the turbopump flange right outside the magnet. As it can be seen in Fig. 5.21, the FEA has an active area of $\sim 1$ mm$^2$ where field-emission tips generate a continuous current up to $\sim 1$ $\mu$A (for details see [Plf01, SRI04]). This is expected to be sufficient to fill the

trap with $10^9 \div 10^{10}$ electrons[2]. Indeed theoretical and experimental studies on continuous injection in Penning traps have shown that the interaction between reflected and incoming particles prevents electrons from leaving the trap. The number of stored electrodes can be substantially higher than what suggested by the straightforward 'ballistic model', where electrons are trapped only by rising the endcap potential [Gor03]. An equilibrium is established as a result of the balance between two effects. First, setting on the trap endcap a voltage that allows injection but still creates a potential well, injected electrons that have lost energy in the two-stream interaction between incoming and reflected beam are captured. In this sense, synchrotron radiation in the trap's strong magnetic field represents an additional beneficial factor. On the other hand, trapping of the incoming beam is slowed and finally stopped by the build-up of space charge in the trap, which inhibits further injection.

[2] An important remark is that the Spindt FEA is a very delicate device and requires special care in handling; SRI does not guarantee good functioning. Nevertheless such a cathode has been used at ASACUSA as electron source, mounted on a radially-movable arm so that it could be positioned on the longitudinal axis for injection and then retracted [Kur05].

# Chapter 6

# Summary, conclusions and outlook

This work intended to give an overview of the HITRAP project. Since the project is under development, the first objective was to provide an introduction to the whole facility, summarizing the work done so far and explaining the scientific goals. The main features of the HITRAP linear decelerator were presented and discussed. The scientific program was introduced underlining the importance of the unprecedented combination of high charge states and low energy of stored stable and radioactive species. These factors will set new standards in accuracy for experiments on trapped ions as well as on low-energy collisions. With these experiments we expect to gain new information on the atomic structure and validate theoretical models.

The main focus of the thesis was on the physical and technical design of the Cooler Trap whose purpose presented new challenges. The problems arising from the confinement of $10^5$ highly charged ions as well as the better understanding and optimization of the cooling techniques were the main issues to be addressed. In this framework, the use of a Particle-In-Cell (PIC) code, although showing limitations in terms of computational effort and geometry simplification ($rz$-geometry) lead to significant progress. With the help of extensive simulations, it was shown that the complex phenomena of electron and resistive cooling can be efficiently handled in order to reach the stringent specifications set by the HITRAP goals, i.e. a final energy of 4 K. Nevertheless, it was evidenced that the resistive cooling of large ion samples will require cooling times larger than 10 s, i.e. the duty cycle of the Experimental Storage Ring. The possibility of formation of a Coulomb crystal at the lowest energy was also discussed.

At the moment of writing, the Double-Drift Buncher and the IH-linac have been installed in the ReInjection Channel. The buncher cavities have been commissioned in 2007 and the commissioning beamtime for the linac is about to start. The Radio Frequency Quadrupole has been conditioned and will be commissioned during the autumn. The Low-Energy Beam Transport line has

been assembled and the first transmission tests with the test ion source will begin after the linac commissioning. The Cooler Trap magnet has been tested already in 2007 and all parts of the electrode stack have been machined by now. The electronics is being finalized. The assembly of the trap and the injection, storage and cooling tests with the LEBT line and the test ion source will constitute the main activity for the rest of 2008. The Vertical Beamline will also be built by the end of the year and will become operational during 2009. In the meanwhile, some of the experiments will be set up. The installation of the laser spectroscopy experiment SPECTRAP is already in an advanced stage and the set-up for the surface experiment will be moved from KVI in Groningen to GSI before the end of 2008.

Although the facility is becoming operational, the experimentalist can gain more helpful information from further theoretical studies on the resistive cooling process. For instance, the experimental findings can be compared with ad-hoc simulations to get confirmations and better understanding when the experimental observables are not sufficient. Further optimization of the set-up can also be guided by simulations. Examples of useful theoretical studies are the systematics on the bandwidth of the cooling circuit and on the influence of contaminants (like different charge states). Another interesting field of investigation is the coupling of axial and radial motions and the possibility of cooling of the energy stored in the radial degrees of freedom, taking into account the presence of space charge effects which limit the effectiveness of radio frequency excitations. Thanks to its flexibility, the PIC code can be further optimized and modified. Therefore these as well as other phenomena can be included. For instance, developing a version of the code with a different geometry ($r\vartheta$ of full 3D) the coupling of motions could be studied.

# Bibliography


[Abr70] M. Abramowitz, J. Stegun, *Handbook of Mathematical Functions*, Dover, New York (1970).

[All89] M.P. Allen, D.J. Tildesley, *Computer Simulation of Liquids*, Clarendon Press, Oxford (1989) 78.

[Alo07] J.A. Alonso Otamendi, *Development of an Experiment for Ultrahigh-Precision g-Factor Measurements in a Penning-Trap Setup*, PhD Thesis, Mainz (2007).

[Ame05] F. Ames, G. Bollen, P. Delahaye, O. Forstner, G. Huber, O. Kester, K. Reisinger, P. Schmidt, *Cooling of radioactive ions with the Penning trap REXTRAP*, Nucl. Instr. Meth. Phys. Res. A **538** (2005) 17.

[Amo03] M. Amoretti, G. Bonomi, A. Bouchta, P.D. Bowe, C. Carraro, C.L. Cesar, M. Charlton, M. Doser, A. Fontana, M.C. Fujiwara, R. Funakoshi, P. Genova, J.S. Hangst, R.S. Hayano, L.V. Jorgensen, V. Lagomarsino, R. Landua, E. Lodi Rizzini, M. Macrí, N. Madsen, G. Manuzio, G. Testera, A. Variola, D. P. van der Werf, *Complete nondestructive diagnostic of nonneutral plasmas based on the detection of electrostatic modes*, Phys. Plasmas **10** (2003) 3056.

[Amo04] M. Amoretti et al., *The ATHENA antihydrogen apparatus*, Nucl. Meth. Phys. Res. A **518** (2004) 679.

[Arn99] M. Arnould, K. Takahashi, *Nuclear astrophysics*, Rep. Prog. Phys. **62** (1999) 395.

[Bar86] J. Barnes, P. Hut, *A hierarchical $O(N \log N)$ force-calculation algorithm*, Nature **324** (1986) 446.

[Bec01] D. Beck, F. Ames, M. Beck, G. Bollen, B. Delauré, P. Schuurmans, S. Schwarz, P. Schmidt, N. Severijns, O. Forstner, *Space Charge Effects in a Gas Filled Penning Trap*, Hyp. Int. **132** (2001) 473.

[Beh08] Behlke Power Electronics online catalogue, http://www.behlke.de (2008).

[Bei00] T. Beier, *The $g_j$ factor of a bound electron and the hyperfine structure splitting in hydogelike ions*, Phys. Rep. **339** (2000) 79.

[Bei02] T. Beier, H. Häffner, N. Hermanspahn, S.G. Karshenboim, H.-J. Kluge, W. Quint, S. Stahl, J. Verdú, G. Werth, *New Determination of the Electron's Mass*, Phys. Rev. Lett. **88** (2002) 011603.

[Bei03] T. Beier, P. Indelicato, V.M. Shabaev, V.A. Yerokhin, *New value for the electron's mass - theoretical foundations*, J. Phys. B **36** (2003) 1019.

[Bei03a] T. Beier, *Determination of the electron's mass from g-dactor experiments on $^{12}C^{5+}$ and $^{16}O^{7+}$* Nucl. Instr. Meth. B **205** (2003) 15.

[Bei01] P. Beiersdorfer, S.B. Utter, K.L. Wong, J.R. Crespo López-Urrutia, J.A. Britten, H. Chen, C.L. Harris, R.S. Thoe, D.B. Thorn, E. Träbert, M.G.H. Gustavsson, Christian Forssén, A.M. Marrtensson-Pendrill, *Hyperfine structure of hydrogenlike thallium isotopes*, Phys. Rev. A **64** (2001) 032506.

[Ber92] A. Berman, *Vacuum Engineering Calculations, Formulas and Solved Exercises*, Academic Press (1992).

[Bev88] N. Beverini, V. Lagomarsino, G. Manuzio, F. Scuri, G. Testera, G. Torelli, *Stochastic cooling in Penning traps*, Phys. Rev. A **38** (1988) 107.

[Bev88a] N. Beverini, V. Lagomarsino, G. Manuzio, F. Scuri, G. Testera, G. Torelli, *Experimental Verification of Stochastic Cooling in a Penning Trap*, Phys. Scr. **T22** (1988) 238.

[Bir69] C.K. Birdsall, D. Fuss, *Clouds-In-Clouds, Clouds-In-Cells Physics for Many-Body Plasma Simulation*, J. Comp. Phys. **3** (1969) 494.

[Bir91] C.K. Birdsall, A.B. Langdon, *Plasma Physics via Computer Simulation*, IOP, Bristol-Philadelphia (1991).

[Bla94] K. Blasche, K. Franzke, *Status Report of the SIS-ESR*, JACoW Conf. Proc. of EPAC 1994, London (1994) 133.

[Bla06] K. Blaum, *High-accuracy mass spectrometry with stored ions*, Phys. Rep. **425** (2006) 1.

[Ble89] B.I. Bleaney, B.Bleaney, *Electricity and Magnetism*, OUP, Oxford (1989).

[Bor70] J.P. Boris, *Relativistic plasma simulation-optimization of a hybrid code*, Proc. IV Conf. Num. Sim. Plasmas (1970) 3.

[Bos03] F. Bosch, *Schottky mass- and lifetime-spectrometry of unstable, stored ions*, J. Phys. B **36** 585.

[Bra99] M.P. Bradley, J.V. Porto, S. Rainville, J.K. Thompson, D.E. Pritchard, *Penning Trap Measurements of the Masses of* $^{133}Cs$, $^{85,87}Rb$, *and* $^{23}Na$ *with Uncertainties* $\leq 0.2$ *ppb*, Phys. Rev. Lett. **83** (1999) 4510.

[Bri96] J.-P. Briand, S. Thuriez, G. Giardino, G. Borsoni, M. Froment, M. Eddrief, C. Sébenne, *Observation of Hollow Atoms or Ions above Insulator and Metal Surfaces*, Phys. Rev. Lett. **77** (1996) 1452.

[Bro86] L.S. Brown, G. Gabrielse, *Geonium theory: Physics of an electron or ion in a Penning trap*, Rev. Mod. Phys. **58** (1986) 233.

[Bun67] O. Buneman, *Time-Reversible Difference Procedures*, J. Comp. Phys. **1** (1967) p.517.

[Cof04] W.T. Coffey, Y.P. Kamykov, J.K. Waldron, *The Langevin Equation, With Applications to Stochastic Problems in Physic, Chemistry and Electrical Engineering*, World Scientific (2004).

[Cre96] J.R. Crespo-López-Urrutia, P. Beiersdorfer, D.W. Savin, K. Widmann, *Direct Observation of Spontaneous Emission of the Hyperfine Transition* $F = 4$ *to* $F = 3$ *in Ground State Hydrogenlike* $^{165}Ho^{66+}$ *in an Electron Beam Ion Trap*, Phys. Rev. Lett. **77** (1996) 826.

[Cre98] J.R. Crespo-López-Urrutia, P. Beiersdorfer, K. Widmann, B.B. Birkett, A.M. Martensson-Pendrill, M.G.H. Gustavsson, *Nuclear magnetization distribution radii determined by hyperfine transition in the 1s level of H-like ions* $^{185}Re^{74+}$ *and* $^{187}Re^{74+}$, Phys. Rev. A **57** (1998) 879.

[Dah04] L. Dahl, W. Barth, Th. Beier, W. Vinzenz, C. Kitegi, U. Ratzinger, A. Schempp, *The HITRAP-Decelerator for Heavy Highly-Charged Ions*, JACoW Conf Proc. of EPAC 2004, Lübeck (2004) 39.

[Dah06] L. Dahl, W. Barth, Th. Beier, W. Vinzenz, C. Kitegi, U. Ratzinger, A. Schempp, *The HITRAP Decelerator Project at GSI*, JACoW Conf Proc. of EPAC 2006, Edinburgh (2006) 1568.

[Deh58] H.G. Dehmelt, *Spin Resonance of Free Electrons Polarized by Exchange Collisions*, Phys. Rev. **109** (1958) 381.

[Deh67] H.G. Dehmelt, *Radio-frequency spectroscopy of stored ions. I. Storage*, Adv. At. Mol. Phys. **3** (1967) 53.

[Deh68] H.G. Dehmelt, F.L. Walls, *"Bolometric" technique for the rf-spectroscopy of stored ions*, Phys. Rev. Lett. **21** (1968) 127.

[Deh69] H.G. Dehmelt, *Rafio-frequency spectroscopy of stored ions. II. Spectroscopy*, Adv. At. Mol. Phys. **5** (1969) 109.

[Dör00] R. Dörner, V. Mergel, O. Jagutzki, L. Spielberger, J. Ullrich, R. Moshammer, H. Schmidt-Böcking, *Cold Target Recoil Ion Momentum Spectroscopy: a 'momentum microscope' to view atomic collision dynamics*, Phys. Rep. 330 (2000) 95.

[DRE08] DREEBIT website, http://www.dreebit.com (2008).

[Dri83] C.F. Driscoll, J.H. Malmberg, *Length-Dependent Containment of a Pure Electron-Plasma Column*, Phys. Rev. Lett. **50** (1983) 167.

[Dub91] D.H.E. Dubin, *Theory of Electrostatic Fluid Modes in a Cold Spheroidal Non-Neutral Plasma*, Phys. Rev. Lett. **66** (1991) 2076.

[Dub99] D.H.E. Dubin, T.M. O'Neil, *Trapped nonneutral plasmas, liquids, and crystals (the thermal equilibrium states)*, Rev. Mod. Phys. **71** (1999) 87.

[Dyc87] R.S. Van Dyck, P.B. Schwinberg, H.G. Dehmelt, *New High-Precision Comparison of Electron and Positron g Factors*, Phys. Rev. Lett. **59** (1987) 26.

[Ear42] S. Earnshaw, *On the Nature of the Molecular Forces which Regulate the Constitution of the Luminiferous Ether*, Trans. Camb. Phil. Soc. **7** (1842) 97.

[Faj99] J. Fajans, *Lifetime scaling in non-neutral plasmas*, Comm. Mod. Phys. **1** (1999) 123.

[Fei99] X. Fei, W.M. Snow, *Cylindrical Penning traps with dynamic orthogonalized anharmonicity compensation for precision experiments*, Nucl. Instr. Meth. Phys Res. A **425** (1999) 431.

[Fra87] B. Franzke, *The heavy ion storage and cooler ring project ESR at GSI*, Nucl. Instr. Meth. B **24** (1987) 18.

[Fri91] J. Friedrich, A. Schempp, H. Deitinghoff, U. Bessler, H. Klein, R. Veith, N. Angert, J. Klabunde, *Properties of the GSI HLI-RFQ Structure*, PAC Conf. Proc. (1991) 3044.

[Gab84] G. Gabrielse, F.C. Mackintosh, *Cylindrical Penning traps with orthogonalized anharmonicity compensation*, Int. J. Mass Spec. Ion Proc. **57** (1984) 1.

[Gab89] G. Gabrielse, L. Haarsma, S.L. Rolston, *Open-endcap Penning traps for high precision experiments*, Int. J. Mass Spec. Ion Proc. **88** (1989) 319.

[Gab99] G. Gabrielse, D.S. Hall, T. Roach, P. Yesley, A. Khabbaz, J. Estrada, C. Heimann, H. Kalinowsky, *The ingredients of cold antihydrogen: Simultaneous confinement of antiprotons and positrons at 4 K*, Phys. Lett. B **455** (1999) 311.

[Gab06] G. Gabrielse, D. Hanneke, T. Kinoshita, M. Nio, B. Odom, *New Determination of the Fine Structure Constant from the Electron g-value and QED*, Phys. Rev. Lett. **97** (2006) 030802.

[Gif65] W.E. Gifford, *The Gifford-McMahon Cycle*, 1965 Cryogenic Eng. Conf. (1965).

[Gil88] S.L. Gilbert, J.J. Bollinger, D.J. Wineland, *Shell-Structure Phase of Magnetically Confined Strongly Coupled Plasmas*, Phys. Rev. Lett. **60** (1988) 2022.

[Gor03] V. Gorgadze, T. Pasquini, J. Fajans, J.S. Wurtele, *Injection into Electron Plasma Traps*, in M. Schauer, T. Mitchell, and R. Nebel, *Non-Neutral Plasma Physics V*, AIP **692** (2003) 30.

[Gre00] R.G. Greaves, C.M. Surko, *Inward Transport and Compression of a Positron Plasma by a Rotating Electric Field*, Phys. Rev. Lett. **85** (2000) 1883.

[Gru05] L. Gruber, J.P. Holder, D. Schneider, *Formation of Strongly Coupled Plasmas form Multi-Component Ions in a Penning Trap*, Phys. Scr. **71** (2005) 60.

[Häf00] H. Häffner, T. Beier, N. Hermanspahn, H.-J. Kluge, W. Quint, S. Stahl, J. Verdú, G. Werth, *High-accuracy Measurements of the Magnetic Moment Anomaly of the Electron Bound in Hydrogenlike Carbon*, Phys. Rev. Lett. **85** (2000) 5308.

[Häf03] H. Häffner, T. Beier, S. Djekić, N. Hermanspahn, H.-J. Kluge, W. Quint, S. Stahl, J. Verdú, T. Valenzuela, G. Werth, *Double Penning trap techniquefor precise g factor determinations in highly charged ions*, Eur. Phys. J. D **22** (2003) 163.

[Han08] D. Hanneke, S. Fogwell, G. Gabrielse, *New Measurement of the Electron Magnetic Moment and the Fine Structure Constant*, Phys. Rev. Lett. **100** (2008) 120801.

[Har01] J.C. Hardy, I.S. Towner, *Standard-Model Tests with Superallowed $\beta$-Decay: An Important Application of Very Precise Mass Measurements*, Hyp. Int. **132** (2001) 115.

[Hei91] D.J. Heinzen, J.J. Bollinger, F.L. Moore, W.M. Itano, D.J. Wineland, *Rotational Equilibria and Low-Order Modes of a Non-Neutral Ion Plasma*, Phys. Rev. Lett. **66** (1991) 2080.

[Her05] F. Herfurth, T. Beier, L. Dahl, S. Eliseev, S. Heinz, O. Kester, H.-J. Kluge, C. Kozhuharov, G. Maero, W. Quint, the HITRAP collaboration, *Highly chharged ions at rest: the HITRAP project at GSI*, in: Y. Yamazaki, M. Wada, *Physics with ultra slow antiproton beams*, AIP Conf. Proc. **793** (2005) 278.

[Her06] F. Herfurth, T. Beier, L. Dahl, S. Eliseev, S. Heinz, O. Kester, C. Kozhuharov, G. Maero, W. Quint, *Precision measurements with highly charged ions at rest: the HITRAP project at GSI*, Int. J. Mass Spec. **251** (2006) 266.

[Her06a] F. Herfurth, *The fast switch for the Cooler Trap entrance electrode*, GSI internal report (2006).

[Hoc65] R.W. Hockney, *A Fast Direct Solution of Poisson's Equation Using Fourier Analysis*, J. Ass. Comp. Mach. **12** (1965) 95.

[Hoc88] R.W. Hockney, J. W. Eastwood, *Computer Simulation Using Particles*, IOP, Bristol-Philadelphia (1988).

[Hof06] B. Hofmann, A. Schempp, O. Kester, *The HITRAP RFQ decelerator at GSI*, JACoW Proc. of EPAC 2006, Edinburgh (2006) 1586.

[Hof08] B. Hofmann, *Konstruktion und Aufbau einer kompakten RFQ-Spiral-Struktur zum Abbremsen hochgeladener Schwerionenstrahlen für das HITRAP-Projekt der GSI*, PhD thesis, Frankfurt (2008).

[Hug99] V.W. Hughes, T. Kinoshita, *Anomalous g values of the electron and muon*, Rev. Mod. Phys. **71** (1999) 133.

[Huk08] Hukseflux website, http://www.hukseflux.com (2008).

[Ich01] T. Ichioka, *Development of intense beam of ultracold antiprotons*, PhD thesis, Tokio (2001).

[Jac72] J.D. Jackson, *Classical Electrodynamics*, John Wiley and Sons, New York (1972).

[Kes06] O. Kester et al., *Proposal: HITRAP decelerator commissioning*, GSI internal document (2006).

[Kes06a] O. Kester, W. Barth, L. Dahl, F. Herfurth, M. Kaiser, H.-J. Kluge, C. Kozhuharov, W. Quint, B. Hofmann, U. Ratzinger, A. Sauer, A. Schempp, *Deceleration of highly charged ions for the HITRAP project at GSI*, JACoW Proc. of LINAC 2006, Knoxville (2006) 189.

[Khe98] H. Khemliche, T. Schlathölter, R. Hoekstra, R. Morgenstern, S. Schippers, *Hollow Atom Dynamics on LiF Covered Au(111): Role of the Surface Electronic Structure*, Phys. Rev. Lett. **81** (1998) 1219.

[Kin06] T. Kinoshita, M. Nio, *Improved $\alpha^4$ term of the electron anomalous magnetic moment*, Phys. Rev. D **73** (2006) 013003.

[Kla94] I. Klaft, S. Borneis, T. Engel, B. Fricke, R. Grieser, G. Huber, T. Kühl, D. Marx, R. Neumann, S. Schröder, P. Seelig, L. Völker, *Precision Laser Spectroscopy of the Ground State Hyperfine Splitting of Hydrogenlike $^{209}Bi^{82+}$*, Phys. Rev. Lett. **18** (1994) 2425.

[Klu07] H.-J. Kluge, W. Quint, D.F.A. Winters, *Atomic physics experiments with trapped and cooled highly charged ions*, J. Phys.: Conf. Series **58** (2007) 9.

[Kur05] N. Kuroda, H. A. Torii, K.Y. Franzen, Z. Wang, S. Yoneda, M. Inoue, M. Hori, B. Juhász, D. Horváth, H. Higaki, A. Mohri, J. Eades, K. Komaki, Y. Yamazaki, *Confinement of a Large Number of Antiprotons and Production of an Ultraslow Antiproton Beam*, Phys. Rev. Lett. **94** (2005) 023401.

[Kur08] N. Kuroda, private communication (2008).

[Laf98] J.L. Lafferty, *Foundations of Vacuum Science and Technology*, John Wiley and Sons, New York (1998).

[Lat95] R.V. Latham, *High Voltage Vacuum Insulation*, Academic Press (1995).

[Lem05] C. Lemell, X.M. Tong, K. Tokesi, L. Wirtz, J. Burgdörfer, *Electron emission from surfaces induced by HCI and lasers*, Nucl. Instr. Meth. Phys. Res. B **235** (2005) 425.

[Maj04] F.G. Major, V.N. Gheorghe, G. Werth, *Charged Particle Traps*, Springer, New York (2004).

[Mal75] J.H. Malmberg, J.S. deGrassie, *Properties of Nonneutral Plasma*, Phys. Rev. Lett. **35** (1975) 577.

[Man86] R. Mann, *Total One-Electron Capture Cross Sections for $Ar^{q+}$ and $I^{q+}$ in Slow Collisions on $H_2$ and He*, Z. Phys. D **3** (1986) 85.

[Mar08] MarkeTech International website, http://www.mkt-intl.com (2008).

[Mar94] R.E. Marrs, S.R. Elliott, D.A. Knapp, *Production and Trapping of Hydrogenlike and Bare Uranium Ions in an Electron Beam Ion Trap*, Phys. Rev. Lett. **72** (1994) 4082.

[McD02] J.W. McDonald, R.W. Bauer, D.H.G. Schneider, *Extraction of highly charged ions (up to 90+) from a high-energy electron-beam ion trap*, Rev. Sc. Instr. **73** (2002) 30.

[Mit95] D.W. Mitchell, R.D. Smith, *Cyclotron motion of two Coulombically interacting ion clouds with implication to Fourier-transform ion cyclotron resonance mass spectrometry*, Phy. Rev. E **52** (1995) 4366.

[Mit97] D.W. Mitchell, R.D. Smith, *Two dimensional many particle simulation of trapped ions*, Int. J. Mass Spec. Ion Proc. **165/166** (1997) 271.

[Mit08] R. Mitchell, private communication (2008).

[Moh98] P.J. Mohr, G. Plunien, G. Soff, *QED corrections in heavy atoms*, Phys. Rep. **293** (1998) 227.

[Moh02] A. Mohri, Y. Kiwamoto, T. Yuyama, T. Michishita, *Different Features of Electron Plasma Confinement of Rectangular and Harmonic Electric Potential Wells*, 29th EPS Conf. on Plasma Phys. and Contr. Fusion, Eur.Conf. Abstracts **26B** (2002).

[Moh08] P.J. Mohr, B.N. Taylor, D.B. Newell, *CODATA recommended values of the fundamental physical cnstants: 2006*, Rev. Mod. Phys. **77** (2005) 1.

[Moo02] R.B. Moore, *Buffer gas cooling of ion beams*, internal report (2002).

[Möl07] B. Möllers, C. Toepffer, M. Walter, G. Zwicknagel, C. Carli, H. Nersysian, *Cooling of ions and antiprotons with magnetized electrons*, Nucl. Instr. Meth. Phys. Res. A **532** (2004) 279.

[Ner07] H. Nersisyan, C. Toepffer, G. Zwicknagel, *Interactions Between Charged Particles in a Magnetic Field*, Springer, Berlin-Heidelberg (2007).

[Odo06] B. Odom, D. Hanneke, B. D'Urso, G. Gabrielse, *New Measurement of the Electron Magnetic Moment Using a One.Electron Quantum Cyclotron*, Phys. Rev. Lett. **97** (2006) 030801.

[Orl08] D. Orlov, A. Wolf, private communication (2008).

[Ota07] J.A. Otamendi, *Development of an Experiment for Ultrahigh-Precision g-factor Measurements in a Penning-Trap Setup*, PhD thesis, Mainz, 2007.

[Pac96] K. Pachucki, D. Leibfried, M. Weitz, A. Huber, W. König, T. W. Hänsch, *Theory of the energy levels and precise two-photon spectroscopy of atomic hydrogen and deuterium*, J. Phys. B **29** (1996) 177.

[Pac98] K. Pachucki, *Quantum electrodynamics of weakly bound systems*, Hyp. Int. **114** (1998) 155.

[Paj94] M. Pajek, R. Schuch, *Total radiative recombination rates for ions interacting with electrons from an electron cooler*, Nucl. Instr. Meth. Phys. Res. B **93** (1994) 241.

[Pan01] V.S. Pandit, P.R. Sarma, R. K. Bhandari, *Modification of a double drift bunching beam system to get the efficiency of a six harmonic buncher*, Proc. of Cyclotron and their Applications 2001, AIP Conf. Proc. **600** (2001) 452.

[Pau53] W. Paul, H. Steinwedel, *Ein Neues Massenspektrometer Ohne Magnetfeld*, Zeit. Naturforschung A **8** (1953) 448.

[Pie49] J.R. Pierce, *Theory and Design of Electron Beams*, D. Van Nostrand Co., New York (1949).

[Plf01] D.G. Pflug, M. Schattenburg, H.I. Smith, A.I. Akinwande, *Field Emitter Arrays for Low Voltage Applications with sub 100 nm apertures and 200 nm period*, IEEE International Devices Meeting, Washington (2001).

[Pot90] H. Poth, *Electron cooling: Theory, Experiment, Application*, Phys. Rep. **196** (1990) 135.

[Rat98] U. Ratzinger, R. Tiede, *Status of the HIIF RF linac study based on H-mode cavities*, Nucl. Instr. Meth. Phys. Res. A **415** (1998) 229.

[Ryj05] V. L. Ryjkov, L. Blomeley, M. Brodeur, P. Grothkopp, M. Smith, P. Bricault, F. Buchinger, J. Crawford, G. Gwinner, J. Lee, J. Vaz, G. Werth, J. Dilling and TITAN Collaboration, *TITAN project status report and a proposal for a new cooling method of highly charged ions*, Eur. Phys. J. A **25** (2005) 63.

[Rin06] R. Ringle, P. Schury, T. Sun, G. Bollen, D. Davis, J. Huikari, E. Kwan, D.J. Morrissey, A. Prinke, J. Savory, S. Schwarz, C. Sumitrarachchi, *Precision mass measurements with LEBIT at MSU*, Int. J. Mass Spec. **251** (2006) 300.

[Sch06] H. Schatz, *The importance if nuclear masses in the astrophysical rp-process*, Int. J. Mass Spec. **251** (2006) 293.

[See98] P. Seelig, S. Borneis, A. Dax, T. Engel, S. Faber, M. Gerlach, C. Holbrow, G. Huber, T. Kühl, D. Marx, K. Meier, P. Merz, W. Quint, F. Schmitt, M. Tomaselli, L. Völker, H. Winter, M. Würtz, K. Beckert, B. Franzke, F. Nolden, H. Reich, M. Steck, T. Winkler, *Ground State Hyperfine Splitting of Hydrogenlike* $^{207}Pb^{81+}$ *by Laser Excitation of a Bunched Ion Beam in the GSI Experimental Storage Ring*, Phys. Rev. Lett. **81** (1998) 4824.

[Sha06] V.M. Shabaev, *g-Factor of Heavy Ions: A New Access to the Fine Structure Constant* Phys. Rev. Lett. **96** (2006) 253002.

[Shi82] K. Shima, T. Ishihara, T. Mikumo, *Empirical Formula for the Average Equilibrium Charge-State of Heavy Ions Behind Various Foils*, Nucl. Instr. Meth. **200** (1982) 605.

[Sch84] A.S. Schlachter, *Charge-Changing-Collisions*, Proc. of the 10th Int. Cyclotron Conf. (1984) 563.

[Sch05] S. Schwarz, private communication (2005).

[Sik03] G. Sikler, *Massenspektrometrie kurzlebiger Sr- und Sn-Isotope und Aufbau der SHIPTRAP-Penningfallen*, PhD Thesis, Heidelberg (2003).

[SIM95] D.A. Dahl, *SIMION 3D Version 6.0 User's Manual*, INEL Idaho Falls (1995).

[SPE07] SPECS IQE 12/38 online catalogue, http://www.specs.de (2007).

[Spr99] Q. Spreiter, M. Walter, *Classical Molecular Dynamics Simulation with the Velocity Verlet Algorithm at Strong External Magnetic Fields*, J. Comp. Phys. **152** (1999) 102.

[SRI04] SRI International, FEP field emitter array manual (2004).

[Ste04] M. Steck, K. Beckert, P. Beller, B. Franczak, B. Franzke, F. Nolden, *Improved Performance of the Heavy Ion Storage Ring ESR*, JACoW Proc. of EPAC 2004, Lucerne (2004) 1168.

[Stu08] S. Sturm, private communication (2008).

[TDR03] T. Beier, L. Dahl, H.-J. Kluge, C. Kozhuharov, W. Quint, *HITRAP Technical Design Report*, GSI Darmstadt (2003).

[Tho08] R.C. Thompson, private communications (2007-2008).

[Ull03] J. Ullrich, R. Moshammer, A. Dorn, R. Dörner, L. Ph. H. Schmidt, H. Schmidt-Böcking, *Recoil-ion and momentum spectroscopy: reaction-microscopes*, Rep. Prog. Phys. **66** (2003) 1463.

[Van84] S. Van Der Meer, *An Introduction to Stochastic Cooling*, CERN/PS/84-33 (1984).

[Ver01] J.L. Verdú Galiana, *One experiment for the high precision measurement of the $g_j$-factor of the electron bound in hydrogenlike ions*, diploma thesis, Mainz (2001).

[Ver04] J. Verdú, S. Djekić, S. Stahl, T. Valenzuela, M. Vogel, G. Werth, *Electronic g Factor of Hydrogenlike Oxygen* $^{16}O^{7+}$, Phys. Rev. Lett. **92** (2004) 093002.

[Vog05] M. Vogel, D.F.A. Winters, D.M. Segal, R.C. Thompson, *Proposed precision spectrometer for trapped, highly charged ions*, Rev. Sci. Instr. **76** (2005) 103102.

[Wan98] T.P. Wangler, *Principles of RF Linear Accelerators*, John Wiley and Sons, New York (1998).

[Win06] D.F.A. Winters, M. Vogel, D.M. Segal, R.C. Thompson, *Electronic detection of charged particle effects in a Penning trap*, J. Phys. B **38** (2006) 3131.

[Win75] D.J. Wineland, H.G. Dehmelt, *Principles of the stored ion calorimeter*, J. Appl. Phys. **46** (1975) 919.

[Zwi05] G. Zwicknagel, *Electron Cooling of Ions and Antiprotons in Traps*, AIP Conf. Proc. of of COOL05 (2005) 513.

[Zwi06] G. Zwicknagel, *Electron Cooling of Highly Charged Ions in Penning Traps*, in: M. Drewsen, U. Uggerhoj, H. Knudsen, *Non-neutral Plasma Physics VI*, AIP Conf. Proc. **862** (2006) 281.

# Acknowledgments

The completion of a PhD work is surely not a lone ride - although one might feel like walking in the desert with the mirage of the end, at times... My gratitudes goes to my supervisor H.-Jürgen Kluge, who accepted me in his group. I am particularly grateful for his guidance during the writing and correction of my thesis. I have learned a lot from his accuracy and high standards. I also thank Prof. Dr. Andreas Wolf for accepting to be my second supervisor, as well as Prof. Dr. Otto Nachtmann and Priv. Doz. Habil. Ulrich Glasmacher for joining the examination committee.

The following list is most probably incomplete and surely a total mess. This comes as the separation between colleagues and friends is a really a zero-order approximation. I hope no one is offended by apparently improper categorization.

I sincerely thank Frank Herfurth, my everyday supervisor. That is, the person I went to when I had questions, doubts, manic frustration. His focused, problem-solving driven attitude and his ability to strip problems and solutions down to the core gave me a tremendous push when I was in front of apparently crazy puzzles. The HITRAP and SHIPTRAP teams were my constant company for four years and we shared a lot both in human and professional terms. Thanks to all of them: Oliver Kester and Wolfgang Quint, Michael Block and the whole bunch of coming and going students and post-docs. I would like to mention Christian Rauth, whom I had a lot of fun with, Gleb Vorobjev (night shifts cannot be better), Sergey Eliseev, Ana Martin and the Indian gang. The kindness of Yuri Novikov and Nikita Kotovskiy cannot be overlooked. Special encouragements to my dear fellow Stephen Koszudowski, who is next on the list...

Stefan Schwarz (MSU) not only provided the simulation code but also his gargantuan programming experience when I had to make several implementations or merely understand the complexity of his code. Physics and programming discussions with Günter Zwicknagel were priceless. The Mainz collaboration supervised by Günther Werth and Klaus Blaum as well as Stefan Stahl, Manuel Vogel, Danyal Winters (GSI), Richard Thompson (Imperial College), Yasunori Yamazaki and Naofumi Kuroda (ASACUSA) gave me answers and inputs... Or posed new questions, which is often useful if not necessary. Giovanni Bettega (Università di Milano) gave me some really cool suggestions which I used with great advantage for my analysis. Christophor Kozhuharov

provided not only a wide range of intellectual input but also the kind assistance in getting the fundamental computing power. Thanks to the laser spectroscopy group of Wilfried Noerthershaeuser, especially to Guido Ewald and Rodolfo Sanchez, for sharing with me the office, their warm friendship and the basic knowledge on survival in Germany when I arrived here.

Barbara Sulignano, Marco Mazzocco, Martino Trassinelli, Fabio Farinon (and more!) have been real good friends to appeal to for Mr. Gumby's brain decompression. Special mention goes to Gianluigi Clemente for the mutual exchange of good company and nervous breakdowns in the last year.

Obviously I did not sever the links with my country. I acknowledge my former supervisor Piero Quarati for continuous and warm contact as well as interesting discussion. The same holds for my mate Fabrizio Ferro, whose friendship I am honoured of. Former school and university mates prove that true bonds can be stronger than distance. Claudio, *Mr. 74 m* and 5 Star Grave keep on being the dark side of the moon. I thank Kronic and its staff (*www.kronic.it*) for taking away all of the time I had left for sleeping and filling it with hundreds of albums to listen to, articles to write, bursts of rage for random organization, lack of editing, mysterious bugs and a fundamental, tantalizing love for music.

The support I received from Simona and my family and my thanks for their endurance are things I cannot express or quantify properly. Luckily, they never asked me for a graph or a histogram about that.

*And now for something completely different.*